République Algérienne Démocratique et Populaire
Ministère de l'Enseignement Supérieur et de la Recherche Scientifique
Université A.MIRA-BEJAIA

جامعة بجاية
Tasdawit n Bgayet
Université de Béjaïa

Faculté de Technologie
Département Génie Electrique
Laboratoire d'Informatique Médicale (LIMED)

THÈSE

EN VUE DE L'OBTENTION DU DIPLOME DE DOCTORAT

Domaine : Sciences et Technologies Filière : Télécommunication
Spécialité : Réseaux et Télécommunications

Présentée par

ALKAMA Dina

Thème

Analyse de la Liaison Descendante dans les Réseaux Cellulaires Assistés par des Véhicules Aériens sans Pilote (VAP) Equipés par des Antennes MIMO

Soutenue le 05 Janvier 2025 **Devant le Jury composé de :**

Nom et Prénom	**Grade**		
Mr Khireddine Abdelkrim	Professeur	Univ. de Bejaia	Président
Mr Azni Mohamed	Professeur	Univ. de Bejaia	Rapporteur
Mr Ouamri Mohamed Amine	MC	Univ. de Paris XIII-USPN	Co-Rapporteur
Mr Berrah Smail	Professeur	Univ. de Bejaia	Examinateur
Mr Amroun Kamal	Professeur	Univ. de Bejaia	Examinateur
Mr Ferhat Hamida Abdelhak	Professeur	Univ. de Sétif 1	Examinateur

Année Universitaire : 2024/2025

People's Democratic Republic of Algeria
Ministry of Higher Education and Scientific Research
University A.MIRA of BEJAIA

جامعة بجاية
Tasdawit n Bgayet
Université de Béjaïa

Faculty of Technology
Electrical Engineering Department
Laboratory of Medical Informatics (LIMED)

THESIS

FOR THE ATTAINMENT OF THE DOCTORAL DEGREE

Domain : Science and Technology Sector : Telecommunication
Specialty : Networks and Telecommunications

Presented by

Dina ALKAMA

Theme

Downlink Analysis in Cellular Networks Assisted by Unmanned Aerial Vehicles (UAVs) Equipped with MIMO Antennas

Defended on January 5, 2025 **Before the Jury composed of :**

Name and Surname	**Grade**		
Mr Abdelkrim Khireddine	Professor	Univ. of Bejaia	Chair
Mr Mohamed Azni	Professor	Univ. of Bejaia	Supervisor
Mr Mohamed Amine Ouamri	Associate professor	Univ. of Paris XIII-USPN	Co-Supervisor
Mr Smail Berrah	Professor	Univ. of Bejaia	Examinator
Mr Kamal Amroun	Professor	Univ. of Bejaia	Examinator
Mr Abdelhak Ferhat Hamida	Professor	Univ. of Sétif 1	Examinator

Academic Year : 2024/2025

To my beloved father, mother, and siblings...♡

Acknowledgements

Alhamdulillah, I praise and thank Allah for his greatness and for giving me the strength and determination to complete this thesis.

I would like to begin by expressing my indebtedness gratitude and deepest thanks to my thesis supervisors, Professor Mohamed Azni and Doctor Mohamed Amine Ouamri, for their invaluable flexibility, support, and guidance throughout the thesis process.

My sincere thanks to Professor Hachem Slimani, Head of the LIMED laboratory, for his kind permission to conduct this thesis in this laboratory, for his warm welcome and for the resources made available to me to facilitate the completion of my work.

I would like to extend my profound recognition to Professor Aduwati Sali for hosting me for a one-month scientific research visit in her research group in the WIPNET laboratory at UPM University. During my time with her, she provided me with invaluable guidance and insights, and she generously shared her knowledge with me.

My warmest thanks go to Professor Abdelkrim Khirddine, for graciously accepting the role of jury chair. I would like to extend my gratitude to Professor Smail Berrah, Professor Amroun Kamal and Professor Abdelhak Ferhat Hamida for agreeing to examine my work and their time and interest in my work.

My greatest beloved parents deserve special mention and warmest thanks for their invaluable support. Thank you, my father, my hero, for offering unwavering moral and financial support at every stage. You were the first to encourage me to pursue my Ph.D. You are always there for me, and you have consistently provided extraordinary solutions to my problems. Thank you, my mother, for your invaluable assistance, moral support, and prayers. You were consistently available to listen and provide guidance when I needed it most. You were my source of strength when I was struggling. Without you, mom, I would not have been able to complete this thesis.

I would be remiss if I did not acknowledge the invaluable help of my beloved siblings Lynda, Kouceila, and Narima, who provided me with guidance based on their experience and most importantly who put up with my nervous breakdowns.

I also acknowledge my esteemed friends, colleagues, and the LIMED laboratory team.

Contents

List of Figures vii

List of Tables x

List of Abbreviations and Acronyms xi

List of Mathematical Notations xiv

Introduction 1

1 Deployment and Coverage Analysis of Heterogeneous Cellular Networks 6

1.1 Introduction . . . 7
1.2 Coverage Concept in Cellular Networks . . . 7
1.3 Coverage Methods in Cellular Networks . . . 8
1.3.1 Heuristic Methods . . . 8
1.3.2 Stochastic Geometry Based Methods . . . 9
1.4 Heterogeneous Networks . . . 9
1.4.1 Terrestrial Heterogeneous Networks . . . 10
1.4.2 Vertical Heterogeneous Networks . . . 11
1.5 Aerial Networks vs Terrestrial Networks . . . 12
1.6 Unmanned Aerial Vehicles Communication . . . 12
1.6.1 UAV Categories . . . 13
1.6.2 UAV Applications . . . 16
1.6.3 UAV Communications in Industry . . . 17
1.7 Stochastic Geometry Tools . . . 18
1.7.1 Point Process Theory . . . 18
1.7.1.1 Poisson Point Process . . . 20
1.7.1.2 Poisson Cluster Process . . . 23
1.7.1.3 Binomial Point Process . . . 25
1.7.2 Random Shape Theory . . . 26
1.7.2.1 Boolean Model . . . 26
1.8 Conclusion . . . 27

2 Stochastic Geometry Modeling and Performance Metrics **28**
2.1 Introduction . . . 29
2.2 Channel Propagation . . . 29
2.2.1 Channel Characterization . . . 29
2.2.2 Propagation Effects . . . 30
2.2.2.1 Path loss . . . 30
2.2.2.2 Shadowing . . . 31
2.2.2.3 Small-scale Fading . . . 31
2.3 Cell Association Strategies . . . 34
2.4 Network Performance Measurement . . . 36
2.4.1 SINR . . . 36
2.4.1.1 Inter-cell interference . . . 37
2.4.2 SINR Coverage Probability . . . 38
2.4.3 SINR Outage Probability . . . 39
2.4.4 Spectral Efficiency . . . 39
2.4.4.1 Area Spectral Efficiency . . . 39
2.4.4.2 Network Spectral Efficiency . . . 40
2.5 Monte Carlo Simulations . . . 40
2.6 Conclusion . . . 41

3 Single-Tier Networks: UBS Swarms Modeling **42**
3.1 Introduction . . . 43
3.2 UBS Deployment in Isolated Regions . . . 43
3.3 Beamforming Technology in Aerial Networks . . . 44
3.3.1 Directional Beamforming . . . 44
3.3.2 3D Beamforming . . . 44
3.4 UBS Swarm . . . 45
3.5 System and Channel Modeling . . . 46
3.5.1 UAV Network Model and Assumptions . . . 46
3.5.2 Air-To-Ground Channel Model . . . 48
3.5.3 Vertical Antenna Pattern Gain . . . 49
3.5.4 User Association and SINR Model . . . 49
3.6 Probability Density Function . . . 51
3.6.1 Conditional Serving Distance Distribution . . . 52
3.6.2 Conditional Interfering Distance Distribution . . . 53
3.7 Conclusion . . . 53

4 Modeling of Vertical Heterogeneous Networks Under 3D Blockage Effects **55**
4.1 Introduction . . . 56

4.2 UBS Deployment in Hotspot Scenarios . . . 56
4.3 mmWave Communication Issues in Dense Cities . . . 57
4.4 Multiuser MIMO Communication Systems . . . 58
4.5 System and Channel Modeling . . . 60
4.5.1 Network Model and Assumptions . . . 60
4.5.2 3D Blockage Model . . . 60
4.5.3 Channel Propagation Model . . . 62
4.5.4 Directional Beamforming Gain . . . 66
4.5.5 User Association and SINR Model . . . 67
4.5.6 Extension to A Model With 3D Beamforming . . . 70
4.6 Probability Density Function . . . 70
4.6.1 Distance Distribution in the UBS Tier . . . 70
4.6.2 Distance Distribution in the 0^{th} Tier . . . 71
4.6.3 Distance Distribution in the 1^{st} Tier . . . 71
4.6.4 Conditional Serving Distance Distribution . . . 71
4.6.5 Conditional Interfering Distance Distribution . . . 72
4.7 Conclusion . . . 72

5 Downlink Performance Analysis of UAV-assisted Cellular Networks 74
5.1 Introduction . . . 75
5.2 Downlink Performance Analysis of Single-Tier Aerial Networks . . . 75
5.2.1 Coverage Probability . . . 75
5.2.2 UBSs Number Optimization . . . 78
5.2.3 Network Spectral Efficiency . . . 78
5.2.4 Simulation and Performance Evaluation . . . 79
5.2.4.1 Model Validation . . . 79
5.2.4.2 Impact of h . . . 80
5.2.4.3 Impact of the Tilt Angle . . . 82
5.2.4.4 Impact of the User's Location . . . 82
5.2.4.5 SA UBSs Optimization . . . 83
5.2.4.6 Impact of K and ω on the NSE . . . 84
5.3 Downlink Performance Analysis of VHetNets under 3D Blockage Effects . . . 85
5.3.1 Coverage Probability . . . 85
5.3.2 Coverage Probability With Shadowing . . . 89
5.3.3 Coverage Probability With 3D Beamforming . . . 90
5.3.4 Coverage Probability With Manageable Scenario . . . 90
5.3.5 Area Spectral Efficiency . . . 91
5.3.6 Simulation and Performance Evaluation . . . 92
5.3.6.1 Impact of σ_u on the Association Probability . . . 92

5.3.6.2 Impact of h and p on the Association Probability 94
5.3.6.3 Model Validation 94
5.3.6.4 Model Validation under Fixed/Random h 94
5.3.6.5 Impact of h on the Coverage Probability 96
5.3.6.6 Correlation between Shadowing, h and N 98
5.3.6.7 Blockage Effects on the Coverage Probability 100
5.3.6.8 Impact of N and N_a on the ASE 101
5.3.6.9 Comparaison between 2D and 3D Beamforming 103
5.4 Conclusion 104

Conclusion and Future Works **105**

Appendices **108**
Appendix A: Proof of Lemma 5.2.2 108
Appendix B: Proof of Theorem 5.7 110
Appendix C: Proof of Lemma 5.3.6 111

Bibliography **112**

List of Figures

1.1 Terrestrial heterogeneous network architecture composed of a macro, micro, pico, and femto cell. . . . 10
1.2 Multi-layered VHetNet architecture comprised of aerial, satellite and terrestrial networks. . . . 11
1.3 UAV classification based on flying mechanism and structure. . . . 13
1.4 Network architecture of HAPs, MAPs, and LAPs. . . . 15
1.5 Main UAV applications. . . . 17
1.6 A comparison between a stochastic geometry-based deployment and a hexagonal deployment where the red squares indicate the BS location. (a) The hexagonal model represents the coverage area of the BS as an hexagon, (b) PPP-based BS distribution, the Voronoi cells are presented by polygonal regions. . . . 22
1.7 Realization of TCP and MCP through Voronoi tessellation. The red squares represent the parent points, which are GBSs distributed according to the PPP. The green points represent the daughter points, which are users clustered around the parent points. . . . 24
1.8 A top view snapshot of UAV-assisted cellular network. The black triangles represent the UAVs distributed by BPP in a finite circular region and the GBSs shown as red squares generated by PPP. . . . 25

2.1 Illustration of Various Propagation Channels. . . . 30
2.2 Effects of Path loss, Shadowing, and Fading. . . . 33
2.3 Cell association rules. . . . 35
2.4 Intercell interference. . . . 37
2.5 Key performance measures based on the SINR, employed in the abstraction of stochastic geometry. . . . 38

3.1 Illustration of 2D beamforming and 3D beamforming. . . . 45
3.2 Single UBS swarm deployed in B_a to cover random users within a finite isolated area B_r. B_a and B_r are parallel concentric disks with the same radius r_a. . . . 47

3.3 Illustration of the system and the 3D beamforming parameters. The down tilt angle ω is identical for all UBSs' antenna pattern. A_i represents the location of an arbitrary UBS and A_0 represents the serving UBS, which can be in LoS or NLoS connection. The typical user is situated at the point $\mathbf{x}_0$, which is located at a distance y_0 from the origin. 50

4.1 Illustration of downlink UBS with SU-MIMO and MU-MIMO systems. 58
4.2 Downlink MU-MIMO beamforming. 59
4.3 Illustration of the VHetNet with 3D blockages of buildings. 61
4.4 3D blockage model and view of the benefit of the UBSs's altitude to prevent obstructed connection. 62
4.5 LoS probability vs. UBS height for different blockage densities. 66
4.6 Illustration the sectored antenna model used to approximate the beamforming patterns. The red line shows a more realistic antenna model. The blue line shows the approximation taken into consideration. 67
4.7 Distance from the typical user and the BS in each tier. 68

5.1 Coverage probability vs. SINR threshold with different number of SA UBSs ($h = 80$ m). 80
5.2 Coverage probability vs. UBS's altitude with different radius r_a. 80
5.3 Coverage probability vs. Tilt angle ω. 81
5.4 Coverage probability vs. the distance from the typical user to origin with different UBS altitudes. 83
5.5 Optimal Number of SA UBSs K_{opt} vs. the isolated region radius ($\omega = 30°$). . . 83
5.6 Network spectral efficiency vs. the number of SA UBSs K with different tilt angle ω ($h = 80$ m). 84
5.7 Association probability vs. user distribution's standard deviation and UBS altitude h ($\overline{H}_B = 20$ m). 93
5.8 Coverage probability without shadowing vs. SINR threshold $\mathcal{T}$ (dB) ($\overline{H}_B = 30$ m). 95
5.9 Coverage probability vs. SINR threshold with manageable scenario ($\alpha = 4$, Rayleigh fading). 96
5.10 Coverage probability vs UBS altitude. 97
5.11 Coverage probability with/without shadowing vs UBS altitude h for different variance of the shadow power σ_G^l ($\bar{H}_B = 30$ m). 98

5.12 Coverage probability with/without shadowing vs assisting UBS number N with different h. 99
5.13 Coverage probability vs assisting UBS number N for different r_a and p ($\bar{H}_B = 30$ m). 99
5.14 Coverage probability. vs blocage density. 101
5.15 Area spectral efficiency vs. the number of assisting UBS N and the number of antennas N_a. 102
5.16 Coverage probability vs. tilt angle, compraraison between 2D and 3D beamforming technologies for different p and altitude h ($\theta_d = 6°$, $SLL = 18$ dB°). . 103

List of Tables

1.1 5G's main performance indicators. 8
1.2 A brief comparison of UAV networks and terrestrial networks. 13
1.3 Prototypes of UAV communication and their key features. 18

5.1 3D beamforming based UAV swarm networks simulation parameters. 79
5.2 VHetNets with a 3D blockage model simulation parameters. 92

List of Abbreviations and Acronyms

A2A	Air-To-Air
A2G	Air-To-Ground
ASE	Area Spectral Efficiency
BPP	Binomial Point Process
BS	Base Station
C2A	Cellular-To-Air
CCDF	Complementary Cumulative Distribution Function
CDF	Cumulative Distribution Function
CSI	Channel State Information
D2D	Device-To-Device
eMBB	Enhanced Mobile Broadband
G2G	Ground-To-Ground
GA	Genetic Algorithms
GBS	Ground Base Station
GWO	Grey Wolf Optimizer
HAP	High Altitude Platform
HetNet	Heterogeneous Network
HPPP	Homogeneous Poisson Point Process
ICI	Inter-Cell Interference
IHPPP	Inhomogeneous Poisson Point Process
IMT	International Mobile Telecommunications
IoT	Internet of Things
IP	Interference Protocol
LAP	Low Altitude Platform
LMDS	Local Multi-point Distribution Service

LoS	Line-of-Sight
MAP	Medium Altitude Platform
MIMO	Multiple-Input-Multiple-Output
MCM	Multi-Carrier Modulation
MCP	Matern Cluster Process
mMTC	Massive Machine Type Communication
MmWave	Millimeter Wave
MU-MIMO	Multiuser Multiple-Input-Multiple-Output
NLoS	Non Line-of-Sight
NSE	Network Spectral Efficiency
NTN	Non-Terrestrial Network
OFDMA	Orthogonal Frequency Division Multiple Access
PCP	Poisson Cluster Process
PDF	Probability Density Function
PGFL	Probability Generating Functional
PP	Point Process
PPP	Poisson Point Process
PSO	Particle Swarm Algorithm
QoS	Quality of Service
ROP	Random Object Process
SA	Simultaneously Active
SE	Spectral Efficiency
SINR	Signal-To-Interference-Plus-Noise Ratio
SIR	Signal-To-Interference Ratio
SNR	Signal-To-Noise Ratio
SU-MIMO	Single User MIMO
TCP	Thomas Cluster Process
URLLC	Ultra-Reliable Low Latency Communication
UAV	Unmanned Aerial Vehicle
UBS	UAV-mounted Base Station
UE	User Equipment
VHetNet	Vertical Heterogeneous Network
WCDMA	Wideband Code Division Multiple Access
ZFBF	Zero Forcing Beamforming

1G	First Generation
2G	Second Generation
3G	Third Generation
4G	Fourth Generation
5G	Fifth Generation
3GPP	3nd Generation Partnership Project
2D	Two-Dimensional
3D	Three-Dimensional

List of Mathematical Notations

$\exp(.)$	Exponential function
$\Gamma(.)$	Gamma function
$\mathbb{P}(.)$	Probability function
$\mathbb{E}(.)$	Expectation function
$\mathcal{L}(.)$	Laplace transform
$f_X(.)$	Probability density function of X
$F_X(.)$	Cumulative distribution function of X
$\bar{F}_X(.)$	Complementary cumulative distribution function of X
Φ_G	HPPP of GBS locations
Φ_U	BPP of UBS locations
Φ_K	BPP of the simultaneously active UBS locations
Φ_C	PCP of user locations
Φ_B	HPPP of buiding locations
M_j	2D GBS location
A_i	3D UBS location
λ_G	Densisty of GBSs
λ_B	Densisty of buildings
P_G	Transmit powers of GBSs
P_U	Transmit powers of UBSs
A_0	Serving UBS location
u	Typical user
$\mathbf{x}_0$	Typical user location
y_0	Distance from the typical user to the origin
σ_u	Standard deviation of the user distribution
GBS_0	0^{th} tier of GBS: the center of the representative cluster
GBS_1	1^{st} tier of GBS: the other cluster centers

B_r	Finite disk representing the isolated region
B_a	Finite disk where UBSs are distributed
B_g	Finite disk representing the hotspot area
r_a	Radius of the finite disks B_a, B_r and B_g
N	Number of UBSs
K	Number of simulataneously active UBSs
N_a	Number of transmit antennas
N_u	Number of simultaneously served UEs
M	Array gain for zero forcing beamforming
h	UBSs's altitude
$\overline{H}_B$	Buildings average height
L	Length of the buildings
W	Width of the buildings
p	city's blockage density index
α_t^l	Path loss exponent in tier t
Υ_t^l	Path loss gain in tier t
φ_l	Additional path loss for
m_t^l	Nakagami-*m* fading parameter for tBSs
h_t^l	Fading channel gain for tBSs
$\hat{h}_U^l$	Fading channel gain for the interfering UBS
N_0	Additive white gaussian noise signal power
S_t^l	Log-normal shadowing
$\sigma_{S_t^l}^{l^2}$	Variance of the shadow fading
ω	Down tilt angle
θ_d	Half-power beamwidth
SLL	Side lobe level
g_t	Main-lobe gain
s_t	Side-lobe gain
θ_t	Main-lobe beamwidth
$\mathcal{T}$	SINR threshold

Introduction

Radio systems have undergone significant technological advancements in the past two decades, propelled by the burgeoning number of subscribers, and evolving user expectations. This evolution in mobile communication began with the introduction of analog cellular phones in the first generation (1G), which offered only unsecured public voice services, and progressed to the second generation (2G), which introduced digital systems capable of supporting both text messaging and data services. [1]. To enhance data connectivity, third-generation (3G) was introduced, offering videoconferencing capabilities and data transfer speeds of up to 200 Kbps. The wideband code division multiple access (WCDMA) technique [2] was used to transmit a large amount of data across a wide frequency band. The advent of fourth generation (4G) has brought ultra-broadband Internet access with speeds of up to 100 Mbps [3, 4]. The 4G is an IP (Internet Protocol)-based technology that uses the orthogonal frequency division multiple access (OFDMA) technique [5]. Following the global success of 4G, the fifth generation (5G) has been explored to introduce a progressive version of the 4G/IMT (International Mobile Telecommunications)-Advanced standards [6].

5G and future networks are ushering in a new era of the Internet of Intelligence. The number of interconnected devices is expected to be more than 30 billion by 2025 and exceed 100 billion by 2030, encompassing both human and machine communications e.g. drones, sensors, vehicles [7] and an average achievable data rate of over 100 Mbps. In this context, several key enabling technologies have been identified to successfully drive 5G including millimeter-wave (mmWave) communications, multiuser Multiple-Input-Multiple-Output (MU MIMO), beamforming, [8–13] and energy harvesting [14].

The major challenge for 5G cellular networks is to provide seamless and widespread coverage, along with dependable, long-lasting, and reliable connectivity. Inadequate coverage planning can adversely affect the performance of low-latency applications. Wireless networks that rely on mmWave communication are highly susceptible to attenuation caused by increased propagation loss and shadow effects resulting from physical obstacles such as building blockages and human-body blockages. These factors can significantly deteriorate coverage performance. Therefore, it is important to consider the impact of both natural and man-made obstacles on the

coverage area. Additionally, in emergency and hotspot scenarios or any temporary events that necessitate the intensive use of network resources such as popular sporting events or outdoor concerts, or following a natural disaster that requires emergency measures, the network becomes congested. In such scenarios, it is necessary to guarantee a sufficient bandwidth to the majority of users to provide continuous wireless connectivity promptly and efficiently, within reasonable limits. Providing reliable coverage in remote and isolated regions is another complex challenge that mobile networks must address.

Early efforts focused on improving network capacity and coverage by using ultra-dense small cell networks [15–17] and device-to-device (D2D) communications [18, 19]. Nevertheless, these solutions have limitations despite their benefits. For instance, ultra-dense small cell networks encounter challenges with backhaul, interference, and network modeling. Furthermore, relying on terrestrial infrastructure can be challenging due to its high operational costs and vulnerability to volatile environments [20]. To achieve successful D2D communication, better frequency planning and resource utilization in cellular networks are required. Furthermore, the short communication range of devices limits D2D communication performance.

Technological advances in recent years have enabled the rapid expansion of the use of UAVs (Unmanned Aerial Vehicles) in various sectors including telecommunications, traffic monitoring and remote sensing [21–25]. UAVs can be integrated into the wireless infrastructure as aerial base stations (UBSs) [26, 27], a promising technological innovation that can assist ground base stations (GBSs) in overcoming their shortcomings and enhancing coverage, thereby creating a vertical heterogeneous network (VHetNet). The low cost, maneuverability, hovering capability, and high line-of-sight (LoS) connectivity of UBSs enable them to enhance the quality of services (QoS), can compensate for cell congestion during peak hours and emergency situations, and compared to traditional fixed infrastructure, they provide autonomous and highly dynamic architectures for new infrastructure, especially in isolated regions [28].

UBSs can play a crucial role in enabling mmWave communications by reducing propagation loss. They can be viewed as flying antenna systems that facilitate MU-MIMO due to their antenna positions and their ability to be deployed to specific locations on demand. In addition, combining UBSs with beamforming techniques can greatly reduce the inter-cell interference (ICI). However, the literature has not fully analyzed the incorporation of three-dimensional (3D) beamforming techniques into UAV networks to enhance coverage by leveraging both the vertical and horizontal dimensions [29].

The Wyner model used in the literature [30,31], is not an appropriate tool for network modeling. Its oversimplification and one-dimensionality result in significant fluctuations in the signal-to-

interference-plus-noise ratio (SINR) value. Stochastic geometry has become a powerful tool for comprehensive mathematical modeling and performance analysis of cellular networks, due to the irregularity of BS (Base Station) and user locations [32–36]. This approach helps to characterize network operation and understand behavior across multiple spatial realizations, where the network's nodes are positioned based on a probability distribution. In cellular network modeling, Andrews *et al.* [37] were the first to use stochastic geometry tools with a Poisson point process (PPP)-based modeling method. This approach has since become popular for extracting average network performance trends [38–41]. PPP-based modeling is commonly used in infinite regions when there are no specific constraints on BS distribution. However, unlike GBSs, which are deployed over a wide area, UBSs are typically deployed regionally, making the Binomial Point Process (BPP) model more appropriate for UBS use cases [42]. In the other hand, Ying et *al.* [43] concluded that the Poisson cluster process (PCP) was the best stochastic model for users in densely populated urban areas.

Therefore, a comprehensive study is necessary to accurately model systems, analyze coverage, and develop new techniques for mmWave UAV-assisted cellular networks, which is the thesis' primary focus.

Several research projects have focused on the stochastic geometry analysis of UAV-assisted cellular networks. Alzenad and Yanikomeroglu [44] and Turgut *et al.* [45] analyzed the performance of VHetNets in dense urban environments using the PPP-based model, however without taking into account the blockage and shadowing effects. Wang *et al.* [46] analyzed the downlink performance of UAV-assisted cellular networks considering probabilistic LoS/NLoS propagation without adopting any technology to boost the channel propagation. Cherif *et al.* [47] have adopted a directive beamforming and have analyzed the coverage of an aerial user in VHetNets. Although these aforementioned works assumed a finite number of UBSs modeled as BPP, they did not analyze the coverage in congested networks. To the best of our knowledge, few studies have addressed the 3D blockage effect. Recently, Tang et *al.* [48, 49] have analyzed the 3D blockage effects of buildings in urban UAV networks. Nevertheless, the authors did not consider the shadowing effects and they only considered the UBS tier in LoS propagation.

In this thesis, motivated by the aforementioned considerations, we elaborate tractable analytical frameworks for analyzing downlink 3D mmWave cellular networks in two different scenarios with a special focus on enhancing the 3D coverage probability and spectral efficiency. To this end, we focus on three stochastic geometry tools: PPP for GBS location modeling, BPP for UBS location modeling and PCP for user location modeling in hotspot areas. In particular, two new 3D space models for UAV-assisted cellular networks are proposed that adopt various

new technologies to mitigate interference and improve the performance. The analysis is conducted under the Nakagami-*m* fading model, which incorporates both LoS and non-line-of-sight (NLoS) transmissions. This approach allows for the capture of the distinctive characteristics of mmWave communications, which are particularly susceptible to fading and path loss.

- The first model considers a single swarm of UBSs using 3D beamforming technology in an isolated region where wireless connectivity cannot be achieved with traditional GBSs. The number of simultaneously active UBSs reusing the same resource block is determined to enhance the spectral efficiency.

- The second model introduces a 3D blockage model on VHetNets in hotspot areas where the users are clustered around the GBSs. New formulas for LoS/NLoS probabilities were developed that accurately characterizes the 3D blockage effects. The combination of 2D/3D beamforming and MU-MIMO technologies is adopted.

This thesis adopts the max-power association policy and includes a detailed derivation of the probability density function (PDF) of distances, association probabilities, overall coverage probability, and spectral efficiency. Monte Carlo simulations are presented to confirm the accuracy of our framework and the advantages of each proposed network model are investigated.

Thesis Organization

The remainder of this thesis is organized as follows

Chapter 1 provides an overview of existing coverage methods and network architectures. It also discusses the advantages of UAV communications over terrestrial networks, as well as their applications in academia and industry. Finally, it covers the tools, theorems, and applications of stochastic geometry in the context of wireless communication.

Chapter 2 presents the criteria and factors to be considered when deriving the coverage probability based on the stochastic geometry theory. It encompasses a variety of channel propagation models and their respective characteristics. Analytical and simulation methods for deriving and evaluating performance are discussed.

Chapter 3 introduces the UBS swarm model, which is applied to a finite, isolated region. It provides a comprehensive description of the new beamforming technologies that are included in the model. The chapter describes the system model and assumptions, and then proceeds to present the SINR formulation and a derivation of the relevant distance distributions.

Chapter 4 proposes a VHetNet model in hotspot areas under the 3D blockage effects of buildings. It exposes the limitations of mmWave communications and their sensitivity to blockages and details the MU-MIMO technology in UAV networks. The system model and the SINR model were provided, and the derivation of the serving and interfering distance distributions was presented.

Chapter 5 provides a performance analysis of the two proposed models. First, the derivation of downlink coverage probability and spectral efficiency based on the association probabilities and the conditional coverage probabilities is presented. Subsequently, the analytical results, which have been validated by Monte Carlo simulations, are presented and discussed in detail.

Finally, general conclusions and perspectives are provided.

Research Outcome

Journal papers

1- D. Alkama, M. Azni, M. A. Ouamri, and X. Li, "Modeling and Performance Analysis of Vertical Heterogeneous Networks under 3D Blockage Effects and Multiuser MIMO Systems," IEEE Transactions on Vehicular Technology, 2024. DOI: 10.1109/TVT.2024.3366655.

2- D. Alkama, M. A. Ouamri, M. Azni, and X. Li, "Coverage and Network Spectral Efficiency Analysis for UAV Swarm Under 3D Beamforming in Isolated Regions," Telecommunication Systems, 2024. DOI: 10.1007/s11235-024-01173-y

3- D. Alkama, M. A. Ouamri, M. S. Alzaidi, R. N. Shaw, M. Azni, and S. S. Ghoneim, "Downlink performance analysis in MIMO UAV-cellular communication with LOS/NLOS propagation under 3D beamforming," IEEE Access, vol. 10, pp. 6650–6659, 2022. DOI: 10.1109/ACCESS.2022.3142529.

International Conference

1- D. Alkama, M. A. Ouamri, L. Alkama, and M. Azni, "Cellular-Connected UAVs : Coverage Analysis using SWIPT and Up-Tilted Antenna," in 2023 Electrical Engineering International Conference EEIC'23, pp. 641–645, 2023. ISBN: 978- 9969-9732-0-4.

2- D. Alkama, S. Zenadji, M.A. Ouamri, A. Khireddine, M. Azni "Performance of Resource Allocation for Downlink Non-Orthogonal Multiple Access Systems in Tri-Sectorial Cell," 2022 IEEE International Conference on Electrical Sciences and Technologies in Maghreb (CISTEM). Vol. 4. IEEE, 2022. DOI: 10.1109/CISTEM55808.2022.10043956.

Chapter 1

Deployment and Coverage Analysis of Heterogeneous Cellular Networks

Contents

1.1 Introduction **7**
1.2 Coverage Concept in Cellular Networks **7**
1.3 Coverage Methods in Cellular Networks **8**
1.3.1 Heuristic Methods 8
1.3.2 Stochastic Geometry Based Methods 9
1.4 Heterogeneous Networks **9**
1.4.1 Terrestrial Heterogeneous Networks 10
1.4.2 Vertical Heterogeneous Networks 11
1.5 Aerial Networks vs Terrestrial Networks **12**
1.6 Unmanned Aerial Vehicles Communication **12**
1.6.1 UAV Categories 13
1.6.2 UAV Applications 16
1.6.3 UAV Communications in Industry 17
1.7 Stochastic Geometry Tools **18**
1.7.1 Point Process Theory 18
1.7.2 Random Shape Theory 26
1.8 Conclusion **27**

1.1 Introduction

The deployment of the dense cellular infrastructure has led to the use of aerial networks or non-terrestrial networks (NTN). The mobility and highly flexible deployment of UAV networks enable them to enhance the probability of having a direct connection with users in the face of obstacles. In comparaison to typical terrestrial networks, UAVs have the potential to enhance wireless network coverage and increase capacity as needed. Additionally, they facilitate a multitude of innovative applications.
In this chapter, we provide an overview of the coverage concept and the existing coverage methods in cellular networks. We then illustrate the different network architectures of 5G and future networks, which include heterogeneous networks. Furthermore, we present the advantages and limitations of aerial networks over terrestrial networks and discuss the fundamentals of UAV communications and their applications in both academia and industry. Finally, we introduce the various stochastic geometry tools (Point processes and random shape theory) used in the literature for wireless communication modeling and describe the main mathematical properties and the useful theorems that can be applied.

1.2 Coverage Concept in Cellular Networks

Several companies, such as DOCOMO, Ericsson, Vodafone, and Huawei, have made noteworthy investments in the development of 5G networks. According to IMT-2020, 5G use cases can be divided into three categories [50]

— Enhanced Mobile Broadband (eMBB): facilitate large-scale data applications and enable support for extensive device and user capacity for wireless broadband services.

— Massive Machine Type Communication (mMTC): enables a significant number of wireless device connections, while also enhancing energy efficiency and reducing the cost per device.

— Ultra-Reliable Low Latency Communication (URLLC): such as unmanned vehicles and smart factories, are capable of maintaining full coverage and operating times.

The coverage network is provided through BS antennas located worldwide, which allow a wireless telecommunications to reach end-users [51]. The concept of cellular networks allows for efficient use of the radio spectrum and enables seamless handover as users move between cells, ensuring continuous connectivity [52]. The coverage of each BS is determined by its configuration and extends to a particular surrounding area. The range of the BS serving area is strongly

Table 1.1: 5G's main performance indicators [53].

Performance indicators	**Requirement**	**Category**
User experienced Data Rate	50 Mbps (UL), 100 Mbps (DL)	eMMB
Peak Data Rate	10 Gbps (UL), 20 Gbps (DL)	eMMB
Spectral Efficiency	15 bit/s/Hz (UL), 30 bit/s/Hz (DL)	eMMB
Connection Density	10^6 devices/Km^2	mMTC
Latency	4 ms for eMMB, 1 ms for URLLC	eMMB, URLLC
Reliability	1-10^{-5}	URLLC
Mobility	up to 500 Km/h	eMMB

affected by the BS's transmit power, carrier frequency, antenna tilt, deployment type, and environmental conditions. Moreover, it is important to consider the impact of natural and man-made obstacles, such as trees, buildings, hills, and mountains, in the coverage area.

The cell densification in 5G terrestrial networks requires an expensive installation with a high degree of latency. Therefore, providing reliable coverage remains an important challenge to be addressed. Technical requirements and deployment scenarios are important considerations for 5G technical concept. For instance, in high population density areas, cells are usually smaller and have less coverage and significant traffic capacity is crucial, while mobility may be less of a priority. Furthermore, the user data rate should be higher than that of wide area coverage. Conversely, in sparsely populated rural areas, cells tend to be larger and have wider coverage. It is important to note that as cell size decreases, the quantity of data sent between BSs increases. Table 1.1 lists the key performance indicators required for 5G cellular networks.

1.3 Coverage Methods in Cellular Networks

Two distinct approaches may be employed to investigate the coverage problem in cellular networks: heuristic methods and stochastic geometry-based methods.

1.3.1 Heuristic Methods

Heuristic approaches are employed to identify approximate solutions to complex problems, based on practical procedures or rules of thumb. These methods include "heuristic algorithms," which can be applied to optimize the service coverage of cellular networks. This can be achieved by optimizing the BS locations, the minimum number of BSs, the resource allocation, the handover, or by dynamically adjusting the transmit power levels of BSs and

devices. Among the various metaheuristic methods, we find the simulated annealing method, which involves improving a single solution. In contrast, population-based metaheuristics, such as particle swarm algorithms (PSO), genetic algorithms (GA) and grey wolf optimizer (GWO), involve a set of solutions called a population, that evolve in parallel as iterations progress to exploit the search space [54]. Heuristic methods are distinguished by their simplicity compared to complex mathematical models. However, their ability to come up with the best solution may be limited, leading to suboptimal results. Furthermore, the initial parameters may influence their performance.

1.3.2 Stochastic Geometry Based Methods

Stochastic geometry is a useful discipline of applied probability for investigating stochastic processes and random phenomena. It is a widely used tool in cellular network analysis, it applies mathematical models and relevant statistical techniques to analyze and evaluate random spatial models generated from Point Process (PP) [55–57] or random shape theory [58]. The stochastic geometry-based methods facilitate the comprehension of network behavior by averaging over all network topologies observed from a generic node, weighted by their probability of occurrence. The distribution of nodes in a wireless network (e.g., BSs, access points, user equipment, buildings etc.) is random in space or Euclidean plane and the locations' geometry of the nodes is critical as it affects interference, coverage performance, and determines the signal-to-interference-plus-noise ratio (SINR) at the receiver [32]. The positions of the nodes can be viewed as a realization of certain PPs, therefore, the stochastic geometry tools are perfectly suited for modeling cellular networks to estimate coverage probability performance.

In complex network contexts, stochastic geometry-based methods are more appropriate for comprehensive analysis and optimization, as they frequently yield more accurate estimates of coverage probability in cellular networks in comparison to heuristic methods.
In this thesis, we focus on applying the stochastic geometry-based methods. Section 1.7 provides a detailed analysis of the available stochastic geometry tools.

1.4 Heterogeneous Networks

This section introduces 5G and future network architectures. It focuses on those architectures with the greatest potential for coverage and QoS. Heterogeneous Networks (HetNets) are composed of multiple nodes that operate simultaneously in frequency bands with varying transmission power levels, capabilities, and coverage areas.

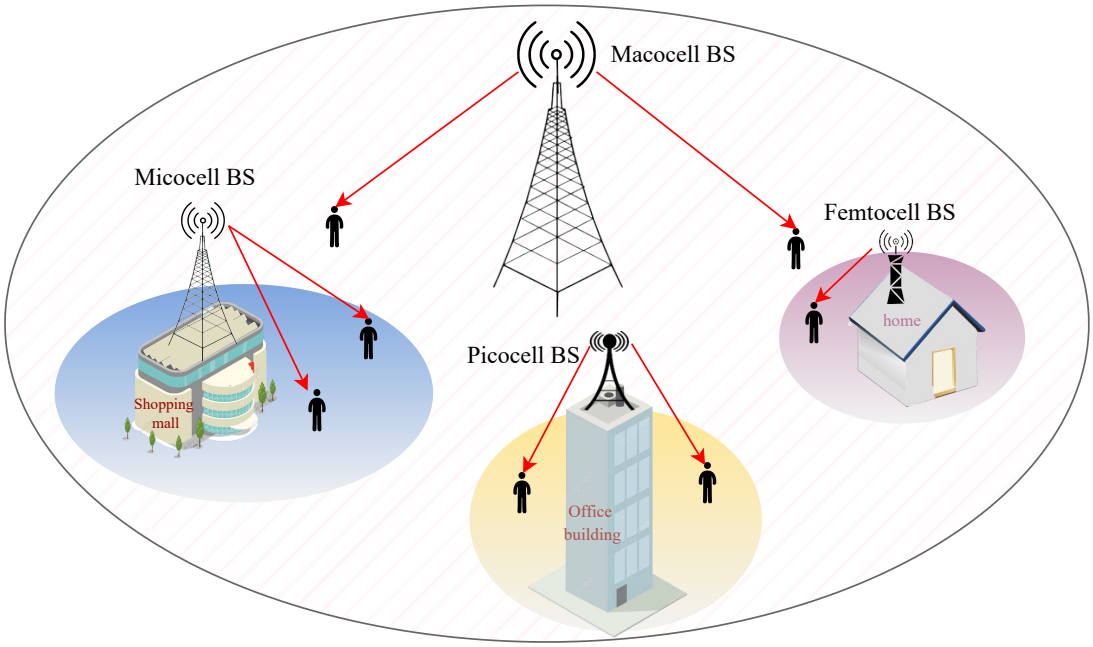

Figure 1.1: Terrestrial heterogeneous network architecture composed of a macro, micro, pico, and femto cell.

1.4.1 Terrestrial Heterogeneous Networks

Terrestrial HetNets (THetNets) offer a distinct advantage over traditional homogeneous terrestrial networks, namely its capacity to facilitate small-cell cooperation within macrocell networks. This enhances the user QoS and increases the possibility of geographic resource reuse. The most straightforward approach to enhancing coverage is the deployment of small cells [17]. This can be achieved by incorporating low-power BSs into the network to address areas that remain uncovered by the macro network. The outcome is a substantial THetNet comprising both large macro cells and smaller cells. The THetNet is comprised of macro, micro, pico, and femto cells, each of which is based on the GBS power, as shown in Figure 1.1.

- **Macrocell networks :** They are capable of providing radio coverage through the use of a high-power BS, which is a common feature of contemporary communication systems. Macro BSs are characterized by sectored antennas, a long transmission distance and a wide coverage area, with cell radii that can extend from approximately 1 km to 25 km [59]. Macro BSs can be used in both rural and urban areas.

- **Microcell networks :** Low-power BSs are used to serve microcell networks, which are typically deployed to increase the network capacity and cover both indoor and outdoor dense areas. The microcells have a transmission radius that is more limited than that of the macro BSs. This typically ranges from a few meters to approximately one kilometer.

- **Picocell networks :** Picocells are defined by their omnidirectional antennas and a maximum power output of 130 milliwatts. Additionally, they exhibit a maximum cell radius of 200 meters. These networks are typically used in outdoor hotspots or office buildings. In addition, they are widely used in Aircraft and Marine.
- **Femtocell networks** : also called home BSs, they comprise small BSs that can be deployed at home or in a small business for very short-range coverage, less than 30 meters [59]. Femtocells feature omnidirectional antennas with a transmit power of approximately 50 milliwatts. The installation of femtocells is significantly more straightforward and more cost-effective than that of macrocells.

1.4.2 Vertical Heterogeneous Networks

5G and future cellular networks are anticipated to comprise a combination of traditional BSs (including macrocells and small cells ...) and aerial BSs operating simultaneously, which we refer to as vertical heterogeneous networks (VHetNets). This is driven by advancements in cellular technologies and the widespread deployment of dense cellular infrastructure. Furthermore, future networks are also expected to integrate terrestrial, aerial, and satellite networks, thereby creating a novel, multi-layered VHetNet architecture, as illustrated in Figure 1.2.

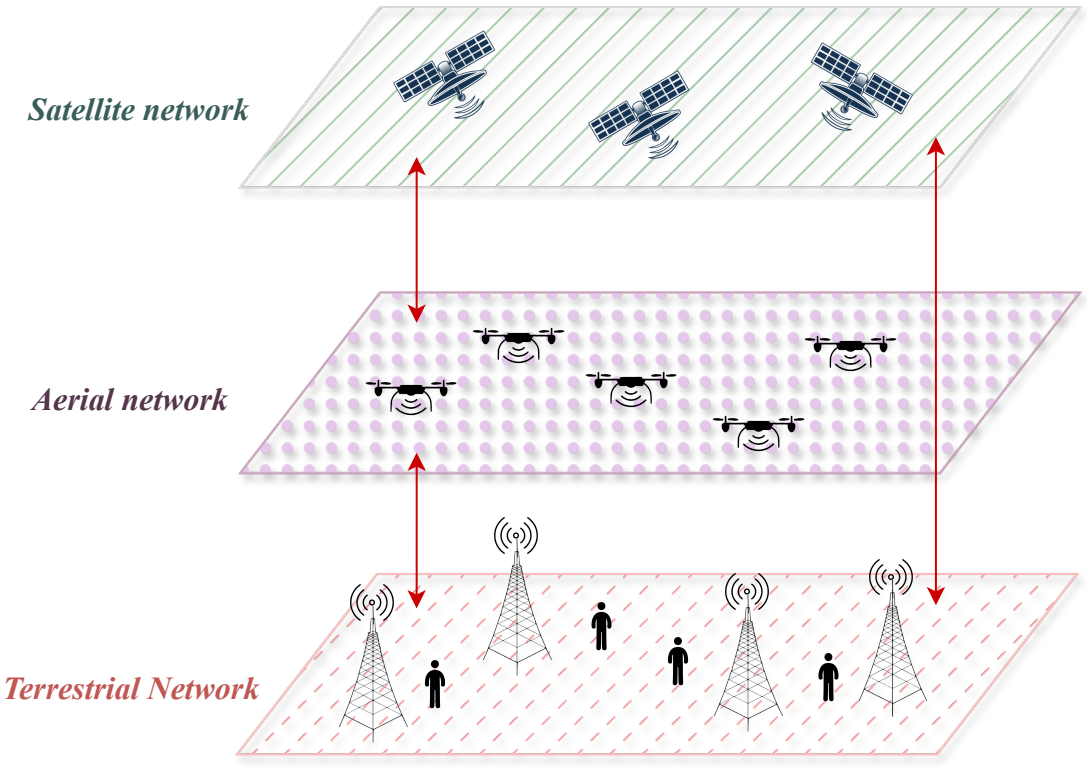

Figure 1.2: Multi-layered VHetNet architecture comprised of aerial, satellite and terrestrial networks [60].

UAVs also known as drones are aircraft that can be controlled remotely or programmed to operate autonomously, without a human pilot on board. In contrast to THetNets, the coexistence of UAV-mounted base stations (UBSs) and GBSs has not been extensively studied in the literature. The most significant advantages of using VHetNet are the potential for increased capacity and the ability to provide extensive 3D coverage, particularly in dynamic and challenging environments.

Despite the numerous advantages that the VHetNets offer, they are currently confronted with several challenges. One such challenge is the differing behavior of propagation channels in aerial and terrestrial networks. Another challenge is the potential for vertical altitude variations in UBSs, even for static UBSs, which could result in changes to their geometry. Therefore, it is important to fully understand the impact of UBS altitude on VHetNet performance. In addition, VHetNets must have mechanisms that can easily adapt to changes in their workplace.

1.5 Aerial Networks vs Terrestrial Networks

UAV networks and terrestrial networks operate in different environments. Therefore, extensively researched findings on terrestrial networks may not be directly applicable to forthcoming 3D UAV wireless networks. The UBS tier and GBS tier differ in their transmit powers, densities, distributions, path loss exponents, fading parameters, and association schemes. An advantage of aerial BSs is that their altitude can be increased to mitigate signal blockage caused, for example, by high-rise buildings. UBSs can serve multiple purposes, including offloading GBSs in densely populated areas and extending coverage to remote regions, typically underserved by cellular networks due to limited operator incentives [61].

Fotouhi *et al.* [62] conducted a thorough study on integrating UAVs into cellular networks, addressing major challenges such as deploying aerial BSs, developing UAV communication prototypes, and ensuring security. Table 1.2 summarizes the various advantages and challenges of UAV networks compared to terrestrial networks.

1.6 Unmanned Aerial Vehicles Communication

It is anticipated that the global market for commercial UAVs will undergo substantial growth, from $19.3 billion in 2020 to $45.8 billion in 2025 [26]. The projected value of the global UAV payload market, encompassing military drones, is anticipated to reach $3 billion by 2027. This payload comprises various equipment carried by UAVs, including cameras, sen-

Table 1.2: A brief comparison of UAV networks and terrestrial networks.

UAV networks	**Terrestrial networks**
Operate in the air.	Operate in the ground.
Mostly unrestricted locations.	Selected locations.
Highly mobile with adaptive altitude.	Static and fixed infrastructure.
Easy deployment with low cost installation.	Complex infrastructure and costly installation.
High LoS communications.	Prone to blockages.
Restricted flight time and payload capacity.	Extensive and long-term network coverage.
Adaptable coverage range.	Fixed coverage area.
Deployed rapidly to specific locations.	Limitations in reaching remote areas.
Temporary communication needs.	Continuous communication needs.

sors, radars, communications devices, among others [63]. UAV-based solutions are increasingly competitive in emerging markets and have sparked substantial interest from both academia and industry. In this section, we discuss the various categories and applications of UAVs.

1.6.1 UAV Categories

Federal aviation regulations and the environmental characteristics must be carefully evaluated when determining the most suitable type of UAV for a specific application, especially to meet QoS, requirements. To attain this objective, it is essential to analyze the UAVs' flight mechanism and their maximum altitude.

In some countries, such as Australia and China, the practical authorization for small UAVs to fly cannot exceed an altitude of 120 meters to reduce the potential danger to manned aircraft [64, 65]. The literature typically categorizes UAVs according to their flying mechanism, and operational altitude. The following classification is detailed accordingly.

"DJI Mavic" rotary wing

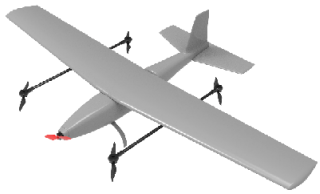

"V220 VTOL" fixed-wing

"Parrot Swing" hybrid fixed/rotary wing

Figure 1.3: UAV classification based on flying mechanism and structure [66].

Types of UAV based on Flying Mecanism

1. **Rotary-wing UAVs**

   Also called multirotor UAVs, they use multiple rotor blades, and take off and land in a vertical position such as quadrotor drones. They can hover and remain stationary over a specified area [64]. Consequently, the use of multirotors as aerial BSs is an attractive solution for mobile network support in emergencies. However, because these UAVs are constantly battling gravity, their energy consumption is high and their mobility is limited [62]. In addition, their structure is relatively complex.

2. **Fixed-wing UAVs**

   They feature a simple structure with rigid wings, allowing them to have enhanced flexibility, mobility, and endurance, such as small airplanes. However, unlike rotary-wing UAVs, they are heavier and faster, and they cannot hover over a fixed area, they need a runway to take off and land, which puts them at a disadvantage [67].

3. **Hybrid fixed/rotary-wing UAVs**

   Hybrid fixed/rotary-wing UAVs have recently emerged in the market to balance the capabilities of fixed-wing and rotary-wing UAVs. These types of UAVs are capable of vertical takeoff, swift traversal through gliding, and seamless switching to hovering mode with the assistance of four rotors.

Figure 1.3 shows examples of rotary-wing, fixed-wing, and hybrid fixed/rotary-wing UAVs.

Types of UAV based on Altitude

1. **High Altitude Platforms (HAPs)**

   These UAVs are typically conceived for long-term service (can be kept in the air for several months) and are mostly quasi-stationary, flying at relatively high altitudes as balloons and large UAVs. They typically operate in the stratosphere, dozens of miles above the Earth's surface [68]. More precisely, their altitude ranges from 15Km to 25Km. HAPs are intended to provide Internet connectivity, a long communication persistence and wide bandwidth to ensure extensive coverage of wide geographic areas such as rural environments, that are not currently served by cellular networks. In addition, despite the advantage that HAPs offer in ensuring a high probability of unblocked links, they are still com-

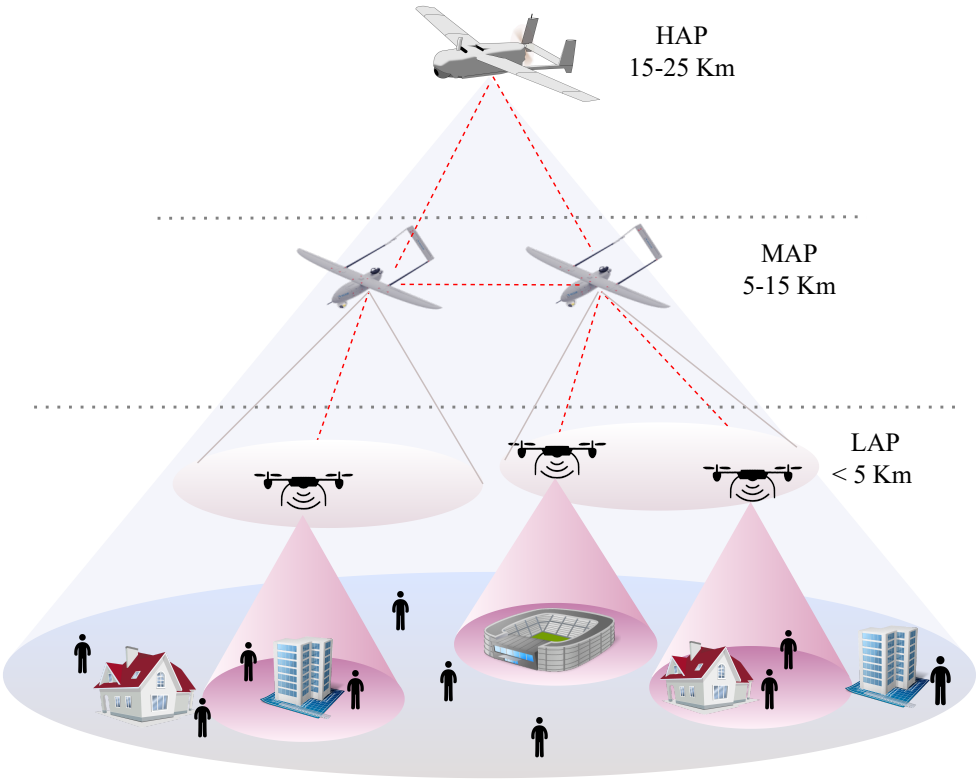

Figure 1.4: Network architecture of HAPs, MAPs, and LAPs.

plex to deploy, as they can generate large-scale ICI that can cause network failure [69]. Consequently, the literature on UAV-based cellular networks rarely tackles them.

2. **Medium Altitude Platforms (MAPs)**

   MAPs operate at altitudes higher than LAPs but lower than HAPs. These platforms typically operate between 5 Km and 15 Km above ground level. MAPS can remain airborne for extended periods and carry heavier payloads to serve as relays between HAPS and LAPS. Their coverage area radius may extend up to 5 Km [61]. Compared to LAPs, MAPs offer an extended coverage range, longer flight endurance capabilities, enhanced stability, and connectivity. They are extensively used for military aerial surveillance and reconnaissance operations.

3. **Low Altitude Platforms (LAPs)**

   LAPs are extensively studied in the literature [65, 70–72]. They are the most widely used to assist cellular communications in time-limited operations, such as emergency services, where flexibility, high mobility or rapid deployment is required. LAPs fly in the lower

troposphere at an altitude of no more than a few kilometers. They suffer from limited battery power, so their lifespan is shorter and their coverage is less than that of HAPs. Conversely, they are less expensive, and their batteries can be easily recharged. Additionally, the use of LAPs reduces shadow effect and provides a significant performance-enhancing advantage due to their ability to establish better LoS communication links over traditional terrestrial networks, and allows for lower path loss than HAPs due to the short-range links that can be achieved. Generally, cooperative small drones dominate LAPs.

Figure 1.4 illustrates the differences between HAPs, MAPs and LAPs.

1.6.2 UAV Applications

UAVs have recently received significant attention in the field of wireless communication [62, 64, 73]. They find extensive application across various domains, serving varied objectives. The use of UAV-mounted wireless equipment depends on the specific application context. They may function as aerial user within cellular-connected UAVs, harmoniously coexisting with ground users relying on existing cellular networks, or may be incorporated into the wireless infrastructure as flying BSs or aerial relays, as illustrated in Figure. 1.5.

Aerial User

UAVs serve as mobile terminals in cellular networks to establish dependable and secure connection in several applications, including surveillance, package delivery and real-time data transmission. For example, a UAV equipped with a sensor can be a cost-effective solution for monitoring, delivery and data collection. The prime benefit of UAV-users lies in their capacity to rapidly navigate and streamline their trajectory to effectively accomplish their missions [64]. Studies [74–77] have investigated the coexistence of aerial and ground users in a cellular network. The authors analyzed design specifications that would allow cellular network operators to modify their networks to accommodate aerial users.
In our recent work [78] we have proposed a model featuring up-tilted antennas applied in terrestrial BSs to serve the aerial users instead of using traditional down-tilted antennas.

Aerial Base Station

UBSs represent a prospective technological innovation with the potential to deliver reliable and cost-effective wireless connectivity and a diverse range of services to ground users. The use of UBSs applies to VHetNets, where additional capacity can be provided on demand to extend

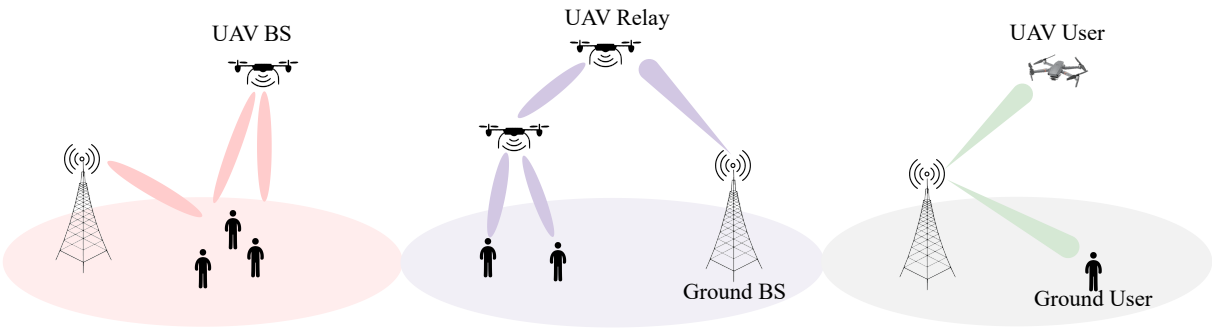

Figure 1.5: Main UAV applications.

coverage in congested terrestrial networks. Furthermore, they can be employed in situations where terrestrial wireless communications are not accessible by ground users.
The literature extensively examines UBSs, optimizing their optimal location [79] and analyzing their 3D deployment [80]. Enayati *et al.* [81] have investigated the optimal altitude of the UBS overlaying a terrestrial network with an energy harvesting system. This study aims to improve the battery life of the UBSs, the channel propagation, and eventually maximize the coverage.

Aerial Relay

Mobile UAVs can serve as aerial relays in mmWave environments that have unfavorable transmission conditions. UAV relays create air-to-air (A2A) communications to enhance transmission between two nodes and ultimately, expand the coverage network. Relative to terrestrial relays, aerial relays have a great ability to establish LoS connections and are exceedingly maneuverable. Furthermore, the backhaul link must be considered for UAV relaying.

In [82], the UAVs have been adopted as relays between the GBS and the user. They used the Friis transmission equation to calculate the received power for the relay path.
The study [83] examined the use of multi-hop UAV relay nodes to connect with ground nodes. It calculated the cascaded propagation loss of the relay link and evaluated the channel capacity.

1.6.3 UAV Communications in Industry

Several companies, including Huawei, China Mobile and Ericsson have conducted UAV experiments using advanced 5G technologies. During exhibitions and commercial events, they have demonstrated various test rigs and prototypes of wireless infrastructure UAVs. These testing platforms aim to enhance user experience and extend coverage to areas lacking terrestrial wireless infrastructure. The projects using UAVs to bring wireless coverage listed in Table 1.3.

Table 1.3: Prototypes of UAV communication and their key features [84]

Prototypes	**Year**	**Main Features**
Facebook Aquila	2016-2018	Provide Internet access to remote areas
China Mobile and Ericsson Prototype	2016	Conduct World's First 5G Drone Prototype Field Trial
Nokia F-Cell	2016	Self-configuring and auto-connecting UAV and provides support for NLoS
Eurecom Perfume	2015-2020	For relay services
Huawei SkySite	2019	5G BS remote radio unit to provide signal coverage to 20-30 km^2 area

1.7 Stochastic Geometry Tools

Stochastic geometry may be applied to assess the effectiveness of 2D and 3D cellular networks in various scenarios, using realistic PPs and random shape theory. This section presents the fundamental tools and concepts of stochastic geometry for modeling VHetNets, THetNets and traditional homogeneous networks. It also includes useful properties and theorems for deriving analytical expressions.

1.7.1 Point Process Theory

Practical geometry applications rely on a set of points randomly distributed in a Euclidean space $\mathbb{R}^d$ of dimension $d \geq 1$, referred to as in the mathematical context as point fields, random point patterns, or point processes. PP theory is recognized as the primary subfield in stochastic geometry and is commonly used in stochastic models. The literature has demonstrated the validity of the PP approximation for real-world cellular networks [85].

PP theory enables the evaluation of the following aspects [32–34, 86]

— Statistical properties of a given set of points,

— The ability to fix a point at a specific location,

— Describe, in general terms, random geometric objects consisting of random unitary elements,

— Minimize error hypotheses based on an empirical set of points.

Assuming that $\{X_i\}$ represents the points of PP Φ which are random variables, Φ can be expressed as a discrete sum of Dirac measures on $\mathbb{R}^d$ [87]

$$\Phi = \sum_i \delta_{X_i}, \tag{1.1}$$

The intensity measure or expectation measure is an essential feature of PP, it refers to the expected number of points within any given set $A \subset \mathbb{R}^d$.

Veronoi Tesslation

The Voronoi tessellation, named after the mathematician Georgy Voronoi, is a valuable geometric tool used in finite element analysis, computational geometry, and spatial pattern analysis. The geometry of the network is divided into distinct, non-uniform zones bounded by the perpendicular bisectors of the line segments connecting each pair of neighboring points. The Voronoi tessellation model differs from hexagonal models in which the BSs are arranged in a deterministic grid, each covering a hexagonal cell of equal coverage area [88], as shown in Figure. 1.6. In reality, sites often deviate from their theoretical positions, making the hexagonal model too idealized. Another drawback, they present mathematical intractability due to the complex numerical calculations involved [37, 89]. In cellular networks, the stochastic model uses the Voronoi tessellation principle to define points representing BSs, which can be randomly or strategically distributed. Each point creates a polygonal region in the Euclidean space known as a Voronoi polygon or Voronoi cell. This makes it a fundamental paradigm for PP theory.

PP can be a mixture of three spatial distribution of network nodes: independent, repulsive, and attractive [90].

- **Independant Distribution**

The transmitters' locations are independently distributed. To describe this distribution, spatial point process models such as Poisson point process and binomial point process models are used.

- **Repulsive Distribution**

In this distribution, wireless transmitters that transmit simultaneously should not be located in close proximity to each other. Repulsion can be caused by various factors, including planned deployment and physical restrictions such as geographic exclusion and terrain occlusion. PP

models, such as lattice processes, Ginibre point processes, and Matérn hardcore point processes, are commonly used to describe this repulsive behavior.

◦ **Attractive Distribution**

Wireless transmitters can be clustered strategically in certain regions, such as in BS-centric user gathering, which creates an attractive distribution that is different from the uniform distribution across the entire plane. To model these attractive spatial distributions, various representative PPs can be used, such as the Thomas cluster process, Matérn cluster process, and Poisson hole process.

In the following, we detail the basic PPs used in this thesis to model the nodes in cellular networks. Additionally, we present some useful theorems used in the derivation of our analytical expressions.

1.7.1.1 Poisson Point Process

The Poisson point process (PPP) is a set of randomly distributed points in a mathematical space. It is the commonly employed PP for cellular network modeling and analysis due to its analytical flexibility, simplicity, and traceability [32, 33], and can provide relevant closed-form expressions. The PPP-based abstraction model is used in cases where there are no specific constraints on the nodes' distribution in the network. Typically, when nodes are not close to each other. This model assumes that wireless nodes are independently distributed without any repulsion or spatial correlation between them.

PPP has key mathematical properties that lead to feasible results. A PP Φ measuring intensity Λ and density λ is a PPP if and only if for any compact set $A \subset \mathbb{R}^d$, the number of points k inside A is a Poisson random variable, and the number of points in disjoint sets are independent.

$$\mathbb{P}\{\Phi(A) = k\} = \frac{\Lambda(A)^k}{k!} \exp\left(-\Lambda(A)\right), \tag{1.2}$$

where $\Lambda(A) = \lambda|A| = \int_A \lambda(y)dy$, with $|A|$ being the Lebesgue measure (area of A).

Special case : If A denotes a circle with radius r, the intensity measure becomes $\Lambda(A) = \lambda\pi r^2$, therefore the Poisson distribution can be written as

$$\mathbb{P}\{\Phi(A) = k\} = \frac{(\lambda\pi r^2)^k}{k!} \exp\left(-\lambda\pi r^2\right), \tag{1.3}$$

A PPP with a uniform density of λ and an intensity measure $\Lambda(A)$, i.e. all the points are independently and uniformly distributed in A, is referred to as a homogeneous Poisson point process

(HPPP) which is a stationary and the simplest PP. Otherwise, it's called an inhomogeneous Poisson point process (IHPPP), which can model non-uniform user distributions in space. In this thesis, we are interested in HPPP.

Figure 1.6 displays both the hexagonal model and the PPP-based model with veronoi cells, where the nodes represents the BS location.

In the context of cellular networks, the HPPP model is commonly used to represent the GBS' positions and the corresponding Voronoi diagram as a structural representation of the cells to illustrate the network planning concept, because GBSs tend to be positioned far apart from each other, and no correlation between them is necessary.

Several research studies have adopted the PPP-based abstraction model and demonstrated that it is capable of accurately reproducing the main structural characteristics of operational cellular networks [91–93].

In [91], the authors compare the deployment of GBSs in urban regions using the PPP model and the grid model. The results demonstrate that the PPP-based abstraction model provides upper bounds for coverage probabilities in urban areas and is more accurate than the hexagonal grid approach.

In [35, 94], Baccelli *et al.*, extensively researched the economic models and architecture of networks, using PPP for the spatial distribution of GBSs.

The PPP-based spatial distribution of GBSs was also adopted in [37] and [38] to analyze and evaluate the key performance metrics of a single-tier network and a multi-tier network, respectively.

Most studies on UAV-assisted cellular networks [95–97] have used the HPPP to depict the arbitrary location of UBSs, without any specific constraints on their distribution. However, this distribution is not suitable for UBSs, which are typically deployed regionally to provide temporary communication services.

We now turn to the fundamental theorems of a PPP, which are very useful for computing the analytical expressions of the network performance.

Probability Generating Functional and Campbell's Theorems

The PP's distribution is characterized by the Laplace functional, which is similar to a characteristic function of a random variable. The Laplace functional of a PP Φ denoted by $\mathcal{L}_\Phi$ is

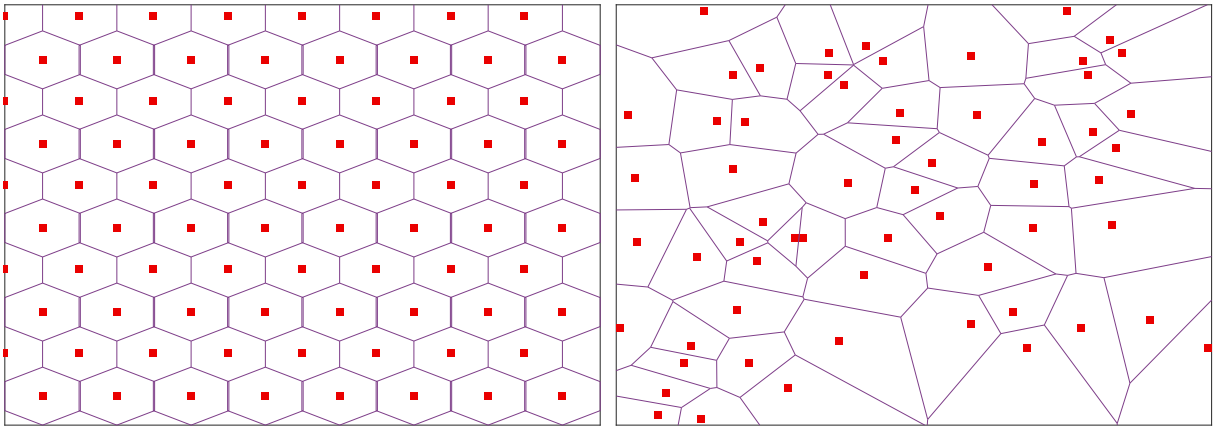

(a) (b)

Figure 1.6: A comparison between a stochastic geometry-based deployment and a hexagonal deployment where the red squares indicate the BS location. (a) The hexagonal model represents the coverage area of the BS as an hexagon, (b) PPP-based BS distribution, the Voronoi cells are presented by polygonal regions.

expressed by the following formula

$$\begin{aligned}\mathcal{L}_{\Phi}(g) =& \mathbb{E}\left[\exp\left(-\sum_{y_i\in\Phi} g(y_i)\right)\right] = \mathbb{E}\left[\exp\left(-\int_{\mathbb{R}^d} g(y)\Phi(dy)\right)\right] \\ =& \exp\Big(-\int_{\mathbb{R}^d}\Big(1-\exp\left(-g(y)\right)\Big)\Lambda(dy)\Big),\end{aligned} \tag{1.4}$$

where g is a positive function defined on $\mathbb{R}^d$.

Denoting G a random variable that is a sum of positive functions f in $\mathbb{R}$ given as

$$G = \sum_{y_i\in\Phi} f(y_i), \tag{1.5}$$

The probability generating functional (PGFL) and Campbell's theorems are vital mathematical techniques for modeling aggregate interference in cellular networks. Campbell's theorem is a valuable tool in probability theory, mainly used to calculate the expectation of a random variable. It is also useful for converting the expectation of a sum of functions to an integral if the random value is equal to a sum such that G in (1.5). Using the expression (1.4), Campbell's and PGFL's theorems for the PPP Φ, can be given as follows

Theorem 1.7.1. *Campbell's theorem for a random variable G can be written as follows*

$$\mathbb{E}\left(G\right) = \mathbb{E}\left(\sum_{y_i\in\Phi} f(y_i)\right) = \int_{\mathbb{R}^d} f(y)\Lambda(dy) = \int_{\mathbb{R}^d} \lambda f(y)dy, \tag{1.6}$$

It is worth noting that the integration limits indicate the boundaries of the area where the PPP exists [39].

Theorem 1.7.2. *The PGFL of a PPP Φ is expressed in a simple, closed-form. This is derived from the expectation of the product of the values of the function G at every point y_i in Φ*

$$\mathbb{E}\left(\prod_{y_i \in \Phi} f(y_i)\right) = \exp\left(-\lambda \int_{\mathbb{R}^d} (1 - f(y))dy\right), \tag{1.7}$$

1.7.1.2 Poisson Cluster Process

The Poisson cluster process (PCP) is a PP constructed from a set of parent points distributed according to HPPP Φ with a set of daughter points clustered around these parent points. In realistic networks, users are not uniformly distributed. For instance, in shopping malls, railway stations, and special events like festivals and soccer matches, users tend to congregate in restricted spaces. In this case, the PPP model cannot accurately represent the geometry of the networks, where correlation between nodes exists.

Ying et *al.* [43] compared the performance of several user modeling methods to find a modeling method that is closer to the real world and depict more realistic scenarios. They concluded that the PCP was the best stochastic model in dense urban and hotspot areas. In this context, the daughter points represent the locations of the users, and the parent point represents the location of the GBSs, as adopted by Chiranjib *et al.* [98]. Daughter points can also depict the location of UAVs assisting an overloaded cellular network, as used by Yao *et al.* [99].

Two specific PCP models are constructed and are commonly used in academic literature: the Thomas cluster process (TCP) and the Matérn cluster process (MCP).

Thomas Cluster Process

In the TCP, daughter points $x \in \Phi_C$ are normally and symmetrically distributed around each parent point $y \in \Phi$ with a standard deviation σ. The probability density function (PDF) for the distance between a daughter point and a parent point is expressed as follows [100]

$$f_X^T(x) = \frac{1}{2\pi\sigma^2} \exp\left(-\frac{\|x - y\|^2}{2\sigma^2}\right), \tag{1.8}$$

Matern Cluster Process

In the MCP, daughter points are uniformly distributed in a disk $D(y, R)$ of radius R centered on each parent point $y \in \Phi$. The PDF of the distance between a daughter point and the parent point can be expressed as follows [101]

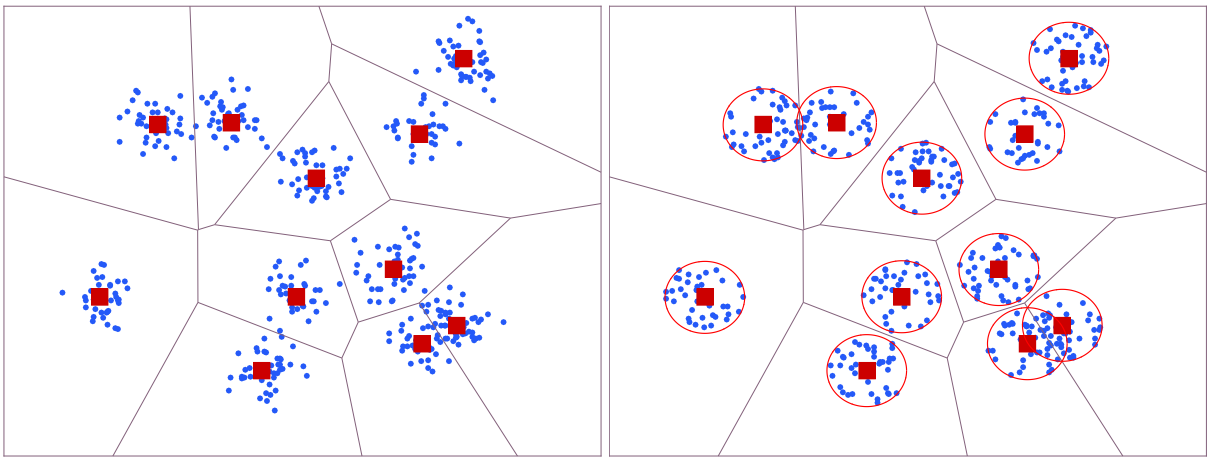

(a) TCP (b) MCP

Figure 1.7: Realization of TCP and MCP through Voronoi tessellation. The red squares represent the parent points, which are GBSs distributed according to the PPP. The green points represent the daughter points, which are users clustered around the parent points.

$$f_X^M(x) = \begin{cases} \frac{1}{\pi R^2}\left(R - \|x-y\|\right) & \text{if } \|x-y\| \leq R, \\ \\ 0 & \text{otherwise}, \end{cases} \tag{1.9}$$

Figure 1.7 depicts the difference in the distribution of daughter points in TCP and MCP.

TCP and MCP were initially developed by Ganti and Haenggi [102] to simulate node positions in clustered wireless ad hoc networks. Since then, they have been adopted in various networks, including D2D networks [103], THetNets [104, 105], cognitive networks [106], and UAV networks [107]. However, research on the use of PCP in VHetNets is still in its early stages.

Wang *et al.* [14] adopted both TCP and MCP for the distribution of the users in UAV-assisted mmWave cellular networks and the ground projections of the UAVs are the parent nodes. The performance was evaluated using both models, and the numerical results showed that TCP and MCP generally lead to similar network performance trends. This demonstrates the insight that considering PCP rather than PPP is key to capturing the user distribution.

Mankar *et al.* [108] have analyzed the coverage in random wireless networks, considering a correlation between the ground users and the BSs. The study demonstrated that TCP is a more appropriate method for distributing users when the standard deviation is small. Furthermore, it was shown that as the standard deviation tends to infinity (i.e. users are not clustered around BSs), the TCP model transitions to the PPP model.

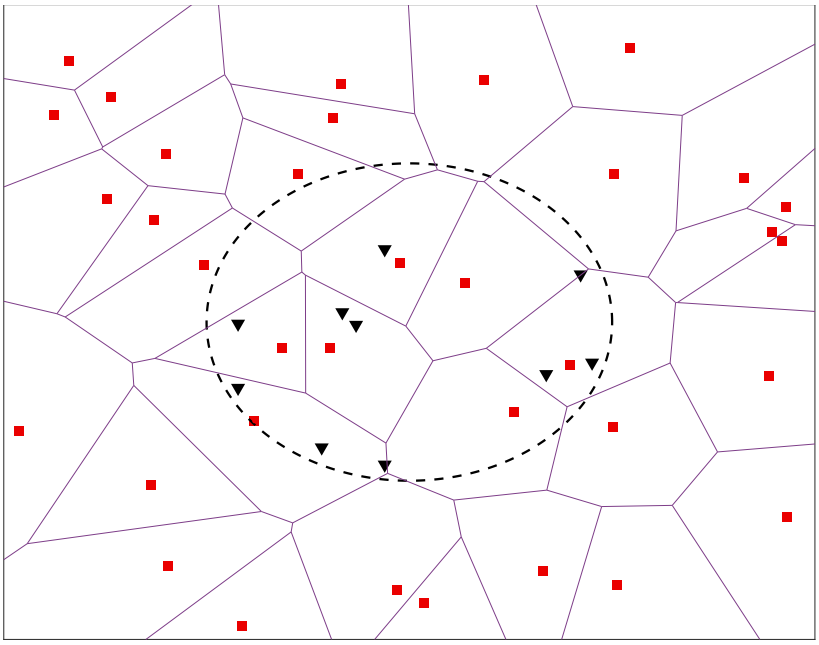

Figure 1.8: A top view snapshot of UAV-assisted cellular network. The black triangles represent the UAVs distributed by BPP in a finite circular region and the GBSs shown as red squares generated by PPP.

Yang *et al.* [105] have analyzed the wireless THetNets in dense areas, with interference management. The macro BSs and small BSs are distributed following a HPPP and the users are clustred around the macro BSs and small BSs forming two TCPs respectively.

1.7.1.3 Binomial Point Process

A binomial point process (BPP) is a PP typified by finite-dimensional distributions. Within a bounded set $A \subset \mathbb{R}^d$, a fixed number of points N are independently and identically distributed. The BPP originates from the HPPP, as demonstrated in [36]. This derivation focuses on restricting HPPP Φ to a subset $W \subset A$ that contains precisely k points, i.e. $\Phi(W) = k$. It is worth noting that every realization of a finite PPP is a BPP with a specific number of realized points [34]. Accordingly, Ψ is a BPP if the number of points k included in any bounded subset W is a binomial random variable, and the numbers of points in disjoint sets are related via a multinomial distribution.

$$\mathbb{P}\{\Psi(W) = k\} = \binom{N}{k} \left(\frac{|\,W\,|}{|\,A\,|}\right)^{k} \left(1 - \frac{|\,W\,|}{|\,A\,|}\right)^{N-k}, \tag{1.10}$$

The binomial process is straightforward; all points are isolated. BPP is suitable when there is a predetermined number of nodes in a delimited area. For instance, it is suitable to be used to model the position of a group of UBSs in areas with a high clustering of users, where N

represents a given number of UBSs. A top view snapshot of UAV-assisted cellular network with BPP model is illustrated in Figure 1.8.

Chetlur and Dhillon [109] were the first to consider BPP for aerial networks. Some studies have suggested a predefined number of UBSs distributed within a finite area as BPP [46, 47, 110]. Nevertheless, we observe a lack of precise user clustering models in this studies.

Recently in [111], the authors modeled the spatial locations of the aerial users as a 3D BPP and evaluated the performance of a typical aerial user in a 3D UAV network using the truncated octahedron concept.

1.7.2 Random Shape Theory

Random shape theory is a branch of advanced geometry with the goal of modeling shapes in multiple dimensions and orientations. This theory allows for the organization of any arbitrary objects in space, which can be represented as a random object process (ROP) [112]. In this thesis, we focus on a straightforward class of object processes called "Boolean model".

1.7.2.1 Boolean Model

Also called Poisson germ–grain model or Boolean scheme, is a straightforward example of a random closed set and can be defined as a combination of sets that emerge from a PP. The Boolean model is based on a PPP Φ, where the points $\{X_i\}$ are called germs, and on an independent sequence of i.i.d. compact sets $\{K_i\}$, referred to as grains [87]. It is a useful tool for describing various objects, such as blockages. However, analyzing these objects can become more complex when correlations exist between them. The Boolean model can be expressed as follows

$$\Theta = \bigcup_i (X_i + K_i), \tag{1.11}$$

The Boolean scheme offers an advantage in assuming the independence of objects and their attributes, enabling a more straightforward evaluation of the model. It is commonly considered as the null hypothesis in stochastic geometry modeling. This model is marked by the following properties [113]

- The central points of objects in the 2D plane create a PPP. Thus, PPP simulation is crucial for enabling boolean scheme simulation.
- Objects are distributed independently, and their size, location and orientation are determined independently.

- The shape parameters (such as length, width, orientations and height), volume and location of any object are also independent.

Xiao [114] introduced the basic concepts of the Boolean scheme and described the analysis and simulation techniques used for this model.

In the context of communication networks, Bai *et al.* [113] developed a mathematical blockage model for mmWave terrestrial networks using the random shape theory as an alternative to the ray tracing approach covered in [115]. The Boolean scheme has also been adopted in [48, 49] to model the location of obstacles in UAV networks with a single tier.

1.8 Conclusion

In this chapter, we have presented the coverage concept and its associated methods that can be employed in cellular networks. These include heuristic methods and stochastic geometry-based methods. Additionally, the architecture of terrestrial HetNets and VHetNets is discussed, with particular emphasis on the advantages of aerial networks over terrestrial networks. The chapter also introduces UAV wireless communication in both academic and industrial contexts. Finally, the stochastic geometry tools are introduced. In particular, we have addressed the main mathematical properties and the useful theorems of the PPP, which is regarded as the standard and most commonly used PP due to its valuable mathematical characteristics. Additionally, we have also presented the BPP and PCP, which are powerful tools in our modeling process. The next chapter focuses on the use of stochastic geometry in channel modeling and performance metric measurement and introduces current methods for deriving coverage probability.

Chapter 2

Stochastic Geometry Modeling and Performance Metrics

Contents

2.1 Introduction **29**
2.2 Channel Propagation **29**
2.2.1 Channel Characterization 29
2.2.2 Propagation Effects 30
2.3 Cell Association Strategies **34**
2.4 Network Performance Measurement **36**
2.4.1 SINR 36
2.4.2 SINR Coverage Probability 38
2.4.3 SINR Outage Probability 39
2.4.4 Spectral Efficiency 39
2.5 Monte Carlo Simulations **40**
2.6 Conclusion **41**

2.1 Introduction

While capacity and data rates are undoubtedly important for 5G and beyond networks, it is equally crucial to ensure comprehensive network coverage. Coverage probability is an important factor that distinguishes network operators from one another as it directly affects the QoS experienced by users and has a significant impact on other system performance (Spectral efficiency, Energy efficiency, ...). The propagation channel has the greatest impact on the design of a wireless receiver among all impairments, which significantly impacts network coverage. Wireless propagation results in a loss of received signal power and the presence of multipath, which creates frequency selectivity in the channel. In this chapter, based on stochastic geometry models, we characterize propagation channel models for terrestrial and aerial networks. Additionally, we define various approaches to user association and present performance metrics, as well as simulation methods for calculating and evaluating these performances.

2.2 Channel Propagation

2.2.1 Channel Characterization

The design process of every wireless technology necessitates a comprehensive modeling of the propagation channel, as the characteristics of the latter significantly influence the network coverage. Air-to-ground (A2G) channel modeling of UAV-based networks has received considerably less attention compared to terrestrial networks, where ground-to-ground (G2G) channels have already been extensively studied and modeled.The A2G channel designates that UAVs communicate with ground users, while the G2G channel refers to the channel between the ground BS and ground users, as shown in figure 2.1. These two types of channels exhibit distinct characteristics. Specifically, the characteristics of A2G channels demonstrate a significant correlation with the elevation angles and altitudes of UAVs. For example, channels designated for LAP cannot be utilized for HAP due to differences in their channel diffusion environments. Moreover, the complexity of 3D environments and the multitude of parameters that needs to be considered continue to pose challenges for these channels. It is imperative to explore the specific characteristics of the propagation channel to promote the development of multiple antenna techniques such as MIMO [116].

Channel models for mmWave communications in aerial contexts are currently undergoing intensive research due to encountering various constraints. The flying capability of UAVs enables to achieve higher LoS probability compared to G2G links. However, due to the presence of

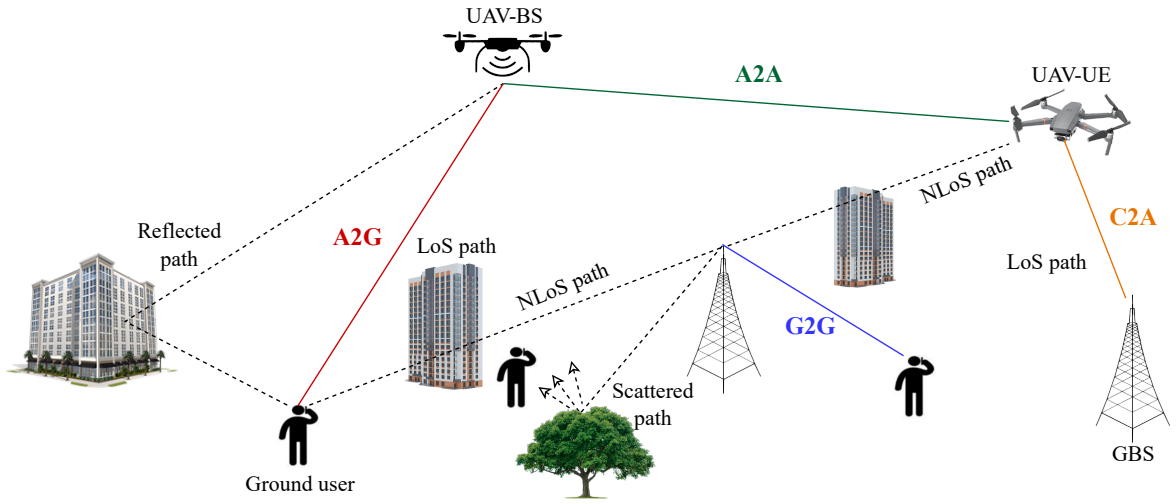

Figure 2.1: Illustration of Various Propagation Channels.

obstacles, the A2G link cannot frequently remain in LoS. To capture these characteristics, we mostly adopt probabilistic path loss model and fading model with different occurrence probabilities of LoS and NLoS.

In cellular-connected UAVs, the channel propagation between the GBS and an aerial user cannot be the same as the A2G channel which is intended for ground users at heights of 1.5 meters. Therefore, new channel model was developed for aerial users is called cellular-to air (C2A) channel (see figure 2.1). In addition, there exists the A2A channel, denoting the communication link between two aerial platforms without direct connectivity to ground infrastructure as in UAV relay communication. In this thesis, we focus on the A2G and G2G channels.

Several propagation models exist in the literature. Accurate A2G channel models regarding the considered environment have been analyzed in [65, 70, 71, 116], to conceive and evaluate UAV communication links, especially for emerging UAV applications requiring high-speed data transfer.

2.2.2 Propagation Effects

In all the above-mentioned channel models, the propagated signals experience effects such as path loss, shadowing, and small-scale fading, which are outlined as follows.

2.2.2.1 Path loss

Path loss refers to the attenuation of average signal power due to long signal propagation distances and environmental parameters. Path loss is a fundamental element in the design and analysis of a telecommunication network. The research reported in [117] found that in A2G

scenarios and urban environments, a small elevation angle can meaningfully alter path loss independently of the distance, i.e. increasing the elevation angle will result in reduced path loss at the same propagation distance [118]. In the majority of models, this phenomenon is represented by an exponential decay function with distance, as shown in Figure 2.2.

2.2.2.2 Shadowing

Large obstacles relative to wavelength such as buildings, vehicles, and trees can cause signal attenuation through diffraction and reflection, resulting in path obstruction. This phenomenon is commonly referred to as shadowing and can also originate from the UAV itself while flying. Shadowing is highly correlated at a larger time and space scale compared to small-scale fading. This means that several signals can be blocked by the same object, resulting in greater signal loss than expected. Communication path obstacles in urban environments can cause geographically correlated shadowing on a scale ranging from 50 to 200 meters [90]. For a tractable analysis, researchers generally neglect the correlation between obstacles [113]. In reality, as the transmit-receive distance increases, the intensity of shadowing is expected to increase, especially in mmWave communications, where signals are more susceptible to blockages and experience high attenuation. However, the distance dependency of blockage effects is not accounted for in shadowing models that use random variables. In this thesis, we propose more sophisticated models of the wireless propagation channel, to capture 3D blockage modeling as Boolean scheme.
The log-normal distribution is a common model for the shadowing effect, which is given by

$$f_S(w) = \frac{1}{w\sqrt{2\pi\sigma_S^2}} \exp\left(-\frac{(\ln w - \mu)^2}{2\sigma_S^2}\right), \tag{2.1}$$

where $\mu(dB)$, σ_S are the mean and the variance of $w(dB)$.
Shadow fading lasts tens of seconds or minutes, longer than multipath fading, which lasts a few milliseconds.

2.2.2.3 Small-scale Fading

The small-scale fading phenomenon, commonly referred to as fast fading, results from the combination of multiple replicas of the same signal, each exhibiting slight variations in delays and phase shifts. Furthermore, it models the communication link, which undergoes rapid fluctuations due to node mobility or the existence of nearby diffusers. In multipath propagation, fading amplitude statistics play a crucial role in analyzing small-scale variations. First-order

statistics, including cumulative distribution function (CDF) and PDF, assist in understanding the random behavior of fading channels. Due to small-scale fading, the signal power variation may reach up to 40 dB over only a fraction of a wavelength. In the UAV channel, multipath fading may originate from the UAV itself. Although these reflections are generally weak and have a low delay [119].

In what follows, we'll look at several frequently used models for small-scale fading distributions.

Rician Fading

Rician distribution is used when there is a single, distinguished component in the communication link, commonly approximates the variation in the fading channel with LoS. The Rician K-factor quantifies the extent of multipath fading in a quantitative way. The literature [120] indicates that in UAV communication, as the altitude of a UAV increases, the effect of ground-reflected multipath fading decreases. To characterize the Rician fading channel, two metrics are required: the Rician factor and the average signal power. Consequently, this model is more complex and challenging to apply. Additionally, the lack of a closed-form formula for the PDF and CDF of the signal strength complicates modeling and mathematical analysis. The Rician fading model is most applicable to environments where the LoS component is important and can be discerned, such as rural or wide-open areas. The PDF of the Rician fading gain is given as follows [121]

$$f_H(g) = \frac{g(k+1)}{\mu} \exp\left(-k - \frac{g(k+1)}{\mu}\right) I_0\left(2\sqrt{\frac{g(k+1)k}{\mu}}\right), \tag{2.2}$$

Rayleigh Fading

Rayleigh fading is particularly suited to scenarios where there is no dominant path among the various multipath components in the link, which is typically the case in NLoS communications, such as in urban or indoor areas. One of the principal benefits of the Rayleigh fading model is its simplicity and ease of use, it necessitates only the average signal power to characterize the fading channel. Research [122, 123] has indicated that Rayleigh fading is unsuitable for mmWave networks due to their poor scattering properties. The signal strength is distributed according to a Rayleigh distribution with scale parameter σ, exhibiting a high probability of being near zero and varying from very low to very high values. The complementary cumulative distribution function (CCDF) and PDF of the channel power gain are closed-form expressions,

respectively given by

$$\bar{F}_H(g) = \exp\left(-\frac{g^2}{2\sigma^2}\right), \tag{2.3}$$

$$f_H(g) = \frac{g}{\sigma^2}\exp\left(-\frac{g^2}{2\sigma^2}\right), \tag{2.4}$$

Nakagami-*m* Fading

The Nakagami-*m* fading is a crucial factor in modeling land-mobile and indoor-mobile multipath propagation used to accurately reproduce the channel behavior. It can simulate multiple scenarios, allowing us to control the severity of multipath fading and maintain analytical tractability [109]. The Nakagami-*m* distribution is a more general representation of multipath distributions than the Rayleigh, Rice, and Gaussian distributions. It provides greater flexibility and accuracy in matching experimental data than other distributions.

In fact, Rayleigh, Recian and Gaussian distributions are special cases of Nakagami-*m* fading environments. This can be achieved by an appropriate choice of the shape parameter m. For example, when $m = 0.5$ we find Gaussian distribution, for $m = 1$ the model converge to Rayleigh distribution, for $m = \frac{(1+k)^2}{1+2k}$ we obtain the Rician distribution, and finally when $m \to \infty$ the model converges to the no-fading environments which are defined by a system with no small-scale fading.

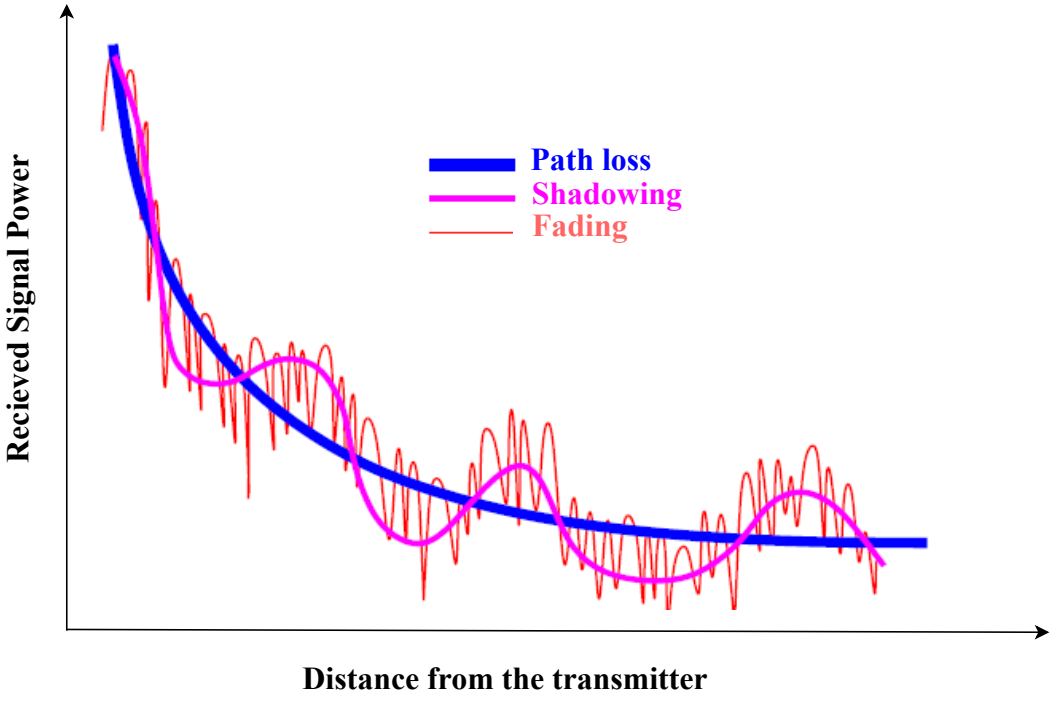

Figure 2.2: Effects of Path loss, Shadowing, and Fading [124].

The Nakagami-*m* channel fading gain follows a gamma distribution, and its CCDF and PDF are respectively given by [125]

$$\bar{F}_H(g) = \sum_{q=1}^{m-1} \frac{(mx)^q}{q!} e^{-mg}, \tag{2.5}$$

$$f_H(g) = \frac{m^m g^{m-1}}{\Gamma(m)} \exp(-mg), \tag{2.6}$$

Nakagami-*m* fading is widely used in the open literature. Previous research [14, 96, 126, 127] has adopted the Nakagami-*m* fading channel for small-scale fading to capture the features of the mmWave communications in UAV Networks and terrestrial networks. Chetlur and Dhillon [109] have investigated the performance of "no-fading" environments in a finite 3D UAV network applying the asymptotic expansion of incomplete gamma function.

Figure 2.2 shows the combined effects of large-scale propagation and small-scale propagation by plotting three distinct realizations of the received signal power. It indicates that the attenuation of radio signals can be explained by the combination of path loss, shadowing, and multipath effects as a function of distance from the source [124]. Signal strength variations caused by multipath occur within the signal wavelength range, while log-normal shadowing affects the total loss.

2.3 Cell Association Strategies

The user association process has to cope with the growing heterogeneity of cellular networks. In VHetNets, the coverage of each network entity depends on its type, (a Ground or an Aerial BS), and the network geometry, which refers to its location in relation to other network entities. Identifying the BS that the user is associated with is crucial for evaluating their performance. Two main approaches have been proposed for cell association in the literature, as shown in Figure 2.3.

- **The Nearest BS Association Rule**

It is a commonly used approach due to its mathematical tractability. This rule selects the BS with the shortest distance, which corresponds to the lowest path loss. Which can be formulated as

$$\text{Serving BS} = \arg\min\{d_j^{-\alpha}\}, \tag{2.7}$$

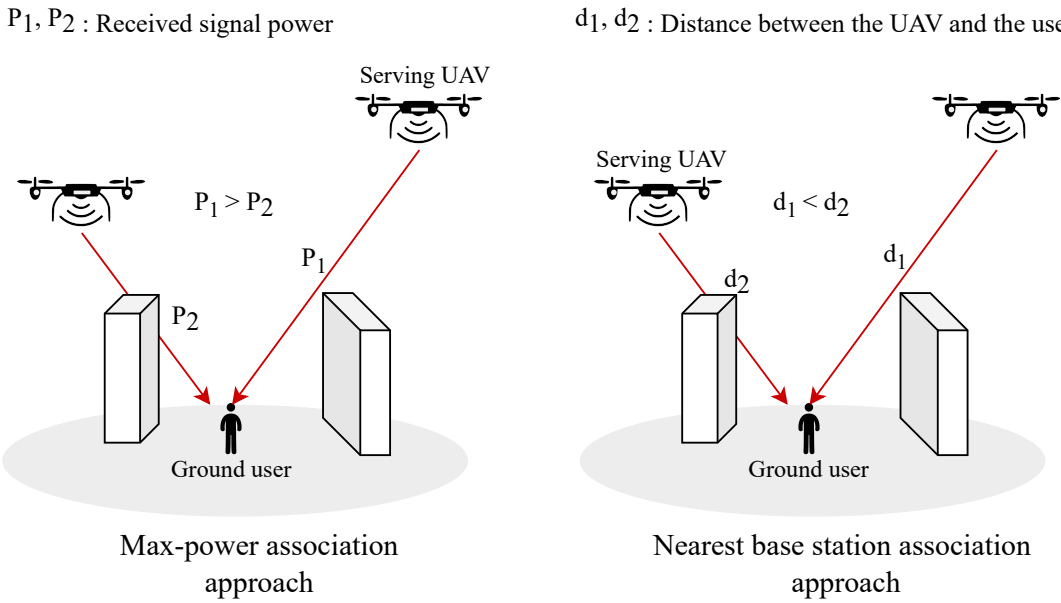

Figure 2.3: Cell association rules.

where d_j is the distance between the BS j and the user.

- **The Max-Power Association Policy**

This approach is based on the strongest received signal power. The process of assigning users to the access network is based on measuring the power received by each of the BSs adjacent to the user. This measurement is used to select the station to which the user should be assigned to ensure good service continuity. The strongest received signal power is reflected in the minimum values of both path loss and small-scale fading across all BSs.

$$\text{Serving BS} = \arg\max\{P_j\}, \tag{2.8}$$

where P_j is the received power at the user from the BS j.

It is worth noting that, the received signal power may be affected by the LoS/NLoS parameters. In practice, a user may connect to a BS with LoS transmission even if it is farther away than a closer BS that is blocked. Therefore, it is important to separately consider the occurrence of LoS and NLoS transmissions and analyze the association probabilities of LoS/NLoS BSs. It can be concluded that the second approach may be more practical.

2.4 Network Performance Measurement

Several methods exist in the literature to accurately measure and assess wireless network coverage as part of network performance evaluation. Most performance measures in stochastic geometry models in various scenarios depend on the node locations and rely on signal-to-noise ratio (SNR), signal-to-interference ratio (SIR) or SINR at the receiver level, and are also based on the random variable statistics. Coverage probability is the basis for several performance metrics, such as average throughput, spectral efficiency and energy efficiency and is therefore recognized as a key system-level metric. The coverage probability can be defined as the probability that a user in a specific area can establish and maintain a connection with the network at a given signal strength or quality level. Outage probability is another commonly used method for evaluating coverage.

2.4.1 SINR

The SINR enables the measurement of link quality. It refers to the ratio of the power of the desired signal received by the user to the power of the interference and noise signals received by the user. Downlink interferences are typically defined as the sum of signal powers from BSs that are not currently serving the user. In particular, if a BS increases its transmission power, it will cause an increase in interference for all other communicating users. When users are randomly distributed in space, the received signal power becomes random, and the interference power is determined by various stochastic processes, such as the random spatial distribution of nodes, shadowing, and fading. The impact of interference and noise on the overall quality of the signal should be carefully considered, and mitigating their effects is a common goal in many fields. Therefore, it is crucial to characterize the stochastic geometry of the network as it is the primary determinant of the SINR. Mathematically, the SINR at the receiver located at the origin in 2D or 3D Euclidean space can be expressed as

$$SINR = \frac{P_r}{I + N_0}, \tag{2.9}$$

where P_r is the received power and I and N_0 are the aggregate interference and the additive white Gaussian noise signal power, respectively.

The SNR metric is used to measure the ratio of signal to noise when interference is eliminated or not considered, and the SIR metric is used when the thermal noise is negligible as compared to the received interference. The SNR can vary significantly among different users in a wireless

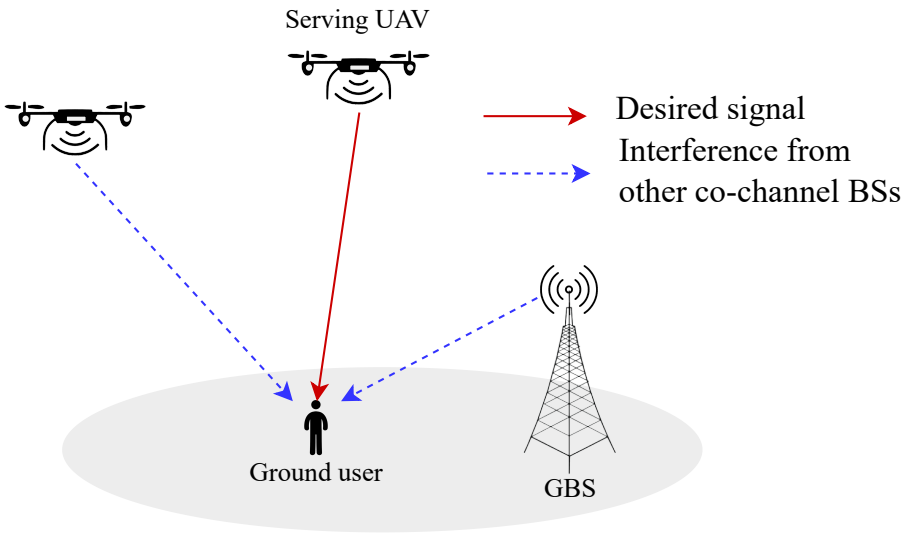

Figure 2.4: Intercell interference.

system due to differences in path loss, shadowing caused by obstructions, and fading due to constructive or destructive wave interference. It is crucial to note that these variations can range from ten to hundreds of decibels.

2.4.1.1 Inter-cell interference

Inter-cell interference (ICI) is a challenge that is commonly encountered in traditional cellular networks where multiple cells operate nearby. ICI occurs when multiple base stations (BSs) share the same frequency band, and their coverage areas overlap, leading to interference in the overlapping regions, as illustrated in Figure 2.4. The matter can become even more crucial in ultra-dense small cell networks, and D2D communications, potentially resulting in a reduction of service quality for users and limiting performance improvements. To reduce interference, one solution is to allocate additional resources. However, this may decrease spectral efficiency and increase operating costs. On the one hand, the use of aerial BSs can reduce interference. By deploying a predefined number of UAVs, we can control the number of links needed to communicate with ground users. Several advanced antenna technologies have been proposed to address ICI, including directional beamforming and 3D beamforming technologies. Combined with UAV technology, these technologies deliver even better performance.

The main performance metrics that can be derived using the SINR to evaluate a stochastic geometry-based model are presented in Figure 2.5, where Th refer to the SINR threshold. In this thesis, we focus on evaluating the SINR coverage probability and spectral efficiency based on association probability.

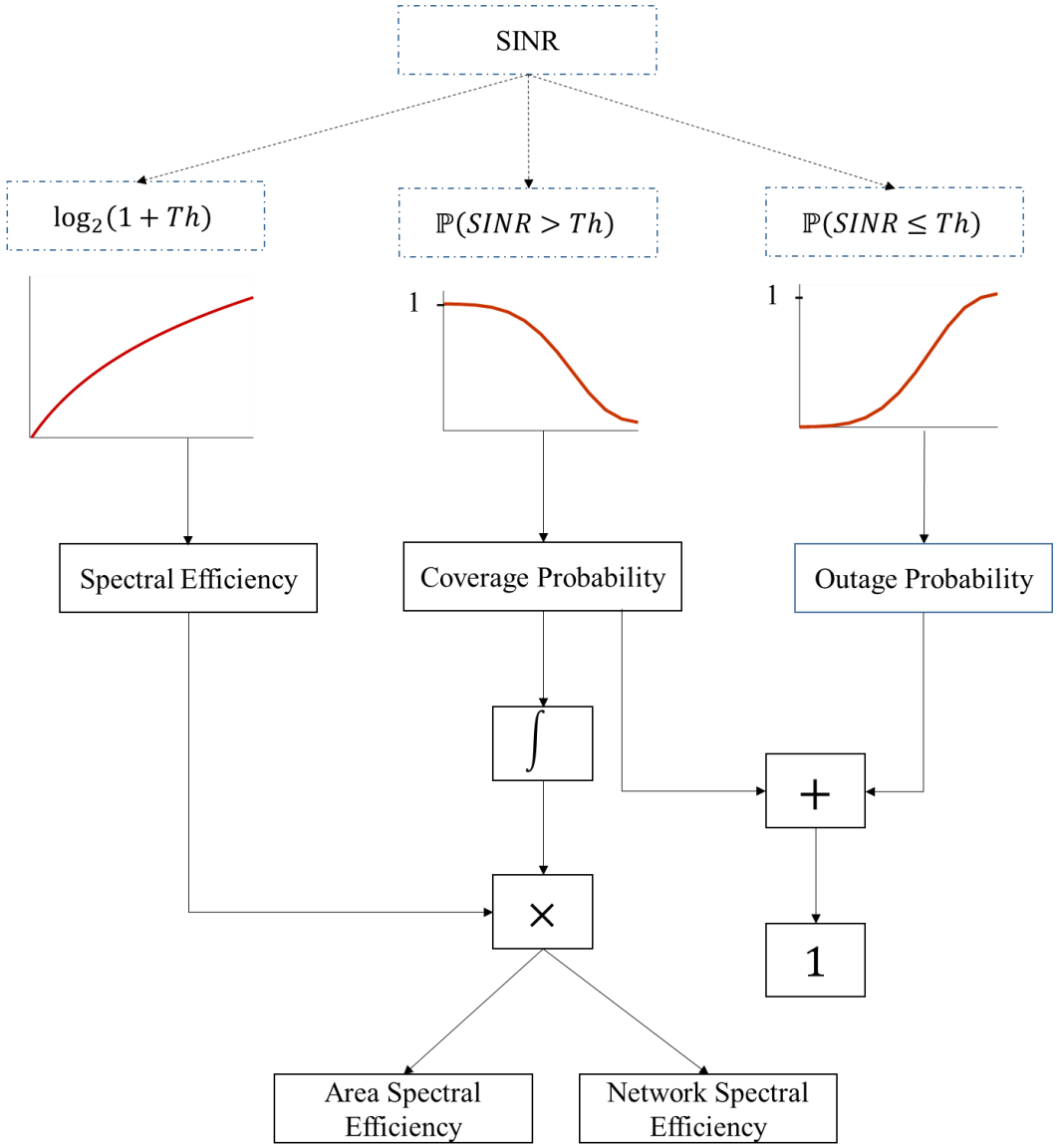

Figure 2.5: Key performance measures based on the SINR, employed in the abstraction of stochastic geometry.

2.4.2 SINR Coverage Probability

The SINR coverage probability is the probability that the received SINR at the user is greater than a predefined SINR threshold $\mathcal{T}$.

$$P_c(\mathcal{T}) = \mathbb{P}(SINR > \mathcal{T}), \tag{2.10}$$

The coverage probability is the probability that the typical user can successfully decode the incoming signal transmitted at a specified rate $\mathcal{R} = B\log_2(1+\mathcal{T}))$ over a bandwidth B.

2.4.3 SINR Outage Probability

The outage probability is defined as the probability that the SINR performance metric will drop below a predefined SINR threshold.

$$O_c(\mathcal{T}) = \mathbb{P}(SINR \leq \mathcal{T}) = 1 - \mathbb{P}(SINR > \mathcal{T}) = 1 - P_c(\mathcal{T}), \tag{2.11}$$

Therefore,

$$P_c(\mathcal{T}) = 1 - O_c(\mathcal{T}), \tag{2.12}$$

It's important to highlight that the outage probability and the coverage probability are equivalent to the CDF and the CCDF of the SINR at the typical user.

2.4.4 Spectral Efficiency

The spectral efficiency (SE), spectrum efficiency, or bandwidth efficiency is a crucial factor in measuring the frequency band. It is defined as the data rate that can be communicated over a normalized bandwidth to optimize the use of the spectrum. The modulation order could potentially be increased to enhance it. Moreover, channel capacity can be increased by increasing the SE of a system. MIMO, beamforming, power control, and multi-carrier modulation (MCM) are techniques commonly used to enhance spectral efficiency. The expression for measuring SE in bits/s/Hz is as follows.

$$SE = \frac{\mathcal{R}}{B} = \log_2(1 + \mathcal{T}), \qquad bits/s/Hz, \tag{2.13}$$

In this study, we focus on two types of spectral efficiency: Area Spectral Efficiency (ASE) and Network Spectral Efficiency (NSE).

2.4.4.1 Area Spectral Efficiency

The initial evaluation of the ASE was in [128]. This metric can be defined as the average number of bits transmitted per unit time per unit bandwidth per unit finite area (bit/s/Hz/m^2) [109]. To compute the ASE, it is crucial to determine the number of simultaneously active links per unit area. The general expression of the ASE can be formulated as

$$ASE = \frac{1}{|\mathcal{A}|} \sum_{n=1}^{NU} \mathbb{E}\left[SE\right], \qquad bits/s/Hz, \tag{2.14}$$

where NU is the number of active users within the target area $|\mathcal{A}|$. The mathematical expectation is averaged among several fading realizations.

Using the concept of stochastic geometry, (2.14) can be written as [129]

$$ASE = \lambda \, SE \, \mathbb{P}\left(SINR > \mathcal{T}\right), \qquad bits/s/Hz/m^2, \tag{2.15}$$

where λ is the density of active BSs.

2.4.4.2 Network Spectral Efficiency

The NSE is typically evaluated for a finite network with a fixed number of transmitting nodes (as UAVs), it can be defined as the total number of bits transmitted per unit time over a given bandwidth across the entire network. The general expression of NSE can be written as

$$NSE = \mathcal{N} \, SE \, \mathbb{P}\left(SINR > \mathcal{T}\right), \qquad bits/s/Hz, \tag{2.16}$$

where $\mathcal{N}$ is the number of maximum active links in the network.

2.5 Monte Carlo Simulations

Monte Carlo simulations, named after the Monte Carlo Casino in Monaco due to the randomness inherent in gambling games, are frequently used to gain insight into network performance without making restrictive assumptions and can provide an estimation of the complete network statistics (resolve a statistical issue).

The Monte Carlo method is a stochastic method involves running a large number of random iterations to obtain numerical results to estimate for example the coverage probability, outage probability, and spectral efficiency based on stochastic geometry tools. Firstly, each variable with intrinsic uncertainty is represented by a probability distribution. Subsequently, the findings are recalculated on each iteration, with a new set of random numbers drawn from within the expected range. As the number of inputs increases, the outputs become more accurate. To put it another way, the various results create a bell curve or normal distribution, with the most frequent result falling somewhere in the middle of the curve.

Monte Carlo simulations are provided to verify the correctness of the mathematical framework. However, carrying out this task can be very time-consuming or require considerable computing resources. Developing tractable analytical methods based on stochastic geometry enables a straightforward analysis and evaluation of the network performance. To confirm the validity of the analytical investigation, it is crucial that the analytical results precisely match the Monte Carlo simulations.

The Monte Carlo methodology for estimating coverage probability with stochastic geometry can be summarized by the following steps

1. Define the area of interest, e.g., circular area of radius R.
2. Generate the spatial distribution of the nodes e.g., PPP, BPP, PCP.
3. Generate the parameters related to the coverage model.
4. Computig the coverage probability based on the SINR.
5. Repeat steps 2 to 4 for a large number of iterations.
6. Estimate the coverage probability by computing the ratio between the result of all iterations and the total number of iterations.

2.6 Conclusion

In this chapter, we have presented the channel propagation models (A2G and G2G channels). We have shown that wireless mmWave propagation, specifically, is susceptible to path loss, shadowing, and multipath fading. These factors have a significant impact on the received signal power and SINR, which in turn affect the cell association and network performance. On the other hand, we have provided the key performance metrics and highlighted the advantages of using Monte Carlo simulations to validate them. In the following chapters, 3 and 4, we provide a comprehensive description of our two contributions and present the two new proposed UAV-assisted cellular network models with different scenarios and environmental contexts.

Chapter 3

Single-Tier Networks: UBS Swarms Modeling

Contents

3.1 Introduction **43**
3.2 UBS Deployment in Isolated Regions **43**
3.3 Beamforming Technology in Aerial Networks **44**
3.3.1 Directional Beamforming 44
3.3.2 3D Beamforming 44
3.4 UBS Swarm **45**
3.5 System and Channel Modeling **46**
3.5.1 UAV Network Model and Assumptions 46
3.5.2 Air-To-Ground Channel Model 48
3.5.3 Vertical Antenna Pattern Gain 49
3.5.4 User Association and SINR Model 49
3.6 Probability Density Function **51**
3.6.1 Conditional Serving Distance Distribution 52
3.6.2 Conditional Interfering Distance Distribution 53
3.7 Conclusion **53**

3.1 Introduction

Providing reliable coverage in remote and isolated regions represents a complex challenge in 5G cellular networks, that must be addressed. One logical approach to increasing transmission bands and capacity and providing Gigabit wireless services in uncovered regions is to combine mmWaves with UAV communications. These systems use narrow beams to provide highly direct communication. However, network coverage can be affected by several factors, including the terrain, weather conditions, and the presence of obstacles. With the development of beamforming technology, the integration of UBSs with 3D beamforming has become a promising method for enhancing coverage performance. Nevertheless, UAV communications are still in the early stages of development, and there are several significant issues that remain open and require thorough investigation.

In this chapter, we propose a 3D single-tier model of mmWave enabled UBS swarm networks that use the developed 3D beamforming technology technique to enhance signal quality and mitigate interference. The model is implemented in a limited isolated area to provide coverage to users not currently served by traditional terrestrial networks. In this context, we present the system model and define the user association approach and the SINR model that have been adopted. Finally, we derive the expressions of the probability density function of the distances from the typical user to the served and the interfering UBS.

3.2 UBS Deployment in Isolated Regions

The integration of UBSs into cellular networks has been studied for numerous communication scenarios. Nevertheless, there remain certain scenarios that have not yet been addressed or studied in sufficient depth. When aiming for universal coverage, it is important to consider reaching remote areas, or geographically challenging areas characterized by shadow zones, also known as isolated regions particularly with 5G mmWave wireless communications. In this case, the necessity to cover vast distances may present a significant challenge to traditional BSs, and wireless communication links remain difficult to establish. The US Federal Communications Commission recommends several frequency spectrums within the mmWave for 5G networks. These include the local multi-point distribution service (LMDS) band ranging from 28 to 30 GHz, the unlicensed 60 GHz band, and the 12.9 GHz band located from 71–76 GHz, 81–86 GHz, and 92–95 GHz in the E-band [130, 131]. However, mmWaves have smaller coverage areas compared to frequencies below 6 GHz [11]. The deployment of mmWave aerial networks

represents a potential solution to the spectrum crunch crisis and can offer the prospect of multi-gigabit communication services, thereby overcoming the limitations of traditional infrastructure and extending connectivity to remote or inaccessible areas.

Few studies have analyzed coverage in isolated regions using stochastic geometry approach. Wang *et al.* [132] considered a single UBS centered on a circular, isolated region. However, this scenario is not realistic as a single UBS cannot ensure seamless coverage due to its limited charge and battery life.

3.3 Beamforming Technology in Aerial Networks

The use of mmWave technology supports the functionality of beamforming techniques. The integration of UBSs with innovative beamforming techniques for downlink channels can effectively mitigate the intensified shadow effects and elevated propagation losses observed in mmWave bands, thereby reduces the network's vulnerability to interference. Notably, boosting spatial beamforming gain is an effective strategy for increasing the capacity and coverage of wireless networks. In this thesis, we focus on two types of beamforming directional beamforming and 3D beamforming.

3.3.1 Directional Beamforming

Directional beamforming, also known as 2D beamforming, is a crucial technique for mmWave communications. Generally, the elements used in beamforming systems are arranged at half-wavelength intervals to preserve directional control and avoid unwanted secondary grating lobes. This technique is designed to direct the beam dynamically in a specific direction within the horizontal plane without the need to physically move the antennas. Ground and aerial BSs can use antenna arrays with a fixed geometry to direct transmitted signals towards mobile users, thereby alleviating the received interference signals' power. However, 2D beamforming neglects the array's gain in the vertical plane.
The subject of directional beamforming has been discussed in numerous existing works in the scientific literature. Cherif *et al.* [47] and Pengshan *et al.* [133] have incorporated the directional antenna array at the aerial BSs with a sectored antenna model.

3.3.2 3D Beamforming

The use of 3D beamforming enables the creation of distinct beams in a 3D spatial domain simultaneously by adjusting the antenna's radiation pattern in the horizontal and vertical

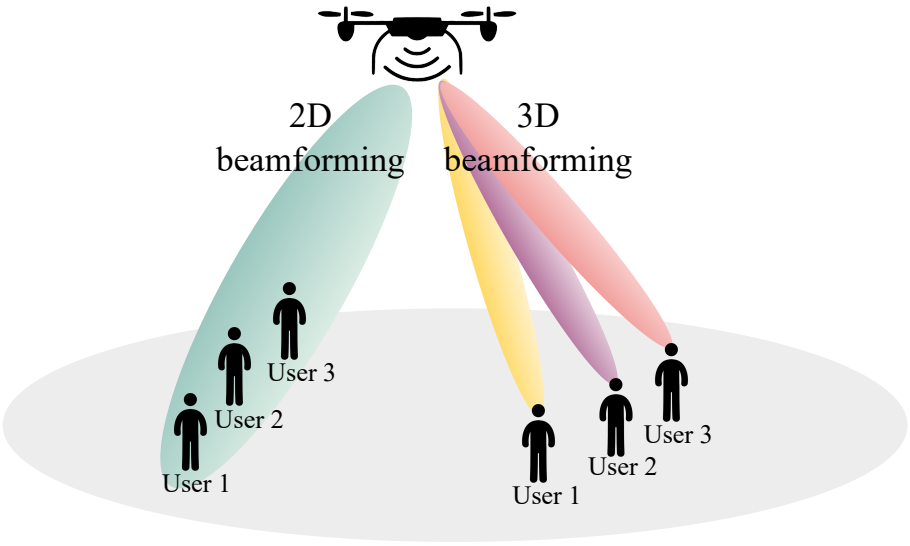

Figure 3.1: Illustration of 2D beamforming and 3D beamforming [64].

planes [134], resulting in a significant concentration of beamforming gain in the target area. This is achieved through extensive sky access, resulting in more precise and efficient signal transmission with reduced ICI. This enables accommodating a greater number of users and ensuring improved coverage performance. 3D beamforming plays an important role in 3D network models such as aerial networks or NTNs (e.g. satellite communications) where 3D coverage is essential. The mobility and flexibility of UAVs in addition to the conditions of the LoS channel in A2G communications permit the practical implementation of 3D beamforming due to the effective mechanical beam steering in any 3D direction. Figure 3.1 displays the main differences between 2D and 3D beam steering.

The results of the analysis carried out in [134] show that incorporating 3D beamforming into fixed-height GBSs maximizes coverage. However, the incorporation of this technology into UAV networks [135] is not fully analyzed in the literature. Therefore, expanding this to UBSs that can easily modify their tilt angle and altitude would be beneficial. However, implementing 3D beamforming at UBSs still poses challenges, especially in controlling the required number of simultaneously active links to effectively reduce interference and ensure wide coverage.

3.4 UBS Swarm

The UBSs are often deployed regionally rather than in a large-scale manner. The current study aims to employ a predefined number of UBSs in a finite region. In fact, reliance on a single UBS cannot ensure consistent service or guarantee continuous coverage in finite areas, as it is inherently limited in terms of both load and battery life. Specifically, when considering

blockage effects, they can worsen the irregularity of network topology and cause fluctuations in users' rates. Consequently, deploying a swarm of UBSs in a finite region is more efficient. The number of UBSs in a swarm can be modified to meet the needs of a specific task and should be selected thoughtfully to minimize interference. In a realistic scenario, a mobile operator would deploy UBSs one by one until a satisfactory coverage is achieved in the target area to be assisted. Since the deployment of a given UBS can be modeled using the Bernoulli distribution, we can see that the deployment of a finite number of UBSs is then naturally modeled using the binomial distribution. Therefore, the BPP is a suitable stochastic geometry tool for modeling the location of a UBS swarm when covering a limited area.

UBS swarms can potentially enhance system robustness by offering redundancy. This implies that in the event of UBS failure or compromise, the entire swarm can still function effectively. Furthermore, interference can be considerably reduced by rolling out a predefined number of UBSs, thus controlling the required number of links to communicate with ground users.

3.5 System and Channel Modeling

3.5.1 UAV Network Model and Assumptions

We investigate an isolated region where conventional GBSs are unable to establish wireless connectivity [136]. Our proposal involves deploying a swarm of N transmitting UBSs that operate in mmWave bands to provide 3D downlink coverage. The isolated region is represented as a finite disk, $B_r(O, r_a)$, centered at the origin O with a radius of r_a, and will be referred to as the "target area". We assume that all UBSs transmit with equal powers, denoted by P_U and use the 3D beamforming technique. The time is assumed to be stationary.

Let $\Phi_U = \{A_i,\ i \in 1 : N\}$ be the set of 3D UBS point locations; $\{A_i\}$ are assumed to be independent and identically distributed (i.i.d.) in a finite disk $B_a(O, r_a)$ according to BPP. The use of this disk assumption in modeling finite networks is a common approach in the literature [42, 46, 109] due to its expositional simplicity. For theoretical tractability, the UBSs are regarded as stationary LAP [137], that hover at the same altitude h above the ground, from which the center of the circular disk is $O' = (0, 0, h)$, as illustrated in Figure 3.2.

However, even though there may be slight differences in altitude among the UBSs, this variation can significantly complicate the derivation process. Nevertheless, the same level of performance can be achieved using the same deterministic UBS altitude scenario, as demonstrated in [109]. Therefore, we exclude the variation in UBS altitudes in our analytical derivation and discuss its

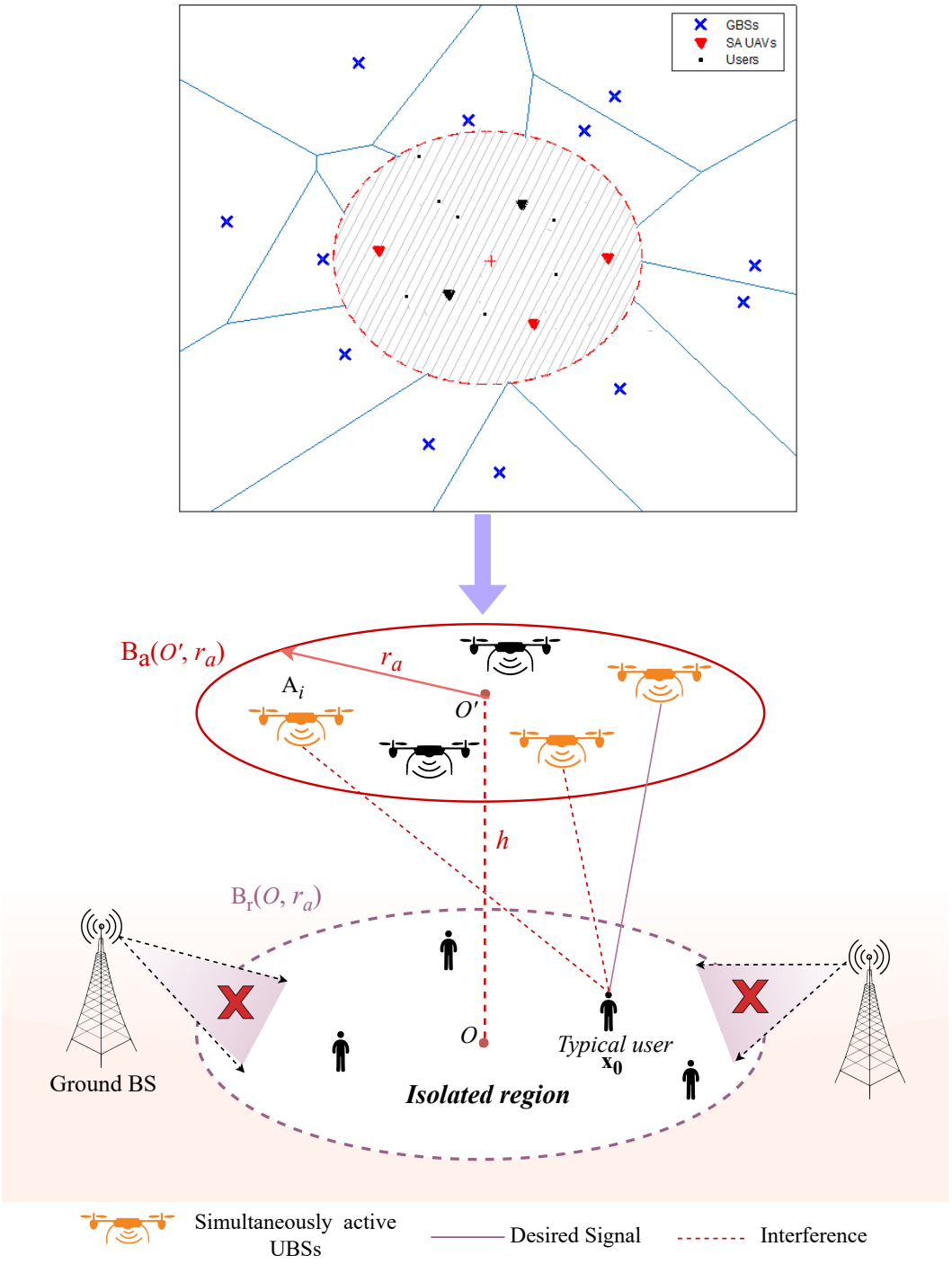

Figure 3.2: Single UBS swarm deployed in B_a to cover random users within a finite isolated area B_r. B_a and B_r are parallel concentric disks with the same radius r_a.

impact in Chapter 5.

To evaluate the network spectral efficiency, we assume that K out of N UBSs with location denoted by $\Phi_K \subset \Phi_U$ are simultaneously active (SA) and reusing the same resource block. The users are randomly distributed in B_r. We perform our analysis on a typical user u located at $\mathbf{x}_0 \equiv (y_0, 0, 0)$ in the disk B_r, who is assumed to be at a distance y_0 from the origin O.

3.5.2 Air-To-Ground Channel Model

Al-Hourani *et al.* [70] developed a common approach to consider the features of UBSs that can maintain LoS communication with the ground user, resulting in lower propagation attenuation compared to NLoS links. This widely used A2G approach identifies the link type based on the probability of its occurrence related to the elevation angle. However, it does not consider blockage characteristics, such as the size and height of the building. Therefore, it may be suitable for an isolated region, but it may not be appropriate for a densely populated urban area. In section 4.5, we develop a new A2G channel that takes into account the characteristics of blockages.

In this work, the A2G channel displays both large-scale fading and small-scale fading.

Large-scale path loss

Considering probabilistic LoS and NLoS transmissions, the path loss model is presented as follows

$$\Upsilon_U^l(X_i) = \begin{cases} \varphi_{LoS} {X_i}^{\alpha_U^{LoS}} \quad w.p. \quad P_U^{LoS}(X_i), \\ \\ \varphi_{NLoS} {X_i}^{\alpha_U^{NLoS}} \quad w.p. \quad P_U^{NLoS}(X_i), \end{cases} \tag{3.1}$$

where $X_i = \sqrt{Y_i^2 + h^2}$ is the distance between the typical user u and the UBS located at A_i, h is the UBS altitude, Y_i is the distance between u and the projection of UBS A_i on the plane. φ_{LoS} and φ_{NLoS} are the additional path loss for LoS and NLoS links, respectively, with $\varphi_{NLoS} > \varphi_{LoS}$, α_{LoS} and α_{NLoS} are the path loss exponent for LoS and NLoS links, respectively.
$P_U^{LoS}(X_i)$ and $P_U^{NLoS}(X_i)$ denote the probability that a link is in LoS or NLoS state, respectively given by [70]

$$P_U^{LoS}(X_i) = \left[1 + c_1 \exp\left(-c_2 \left(\frac{180}{\pi} \sin^{-1}\left(\frac{h}{X_i}\right) - c_1\right)\right)\right]^{-1}, \tag{3.2}$$

$$P_U^{NLoS}(X_i) = 1 - P_U^{LoS}(X_i), \tag{3.3}$$

Note that the LoS/NLoS probabilities depend on the environmental constant c_1 and c_2 and the elevation angle $\sin^{-1}\left(\frac{h}{Y_i}\right)$. The elevation angle is the angle from the user u at x_0 to an arbitrary UBS A_i.
This model supports the notion that transmission links are less likely to be obstructed by obstacles as the elevation angle increases.

Small-scale fading

With the assumption of probabilistic LoS/NLoS propagation, the Nakagami-*m* fading model is the most suitable due to its ability to control the severity of multipath fading and simulate various scenarios while maintaining analytical tractability. We assume that each link is affected by Nakagami-*m* fading, such that the channel power fading is a normalized gamma random variable $\Gamma(m_U^{LoS}, \frac{1}{m_U^{LoS}})$, $\Gamma(m_U^{NLoS}, \frac{1}{m_U^{NLoS}})$ where m_U^{LoS} and m_U^{NLoS} are distinct fading parameters, for LoS and NLoS links, respectively. The CCDF of the channel power fading, denoted by h_U^l, can be expressed as

$$\bar{F}_{h_U^l}(\eth) = \sum_{g=1}^{m_U^l - 1} \frac{(m_U^l \eth)^x}{x!} e^{-m_U^l \eth}, \tag{3.4}$$

where $l \in \{LoS, NLoS\}$.

3.5.3 Vertical Antenna Pattern Gain

The vertical antenna pattern gain of UBS A_i is denoted by $\Omega(\omega, \theta(X_i))$,which can be expressed as follows [134]

$$\Omega(\omega, \theta(X_i)) = 10^{-0.1 \times \min\left[12\left(\frac{\omega - \theta(X_i)}{\theta_d}\right)^2, SLL\right]}, \tag{3.5}$$

where ω is the down tilt angle of the UBS antenna pattern A_i and $\theta(X_i)$ is the vertical user's angle of arrival given by $\theta(X_i) = \tan^{-1} \frac{h}{\sqrt{(X_i^2 - h^2)}}$, as illustrated in Figure 3.3. θ_d and SLL are the half-power beamwidth and the side lobe level of the vertical antenna pattern, respectively. We assumed that the tilt angle remains constant for all transmitting UBSs.

3.5.4 User Association and SINR Model

The cell association strategy employed in this study takes into account both LoS and NLoS propagation by selecting the strongest received signal power. It is worth noting that the events of the UBS being in either LoS or NLoS links are mutually exclusive. This is due to the UBS swarm being designed to follow a BPP distribution. The location of the serving UBS is indicated by A_0 where $A_0 \subset \Phi_K$.

According to [138], it could be assumed that the Nakagami-*m* fading gain expectation is one, $\mathbb{E}(h_U^{LoS}) = \mathbb{E}(h_U^{NLoS}) = 1$. The received signal power at a typical user from UBS A_i can be calculated as

$$\xi_U = P_U \varphi_l^{-1} {X_i}^{-\alpha_U^l}, \tag{3.6}$$

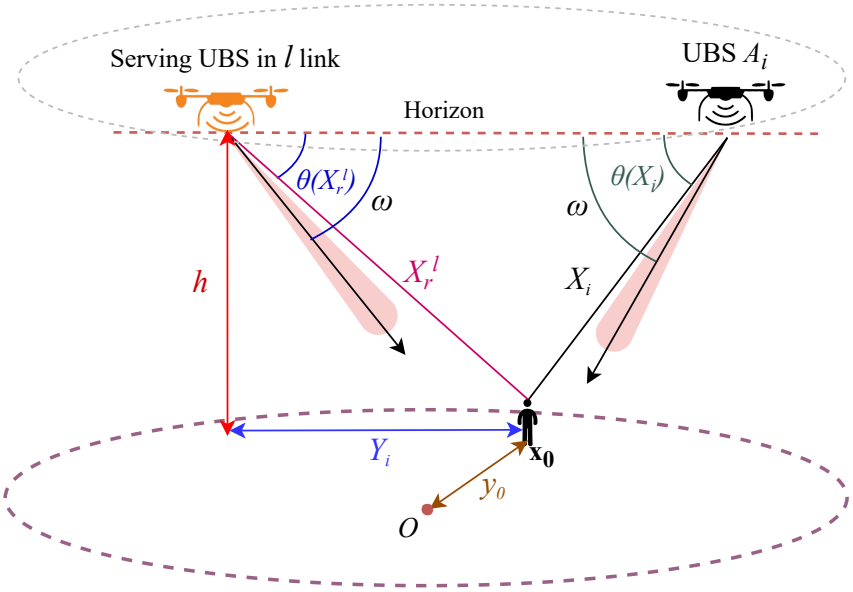

Figure 3.3: Illustration of the system and the 3D beamforming parameters. The down tilt angle ω is identical for all UBSs' antenna pattern. A_i represents the location of an arbitrary UBS and A_0 represents the serving UBS, which can be in LoS or NLoS connection. The typical user is situated at the point $\mathbf{x}_0$, which is located at a distance y_0 from the origin.

where $l \in \{LoS, NLoS\}$. Based on the aforementioned assumptions, the serving UBS can be written as

$$A_0 = \arg\max_{i=1:N} \left\{ P_U \varphi_{LoS}^{-1} X_i^{-\alpha_U^{LoS}} \cup P_U \varphi_{NLoS}^{-1} X_i^{-\alpha_U^{NLoS}} \right\}, \tag{3.7}$$

To calculate the coverage probability, it is necessary to determine the SINR received at the typical user. We assume that the SA UBSs, except for the serving UBS, will cause interference to the typical user u, regardless of whether they are in LoS or NLoS states. The number of interfering UBSs is determined by $K-1$. Let denote by Z_i the distance from a random interfering UBS to user u. The aggregate interference is represented by I and can be expressed as follows

$$I = \sum_{i=1}^{K-1} \left(P_U \Omega(\omega, \theta(Z_i)) h_U^{LoS} {\varphi_{LoS}}^{-1} Z_i^{-\alpha_U^{LoS}} \cup P_U \Omega(\omega, \theta(Z_i)) h_U^{NLoS} {\varphi_{NLoS}}^{-1} Z_i^{-\alpha_U^{NLoS}} \right), \tag{3.8}$$

where $l \in \{LoS, NLoS\}$, $\Omega(\omega, \theta(Z_i))$ denotes the vertical antenna pattern gain of the interfering UBS.

Let denote by X_r^{LoS} and X_r^{NLoS} the distance between u and the serving UBS A_0 in LoS and NLoS states, respectively. The SINR received at u is formulated as follows

$$SINR = \frac{P_U \Omega(\omega, \theta(X_r^l)) h_U^l {\varphi_l}^{-1} {X_r^l}^{-\alpha_U^l}}{I + N_0}, \tag{3.9}$$

where $l \in \{LoS, NLoS\}$, $\Omega(\omega, \theta(X_r^l))$ denotes the vertical antenna pattern gain of the UBS A_0 and N_0 is the additive white Gaussian noise signal power.

3.6 Probability Density Function

The characterization of the distribution of distances is a crucial step in achieving the association probability and coverage probability. Obtaining the distance distribution for BPP-based finite networks is more challenging compared to PPP due to the derivation area sometimes being an intersection of two disks when the location $\mathbf{x}_0$ of the typical user is not at the center of the target area. The PDF of the distance X_i between u and an arbitrary UBS A_i conditioned on the distance y_0 is provided by Lemma 3.6.1.

Lemma 3.6.1. *The PDF of X_i conditioned on y_0 is*

$$f_{X_i}(x \mid y_0) = \begin{cases} \dfrac{2x}{r_a^2}, & h \le x \le x_m, \\ \dfrac{2x}{\pi r_a^2} \arccos\left(\dfrac{x^2 - h^2 + y_0^2 - r_a^2}{2y_0(x^2-h^2)^{\frac{1}{2}}}\right), & x_m \le x \le x_u, \end{cases} \tag{3.10}$$

where $x_m = \sqrt{(r_a - y_0)^2 + h^2}$ and $x_u = \sqrt{(r_a + y_0)^2 + h^2}$.

Proof: The CDF of each distance X_i can be written as

$$\begin{aligned} F_{X_i}(x_i) = \mathbb{P}(X_i \le x_i) =& \mathbb{P}(Y_i^2 + h^2 \le x_i^2) \\ =& F_{Y_i}(\sqrt{x_i^2 - h^2}), \end{aligned} \tag{3.11}$$

Since $\mathbf{x}_0$ is random within the $B_r(O, r_a)$ area, we need to determine the intersection area of the two discs $B_r(O, r_a)$ and $B_r(\mathbf{x}_0, y_i)$ to calculate the conditional CDF of Y_i. There are two possible cases depending on the range of y_i: (i) the disc $B_r(\mathbf{x}_0, y_i)$ is completely contained within the disc $B_r(O, r_a)$, and (ii) $B_r(\mathbf{x}_0, y_i)$ partially overlaps with $B_r(O, r_a)$. This results in a piece-wise conditional CDF of Y_i, as shown below [139]

$$F_{Y_i}(y_i \mid y_0) = \begin{cases} \dfrac{y_i^2}{r_a^2}, & 0 \le y_i \le y_m, \\ \dfrac{y_i^2}{\pi r_a^2}\left(\theta^* - \dfrac{\sin 2\theta^*}{2}\right) + \dfrac{1}{\pi}\left(\phi^* - \dfrac{\sin 2\phi^*}{2}\right), & y_m \le y_i \le y_u, \end{cases} \tag{3.12}$$

where $\theta^* = \arccos\left(\dfrac{y_i^2 + y_0^2 - r_a^2}{2y_i y_0}\right)$, $\phi^* = \arccos\left(\dfrac{r_a^2 + y_0^2 - y_i^2}{2r_a y_0}\right)$, $y_m = r_a - y_0$ and $y_u = r_a + y_0$.

By substituting (3.12) into (3.11), we can obtain the conditional CDF of X_i as follows

$$F_{X_i}(x_i \mid y_0) = \begin{cases} \dfrac{x_i^2 - h^2}{r_a^2}, & h \le x_i \le x_m, \\ \dfrac{x_i^2 - h^2}{\pi r_a^2}\left(\theta^* - \dfrac{\sin 2\theta^*}{2}\right) + \dfrac{1}{\pi}\left(\phi^* - \dfrac{\sin 2\phi^*}{2}\right), & x_m \le x_i \le x_u, \end{cases} \tag{3.13}$$

where $\theta^* = \arccos\left(\dfrac{x_i^2 - h^2 + y_0^2 - r_a^2}{2y_i y_0}\right)$, $\phi^* = \arccos\left(\dfrac{r_a^2 + y_0^2 - x_i^2 + h^2}{2r_a y_0}\right)$, $x_m = \sqrt{(r_a - y_0)^2 + h^2}$ and $x_u = \sqrt{(r_a + y_0)^2 + h^2}$. Taking the derivative of $F_{X_i}(x_i \mid y_0)$ w.r.t. x_i yields (3.10).

3.6.1 Conditional Serving Distance Distribution

The conditional serving and interfering distance distributions provide intermediate results for obtaining the statistical characteristics of the desired signal and aggregate interference, which are necessary to derive the coverage probability.

We refer to the conditional distance from the typical user to LoS/NLoS UBS by $X_r^{\hat{L}oS}$, $X_r^{\hat{N}LoS}$ respectively. The PDF of $\hat{X}_r^l$ conditioned on y_0, denoted by $f_{\hat{X}_k r^l}(r \mid y_0)$ is given in the following Lemma.

Lemma 3.6.2. *The conditional PDF of the distances $\hat{X}_r^l$ is*

$$f_{\hat{X}_r^l}(r \mid y_0) = \frac{N P_U^l(r)}{A_U^l(y_0)} \left(\int_{R_{LoS}^{NLoS}(r)}^{x_u} f_{X_i}(x \mid y_0) P_U^{LoS}(x) dx + \int_{R_{NLoS}^{LoS}(r)}^{x_u} f_{X_i}(x \mid y_0) P_U^{NLoS}(x) dx \right)^{N-1}, \tag{3.14}$$

Proof: The CDF of $\hat{X}_r^l$ can be written as

$$\begin{aligned} F_{\hat{X}_r^l}(r \mid y_0) &= \mathbb{P}\left(X_r^l < r | u \text{ is associated with UBS in } l \text{ link}\right) \\ &= \frac{\mathbb{P}\left(X_r^l < r, u \text{ is associated with UBS in } l \text{ link}\right)}{\mathbb{P}(u \text{ is associated with UBS in } l \text{ link})} \\ &= \frac{N}{A_U^l(y_0)} \int_{x_u}^{r} P_U^l(q) f_{X_i}(q \mid y_0) \\ &\times \left(\int_{R_{LoS}^{NLoS}(r)}^{x_u} f_{X_i}(x \mid y_0) P_U^{LoS}(x) dx + \int_{R_{NLoS}^{LoS}(r)}^{x_u} f_{X_i}(x \mid y_0) P_U^{NLoS}(x) dx \right)^{N-1} dq, \end{aligned} \tag{3.15}$$

where $l \in \{LoS, NLoS\}$. Deriving $F_{\hat{X}_r^l}(r \mid y_0)$ w.r.t. q yields (3.14).

3.6.2 Conditional Interfering Distance Distribution

For networks based on PPPs, PGFL is a well-developed tool for efficiently dealing with aggregate interference as shown in Chapter 1. However, PGFL cannot be used in BPP-based network.

To accomplish this, we derive the PDF of the distance Z_i from an arbitrary interfering UBS to u located at $\mathbf{x}_0$. Wang *et al.* [46] have demonstrated that when UBSs are i.i.d. in a finite disk according to BPP, the distance Z_i between any two interfering UBSs is independent.

Lemma 3.6.3. *The conditional PDF of the interference distance Z_i*
We denote by $\mathcal{B}_{R_l^v(r)}$ the event that the interfering UBS being in $v \in \{LoS, NLoS\}$ is located $R_l^v(r)$ away from u and assume that r be the distance between u and its associated UBS in $l \in \{LoS, NLoS\}$. The conditional PDF of Z_i is then given by

$$f_{Z_i}\left(z|\mathcal{B}_{R_l^v(r)}, y_0\right) = \frac{f_{X_i}(z \mid y_0) P_U^v(z)}{\int_{R_l^v(r)}^{x_u} f_{X_i}(z \mid y_0) P_U^v(z) dz}, \tag{3.16}$$

Proof: It's worth noting that Z_i is the distance X_i conditioned on $\mathcal{B}_{R_l^v(r)}$, then we begin by presenting the conditional CDF of X_i as follows

$$\begin{aligned} F_{X_i}\left(x|\mathcal{B}_{R_l^v(r)}, y_0\right) =& \mathbb{P}\left(X_i < x|\mathcal{B}_{R_l^v(r)}, \text{conditioned on the distance } y_0\right) \\ =& \frac{\mathbb{P}\left(X_i < x, \mathcal{B}_{R_l^v(r)}, y_0\right)}{\mathbb{P}\left(\mathcal{B}_{R_l^v(r)}, y_0\right)} \\ =& \frac{\int_{R_l^v(r)}^{x} f_{X_i}(z \mid y_0) P_U^v(z) dz}{\int_{R_l^v(r)}^{x_u} f_{X_i}(z \mid y_0) P_U^v(z) dz}, \end{aligned} \tag{3.17}$$

After deriving (3.17) and substituting X_i with Z_i, we obtain the desired result in (3.16).

3.7 Conclusion

This chapter proposed a 3D model of a mmWave UBS swarm in a finite isolated region where wireless connectivity cannot be achieved with traditional GBSs. In this context, the network and channel models are described, with the pertinent assumptions delineated. The number of simultaneously active UBSs reusing the same resource block can be controlled, and the 3D beamforming technique is implemented to mitigate interference and further improve the network performance. Stochastic geometry is employed as the modeling tool, in which the BPP is used for the UBS spatial distribution. A cell association strategy based on the strongest

received signal power is adopted, and the formulation of the SINR is provided. Finally, the expressions of the probability density function of the serving and interfering distances, which are crucial for the derivation of the coverage probability, are derived.

Chapter 4

Modeling of Vertical Heterogeneous Networks Under 3D Blockage Effects

Contents

4.1 Introduction **56**
4.2 UBS Deployment in Hotspot Scenarios **56**
4.3 mmWave Communication Issues in Dense Cities **57**
4.4 Multiuser MIMO Communication Systems **58**
4.5 System and Channel Modeling **60**
4.5.1 Network Model and Assumptions 60
4.5.2 3D Blockage Model 60
4.5.3 Channel Propagation Model 62
4.5.4 Directional Beamforming Gain 66
4.5.5 User Association and SINR Model 67
4.5.6 Extension to A Model With 3D Beamforming 70
4.6 Probability Density Function **70**
4.6.1 Distance Distribution in the UBS Tier 70
4.6.2 Distance Distribution in the 0^{th} Tier 71
4.6.3 Distance Distribution in the 1^{st} Tier 71
4.6.4 Conditional Serving Distance Distribution 71
4.6.5 Conditional Interfering Distance Distribution 72
4.7 Conclusion **72**

4.1 Introduction

A significant challenge currently facing 5G network operators is to provide seamless and ubiquitous coverage in dense urban areas characterised by high-rise buildings, while ensuring that all users have access to reliable and high-quality services. Moreover, the static infrastructure of the terrestrial network can fail to keep up with the huge demand from users, creating a congested and saturated network. To address this issue, a novel network infrastructure must be considered. In the literature, VHetNets [44–47, 99, 140] have been investigated to enable global 3D communication network coverage, overcoming the limitations of traditional terrestrial networks. However, there are still unaddressed issues in this context, including the impact of 3D blockages.

In this chapter, we propose a new 3D model of mmWave VHetNets in which the aerial tier is deployed to assist the terrestrial tier in dense urban areas with high user density and 3D blockage effects. We adopt a new combination of technologies consisting of MU-MIMO beamforming with UAV-enabled mmWave communications. In this context, we present the system model and assumptions based on the BPP, PPP, and PCP stochastic geometry tools, we define the user association approach and derive the SINR. Finally, we compute the probability density function of the distances between the typical user and the BS in each tier.

4.2 UBS Deployment in Hotspot Scenarios

In situations of high user concentration, such as festivals, concerts, and the olympic games, traditional BSs may not have the capacity to meet the user demand and sudden surge of broadband, creating an overloaded infrastructure area. Therefore, it is important to consider alternative solutions in these temporary areas. The deployment of multiple UBSs is a promising solution to assist and complement terrestrial networks. These UBSs will be autonomously controlled, dispatched as a network requires, cheaply maintained, and easily manoeuvred. The backhaul bit rates required for each UBS radio access node could be several Gbps, depending on the traffic load.

On the other hand, VHetNets can also offer an intriguing opportunity during natural disasters, e.g., floods, tornadoes, earthquakes, and violent snowstorms, where dependable and adaptable communications are crucial for search and rescue operations [141]. A rotary-wing UBS can carry out high-risk missions, creating resilient communication networks. In addition, coverage gaps can also occur due to man-made phenomena such as subsystem failures. It is worth noting

that, users congregate in these particular regions, resulting in the formation of clusters. Consequently, the PCP is commonly employed. UAV-assisted cellular networks with PCP-based user distribution in a post-disaster situation were studied in [140–142].

4.3 mmWave Communication Issues in Dense Cities

The combination of VHetNets with mmWave communications offers several benefits. These include spatial sparsity, flexible beamforming, increased resistance to the Doppler effect when used with mobile UBSs, and cost reduction of wired backhaul in terrestrial networks. Nevertheless, the propagation of these waves is considerably susceptible in densely populated urban areas, and this phenomenon has not been extensively studied by researchers.

Sensitivity to Blockage

mmWave communications experience significant propagation loss due to beam misalignment [143] and blockage effects, such as building blockages [113], human-body blockages [144] and self-blockages [145], that may limit the performance. These waves are easily and rapidly attenuated by significant obstructions due to their short range, leading to intricate propagation conditions in the channel. For instance, at a frequency of 60 GHz, the wavelength measures only 5 millimeters, while the size of a building is significantly larger. As a result, the wave encounters significant difficulty in penetrating or diffusing through a building and communication can be severely disrupted. In reality, mmWaves primarily rely on LoS transmission. Geng *et al.* [146] noted that the channel characterization of NLoS experiences greater attenuation than that of LoS. Deploying UAV networks can help address this issue more effectively than terrestrial networks. According to the results obtained in [70] and the measurements reported in [147], the higher altitude of UBSs leads to a higher probability of establishing LoS links than GBSs, which improves channel quality.

Hotspots frequently arise in dense urban areas where multiple buildings can interfere with communication links. Therefore, when analyzing coverage in hotspot areas, it is crucial to consider the 3D blockage effect of buildings. Performance analysis has been conducted on hotspots in mmWave cellular networks with only ground tier in [148, 149]. Recent studies have focused on the integration of UBSs into mmWave cellular networks in crowded hotspot areas using cluster-based model [45, 96, 133, 138]. However, the blockage effect of buildings on the coverage performance has not been addressed in the aforementioned works.

Compared to 2D blockage models where the presence of a building results in a blocked link, 3D models can facilitate unobstructed connections by considering building height. However, 3D blockages can create spatial constraints for UBS distribution since they cannot be deployed inside building areas and affect the cell association strategy. Previous works have not taken into account this dependent deployment, where UBSs are distributed to BPP [110, 126, 127]. The investigation of 3D blockage effects on UAV-based communication has not received much attention in the open literature [48, 49] and has not been addressed in the VHetNets.

4.4 Multiuser MIMO Communication Systems

MIMO technology was developed as an ideal solution to the limited frequency spectrum available and the increasing demand for higher data transmission rates without the need for extra bandwidth. MIMO provides the advantage of spatial multiplexing, allowing for the simultaneous transmission of multiple data streams using different antennas. This makes it a viable solution for dealing with heavy propagation losses in mmWave links. Traditional MIMO or single user MIMO (SU-MIMO) increases the capacity of a single user by directing all transmit antennas towards it. However, when multiple users are present, each one must wait their turn to receive the signal in a round-robin fashion.

The MU-MIMO system is a promising technology for congested networks with a high density of users. It can significantly improve system capacity by using MIMO channels in combination with multiuser multiplexing schemes. This technology enables a BS to serve multiple users simultaneously using the same frequency resources, as shown in Figure 4.1. This provides spatial degrees of freedom of the channel leading to substantially increased spectral efficiency and

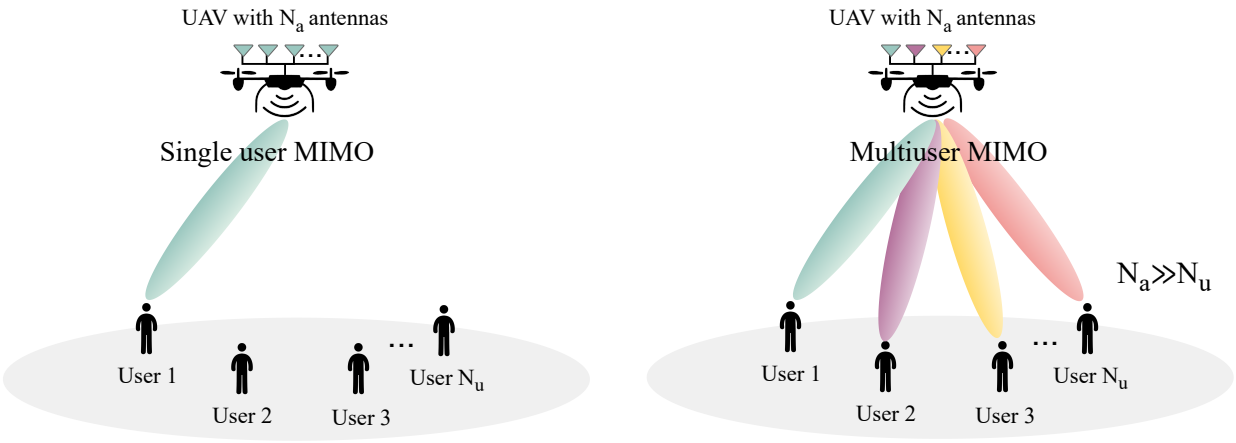

Figure 4.1: Illustration of downlink UBS with SU-MIMO and MU-MIMO systems.

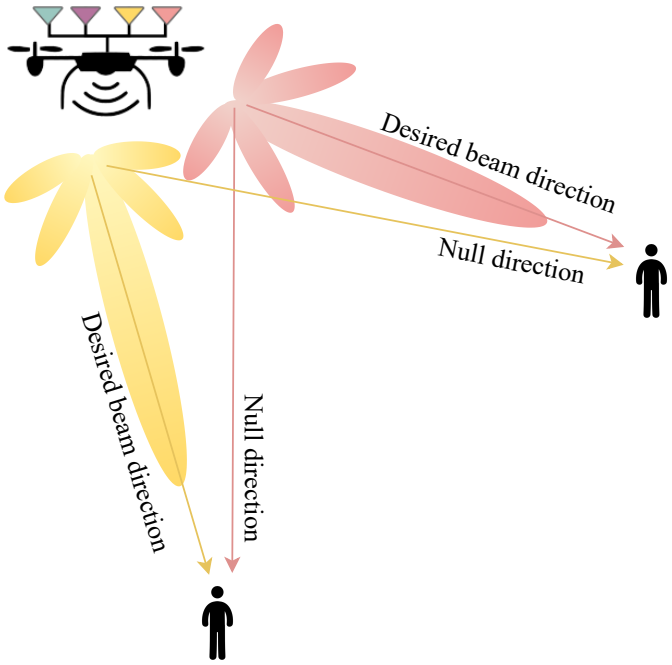

Figure 4.2: Downlink MU-MIMO beamforming.

thus expands upon traditional MIMO capabilities. The integration of MU-MIMO technology with UBSs offers new opportunities and advantages compared to its use with fixed GBSs. This approach allows for adaptive beamforming and dynamic deployment, especially in disaster-affected areas or crowded public events, improving thus coverage and connectivity.

The capacity of multiuser communication systems is restricted by interference. Several precoding techniques have been developed to address the interference issue such as zero forcing beamforming (ZFBF) [150] in which the simultaneously active users receive informations without interferences through the transmission signal being projected into the interference subspace's null space, minimum mean square error (MMSE) [151] which combines consideration of noise and channel uncertainty with channel state information (CSI), and interference alignment [152] in which multiple users' interference is oriented into orthogonal subspaces.

MIMO UAV-cellular communication in a geometry-based stochastic model have been widely analyzed in the literature [153, 154]. However, the literature has not extensively analyzed the performance in a MU-MIMO system for UAV networks.

The 3D model proposed in this chapter explores the use of a combination of MU-MIMO and directional beamforming in mmWave aerial networks as illutrated in Figure 4.2, to enhance signal quality and improve the received SINR at the user. To the best of our knowledge, this combination has not been previously studied in the literature in the context of coverage analysis using stochastic geometry.

4.5 System and Channel Modeling

The work presented in this section [155] represents an evolution of our previous work, provided in [156].

4.5.1 Network Model and Assumptions

We focus on more realistic ground hotspots, considering a densely populated city, with the presence of buildings causing 3D blockage effects. To alleviate traffic congestion and enhance coverage on mmWave cellular networks, we employ a predefined number N of UBSs in a finite circular region to establish VHetNets, as illustrated in Figure 4.3. The UBS tier and the infinite GBS tier share the same frequency band. The time is assumed to be stationary.

The set of GBS locations is denoted by $\Phi_G = \{M_j, j \in \mathbb{N}\}$. The locations M_j are assumed to be spatially distributed according to HPPP with a spatial density of $\lambda_G \geq 0$. All GBSs transmit with equal power, denoted by, P_G. The modeling of UBS locations follows the BPP distribution, as described in the previous chapter 3 (section 3.5). We assume that both UBSs and GBSs incorporate directional beamforming. We consider that GBSs and users are equipped with a single antenna. MU-MIMO is considered at the UBSs, where each UBS is equipped with an N_a antenna array serving N_u users $(1 < N_u \ll N_a)$.

The users are clustered around the GBSs, and their locations form a TCP denoted by Φ_C. Therefore, the users are i.i.d. around the cluster centers, following a Gaussian distribution with a zero mean and a variance σ_u^2. Our analysis is conducted on a typical user u in the target area B_g, which is the projection of B_a onto the plane. To ensure clarity, we randomly selected u within a random cluster (termed a representative cluster) and set it as the origin. The link between a UBS or GBS and u can be in either a LoS or NLoS state.
The UBS deployment in our model mainly depends on the capacity of GBSs (cluster center) to cover user hotspots, that's why the position of the UBSs relative to the hotspot is irrelevant.

4.5.2 3D Blockage Model

In this study, we aim to investigate the impact of LoS/NLoS propagation to fit the characteristics of mmWave communication, where the existing studies on 3D blockage consider only the LoS propagation channel and a nearest UBS-based user association, such an approach is impractical and doesn't reflect the emission power and neglects the randomness in the channel propagation. We propose more sophisticated models of the wireless propagation channel to

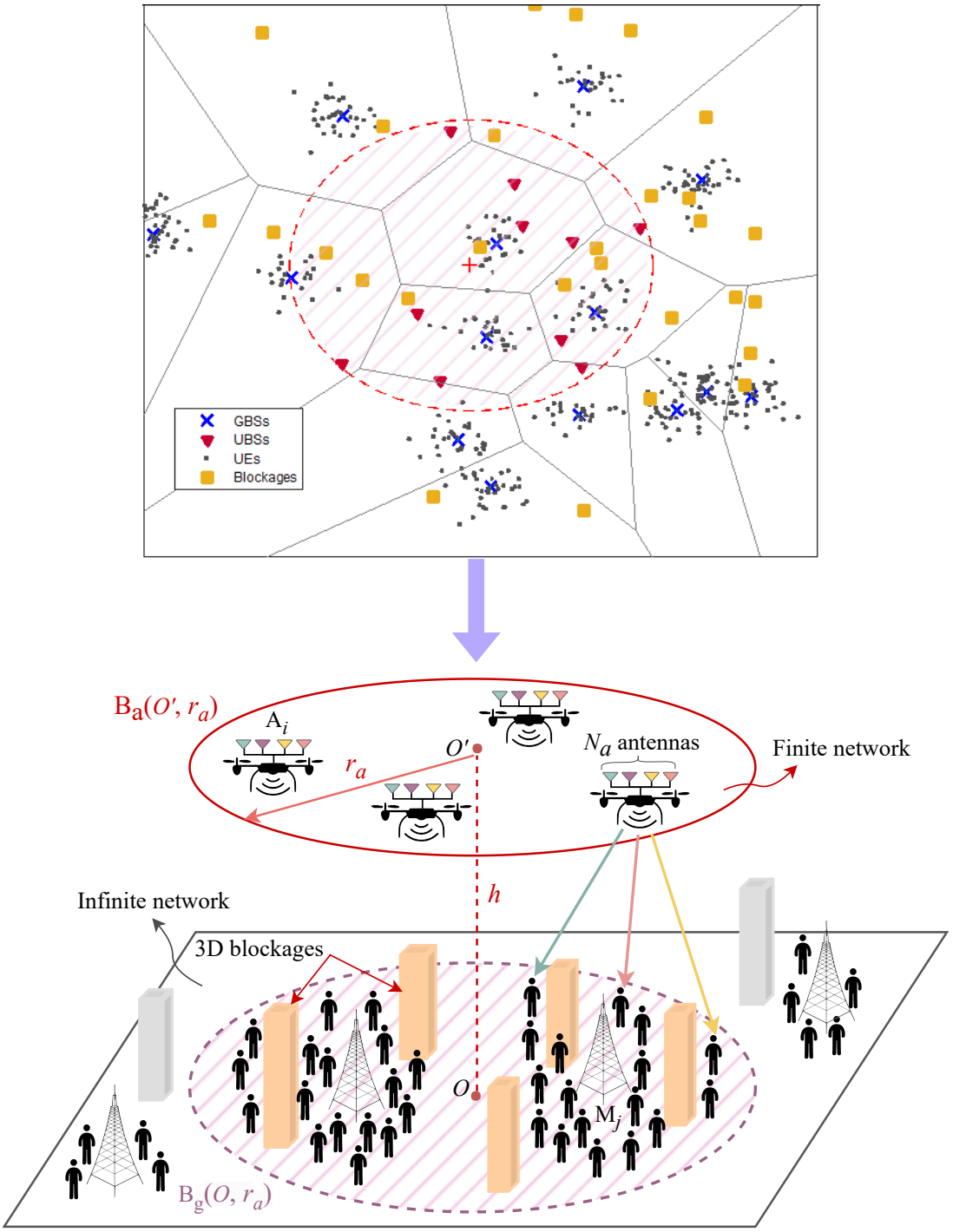

Figure 4.3: Illustration of the VHetNet with 3D blockages of buildings.

capture the 3D blockage. UBS's flying capability creates unobstructed A2G channels, resulting in a higher LoS probability compared to G2G connections, as shown in Figure 4.4. We use a Boolean scheme of rectangles to model randomly located buildings [36]. The buildings are distributed according to an HPPP ϕ_B with a density of $\lambda_B \geq 0$, ensuring that their locations, sizes, and orientations are independent. The buildings' length L_B and width W_B are i.i.d. with mean values of $\mathbb{E}[L_B]$ and $\mathbb{E}[W_B]$, respectively. As per [113], the buildings can be considered

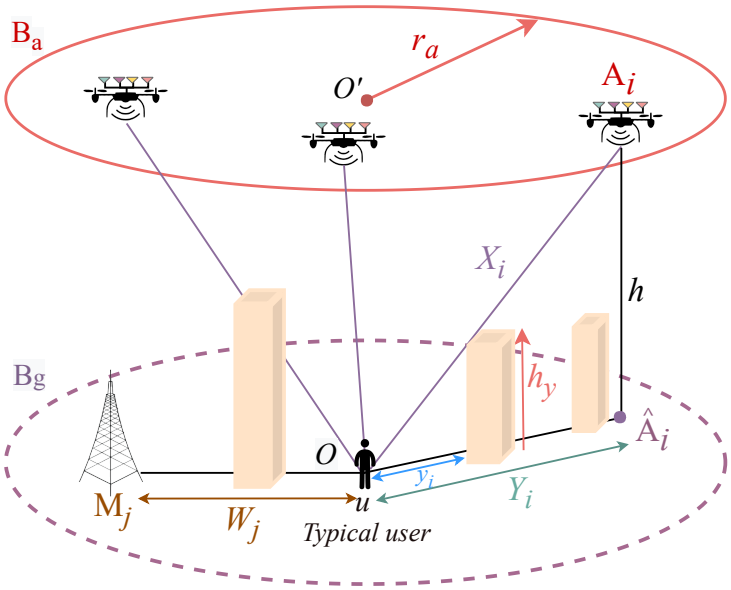

Figure 4.4: 3D blockage model and view of the benefit of the UBSs's altitude to prevent obstructed connection.

symmetric, eliminating the need to specify their orientations. We neglect the overlapping of buildings and consider that building height H_B follows an exponential distribution with parameter μ, the CDF of H_B can be expressed as follows

$$F_{H_B}(h_B) = 1 - e^{-\mu h_B} \quad h_B \geq 0, \tag{4.1}$$

Note that the buildings average height is then given by $\overline{H}_B = \frac{1}{\mu}$.

4.5.3 Channel Propagation Model

Large Scale Path loss

Blockages in A2G and G2G links cause significant differences in path losses between LoS and NLoS scenarios, particularly in mmWave communications. To account for the greater impact of NLoS compared to LoS, we assume that NLoS has the highest path loss exponent. The UBS path loss model is formulated as follows [46]

$$\Upsilon_U^l(X_i) = \begin{cases} \Upsilon_U^{LoS}(X_i) = {X_i}^{-\alpha_U^{LoS}}, \\ \\ \Upsilon_U^{NLoS}(X_i) = {X_i}^{-\alpha_U^{NLoS}}, \end{cases} \tag{4.2}$$

where $X_i = \sqrt{Y_i^2 + h^2}$ is the distance between u and the UBS A_i, h is the UBS altitude, Y_i is the distance between u and $\hat{A}_i$, which is the projection of A_i on the plane. α_U^{LoS} and α_U^{NLoS} are the path loss exponents for LoS/NLoS cases in the UBS tier.

For the terrestrial links, we adopt the following 3GPP path loss function [109]

$$\Upsilon_G^l(W_j) = \begin{cases} \Upsilon_G^{LoS}(W_j) = {W_j}^{-\alpha_G^{LoS}}, \\ \\ \Upsilon_G^{NLoS}(W_j) = {W_j}^{-\alpha_G^{NLoS}}, \end{cases} \tag{4.3}$$

where W_j is the distance between u and GBS M_j, α_{LoS}^G and α_{NLoS}^G are the path loss exponents for LoS and NLoS links in the terrestrial tier, respectively.

Small Scale Fading

We assume that LoS and NLoS links in each tier experience Nakagami-*m* fading, with shape and scale parameters given by $\left(m_t^l, \frac{1}{m_t^l}\right)$, where $t \in \{U, G\}$, $l \in \{LoS, NLoS\}$. Additionally, as the UBSs are equipped with MIMO antennas serving multiple N_u users, we use zero-forcing beamforming with perfect CSI in UBS tier. The Nakagami fading gains in the UBS tier, denoted by h_U^l, and in the ground tier, denoted by h_G^l, follow the gamma distribution, and can be expressed as follows $h_U^l \sim \Gamma\left(m_U^l M, \frac{1}{m_U^l}\right)$ and $h_G^l \sim \Gamma\left(m_G^l, \frac{1}{m_G^l}\right)$, where $M = N_a - N_u + 1$ denotes the array gain for zero forcing beamforming transmission [112].

Shadowing

The log-normal shadowing power S may be expressed by $S_t^l = 10^{-\frac{S_{tdB}^l}{10}}$, where S_{tdB}^l has a normal distribution with zero mean and ${\sigma_{S_t^l}}^2$ variance and $l \in \{LoS, NLoS\}$. The variance in the UBS tier depends on the elevation angle and environment type, as reported in [73]. Therefore, the variance of LoS and NLoS UBS can be written as

$$\sigma_{S_U}^{LoS}(h) = b_1 \exp\left(-b_2 \sin^{-1}\left(\frac{h}{Y_i}\right)\right), \tag{4.4}$$

$$\sigma_{S_U}^{NLoS}(h) = b_1' \exp\left(-b_2' \sin^{-1}\left(\frac{h}{Y_i}\right)\right), \tag{4.5}$$

where b_1, b_2, b_1' and b_2' are constants that depend on the environment and $\sin^{-1}\left(\frac{h}{Y_i}\right)$ is the elevation angle between the typical user and the UBS located in A_i.

LoS and NLoS Probabilities

In practice, not all multipath components may be obstructed by buildings. Therefore, in this study we classify a blocked link as an NLoS link. The LoS and NLoS probabilities (3.2), (3.3) applied in the isolated regions model presented in the preceding chapter are not suitable

for application to dense urban environments due to the presence of multiple 3D buildings that can interfere with the communication link between the user and the UBS. To this end, we develop new probability formulas for LoS and NLoS, which will be based on the exponential distribution of building heights. The formulas provide a more precise representation of the impact of buildings on communication links.
We denote by OA_i and $O\hat{A}_i$ the link from u to UBS A_i and the link from u to $\hat{A}_i$, respectively. Similarly, the link from GBS M_j to u is denoted as OM_j.

- **2D Blockage Effect**

The terrestrial network model has only been limited to the $\mathbb{R}^2$ plane (2D G2G channel), neglecting the height of GBSs and users, as well as the height of buildings. Consequently, the presence of a building obstructs the G2G link. The A2G channel is considered in 3D. However, to obtain the expressions in the 3D model, we must first derive the expressions in 2D model.

$\hat{K}_i$ and B_j, the number of buildings crossing the links $O\hat{A}_i$ and OM_j respectively, are Poisson distributed random variables, as demonstrated in [113]. Their means are $\mathbb{E}[\hat{K}_i] = \beta Y_i + p$, and $\mathbb{E}[B_j] = \beta W_j + p$. Here, Y_i and W_j represent the horizontal distance from UBS to u and from GBS to u, respectively. β and p are parameters of blockage processes, where $\beta = \frac{2\lambda_B(\mathbb{E}[W_B]+\mathbb{E}[L_B])}{\pi}$, and $p = \lambda_B \mathbb{E}[W_B]\mathbb{E}[L_B]$. p represents the index of city blockage density. A low p-value indicates that blockages are not widely distributed, and vice versa. By using the properties of the Poisson distribution, the derived corollary results enable the expression of the probabilities of horizontal LoS and NLoS for the link $O\hat{A}_i$ and OM_j as follows

$$P^{l}_{U_{(2D)}}(Y_i) = \begin{cases} P^{LoS}_{U_{(2D)}}(Y_i) = e^{-(\beta Y_i + p)}, \\ \\ P^{NLoS}_{U_{(2D)}}(Y_i) = 1 - e^{-(\beta Y_i + p)}, \end{cases} \tag{4.6}$$

$$P^{l}_{G}(W_j) = \begin{cases} P^{LoS}_{G}(W_j) = e^{-(\beta W_j + p)}, \\ \\ P^{NLoS}_{G}(W_j) = 1 - e^{-(\beta W_j + p)}, \end{cases} \tag{4.7}$$

- **3D Blockage Effect**

In the UBS tier, the presence of a building along the OA_i link does not always lead to a NLoS link, unless the building's height is significant enough to block the connection. This intuitively enhances the probability of establishing a direct A2G communication link. Figure 4.4 shows that the obstruction of the path is dependent on the height of the building that intersects it,

which is determined by $\overline{H}_B > h_y = \frac{y_i}{Y_i}h$, where y_i is the horizontal distance between u and the building.

The LoS and NLoS probabilities in the UBS tier are given in Lemma. 4.5.1.

Lemma 4.5.1. *The probability of LoS and NLoS of the A2G channel are expressed as follows*

$$P_U^{LoS}(X_i) = \exp\left(-\frac{1-e^{-\overline{H}_B^{-1}h}}{\overline{H}_B^{-1}h}\left(\beta\sqrt{X_i^2-h^2}+p\right)\right), \tag{4.8}$$

$$P_U^{NLoS}(X_i) = 1 - P_U^{LoS}(X_i), \tag{4.9}$$

Proof: Consider K_i the number of buildings intersecting the link OA_i, which follows a Poisson distribution. The conditional probability of K_i obstructing the OA_i link can be written as follows

$$\begin{aligned}\eta &= \frac{1}{Y_i}\int_0^{Y_i}\mathbb{P}[\overline{H}_B > h_y]\,dy_i \\ &= \frac{1}{Y_i}\int_0^{Y_i}\left(1-F_{\overline{H}_B}(h_y)\right)\,dy_i \\ &= \frac{1}{Y_i}\int_0^{Y_i}e^{-\mu\frac{y_i}{Y_i}h}dy_i \\ &\overset{(a)}{=} \frac{1-e^{-\overline{H}_B^{-1}h}}{\overline{H}_B^{-1}h},\end{aligned} \tag{4.10}$$

where (a) follows from $\mu = \frac{1}{\overline{H}_B}$. Then the mean of K_i is $\mathbb{E}[K_i] = \eta\,\mathbb{E}[\hat{K}_i]$. Based on equation (4.6), the probability of LoS in the 3D model can be expressed as

$$P_U^{LoS}(X_i) = \exp\left(-\eta\left(\beta\sqrt{X_i^2-h^2}+p\right)\right), \tag{4.11}$$

Substituting the expression of η in (4.11) yields (4.8).

By examining (4.8), we observe that the probability of LoS link occurrence is influenced by various factors such as building density, height, area, and the altitude of UBSs. This differs from the conventional equation used in the scenario of isolated region (3.2), which primarily hinges on the elevation angle between the UBS and the user.

To get an overview of the 3D blockage effects on the aerial communication link, we plotted in Figure 4.5, the new LoS probability given in (4.8) and the LoS probability given in (3.2) as a function of UBS altitude h with different values of λ_B. From Figure 4.5, it can be seen that there is a direct relationship between the probability to have a LoS link and the UBS altitude h. Furthermore, it can be observed that when a simple A2G channel is considered, without accounting for 3D building characteristics, the LoS probability rapidly approaches 1, in contrast

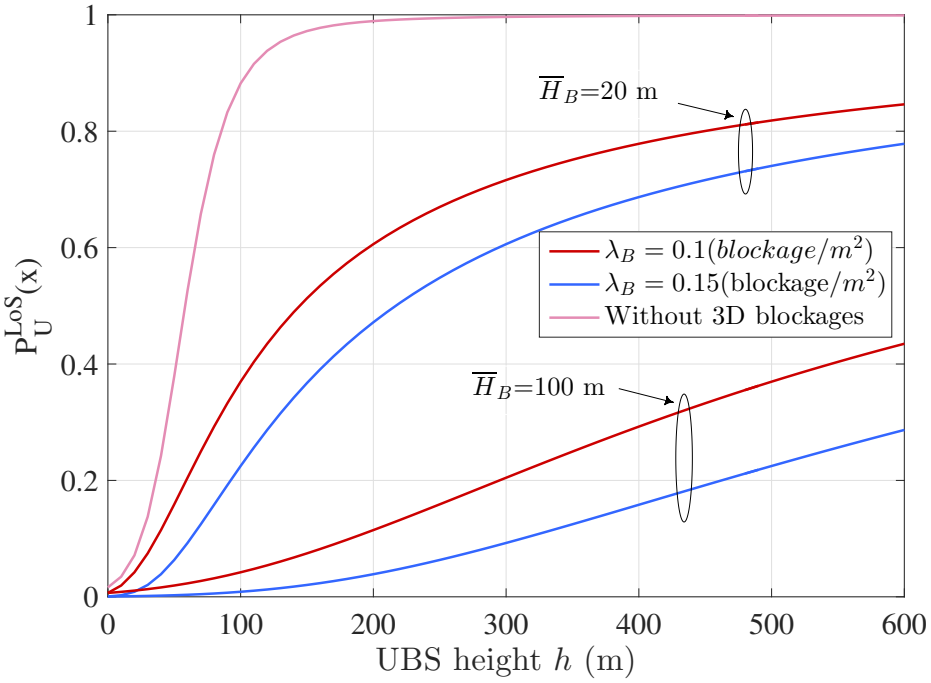

Figure 4.5: LoS probability vs. UBS height for different blockage densities.

to the new channel with 3D blockages. Indeed, the higher altitude of UBSs promotes higher LoS probability in contrast, the increase in building height or in blockage density decreases the LoS probability.

4.5.4 Directional Beamforming Gain

Given the nature of mmWave transmissions, we employ directional beamforming to reduce interference. Subsequently, the analysis will be extended with 3D beamforming and a comparison will be made between the two techniques. The sector antenna model was used to approximate the array patterns, as illustrated in Figure 4.6, with characteristics including main lobe beamwidth θ_t, main lobe gain g_t, and side lobe gain s_t, where ($t \in \{U, G\}$). The sectored antenna model assumes constant array gains, g_t, for all angles in the main lobe and another constant, s_t, in the side lobe. However, it is important to note that g_t represents the maximum antenna gain that can be achieved between the typical user and the serving BS. The directional gain of the BS antenna, denoted by G_t is provided by

$$G_t = \begin{cases} g_t, & P_{g_t} = \dfrac{\theta_t}{2\pi}, \\ \\ s_t, & P_{s_t} = 1 - P_{g_t}, \end{cases} \tag{4.12}$$

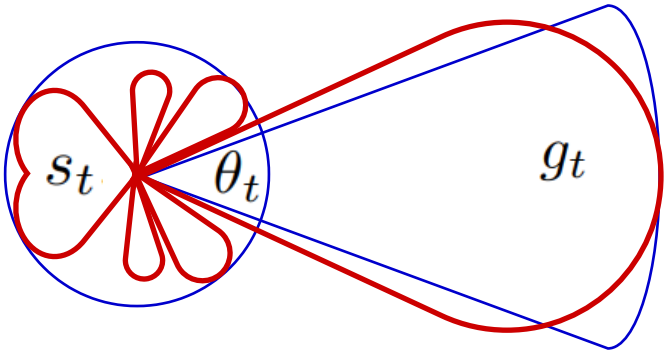

Figure 4.6: Illustration the sectored antenna model used to approximate the beamforming patterns. The red line shows a more realistic antenna model. The blue line shows the approximation taken into consideration [40].

where P_{g_t} and P_{s_t} are the probabilities of the main lobe and the side lobe, respectively. We adopt perfect beam alignment therefore g_t is the received gain from the serving BS.

4.5.5 User Association and SINR Model

Since the users cluster around GBSs based on TCP, the distance distribution between the typical user and the representative cluster center differs from the distance distribution between the typical user and the center of any other cluster. Consequently, we devide the ground tier into two tiers: 0^{th} tier (GBS$_0$), which represents the cluster center, and 1^{st} tier (GBS$_1$), which represents the other GBSs. Therefore, the typical user u can be associated with either LoS/NLoS UBS, LoS/NLoS GBS$_0$, or LoS/NLoS GBS$_1$, whichever provides the strongest long-term averaged received power.

To distinguish between GBS$_0$ and GBS$_1$, we use W_0 to denote the distance from u to GBS$_0$ and W_j to denote the distance from u to GBS$_1$, as illustrated in Figure 4.7, while maintaining the same propagation channel.

With the assumption that $\mathbb{E}[h_U^l] = \mathbb{E}[h_G^l] = 1$ [138], the received power at u from UBS, GBS$_0$, and GBS$_1$ can be expressed as follows

$$\xi_U = P_U M G_U \Upsilon_U^l (X_i)^{-1}, \tag{4.13}$$

$$\xi_{G_0} = P_G G_G \Upsilon_G^l (W_0)^{-1}, \tag{4.14}$$

$$\xi_{G_1} = P_G G_G \Upsilon_G^l (W_j)^{-1}, \tag{4.15}$$

In the infinite network, the HPPP is used for the location of the GBSs. With the assumption that the Nakagami-*m* fading gain is equal to one, the GBS$_1$ with the shortest distance provides the strongest received power in the 1^{st} tier. However, in the 0^{th} tier the event that the GBS$_0$ be the serving BS is mutually exculsif as the GBS$_0$ can be in LoS or NLoS with u. Furthermore,

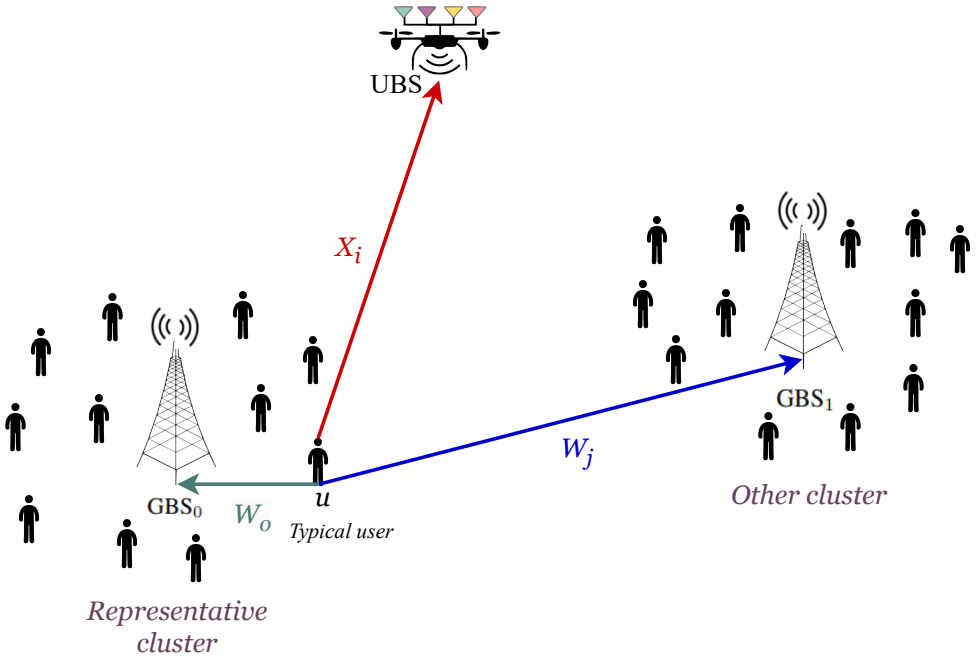

Figure 4.7: Distance from the typical user and the BS in each tier.

the events of the UBS being in either LoS or NLoS links are also mutually exclusive as they are i.i.d. in a finite disk as a BPP. As a result, the serving UBS cannot be the closest one. In this scenario, the serving UBS can be any of the N UBSs that can be in the LoS or NLoS link. If UBSs are distributed according to HPPP, the serving UBS will be the closest one to the user [44].

Of the three tiers, the serving BS, denoted by S_0, can be summarized by the following expression

$$S_0 = \arg\max \left\{ \max_{i=1:N} \left(P_U M g_t {X_i}^{-\alpha_U^{LoS}} \cup P_U M g_t {X_i}^{-\alpha_U^{NLoS}} \right), P_G g_t {W_0}^{-\alpha_G^{LoS}} \cup P_G g_t {W_0}^{-\alpha_G^{NLoS}}, \right.$$
$$\left. P_G g_t \left(\min W_j^{LoS} \right)^{-\alpha_G^{LoS}}, P_G g_t \left(\min W_j^{NLoS} \right)^{-\alpha_G^{NLoS}} \right\}, \tag{4.16}$$

Nearest Interfering Base Station

To derive the analytical expressions for the association probability, it is required to specify the excluded zone where there are no interfering BSs. Let r be the distance between u and its associated BS. Bearing that "xBS" is the serving BS in l link, there exists a minimum distance $R_{x^l}^{y^v}(r)$ between u and the closest interfering "yBS" in v link, where $l, v \in \{LoS, NLoS\}$ and $x, y \in \{U, G_0, G_1\}$.

Remark 1. Note that if xBS and yBS are simultaneously either UBSs or GBSs with the same link state,

$$R_{U^l}^{U^l}(r) = R_{G_0^l}^{G_1^l}(r) = R_{G_1^l}^{G_0^l}(r) = R_{G_1^l}^{G_1^l}(r) = r,$$

Remark 2. If xBS and yBS are simultaneously either UBSs or GBSs with a different link state,

$$R_{U^l}^{U^b}(r) = r^{\frac{\alpha_U^l}{\alpha_U^b}}, l \neq b$$

$$R_{G_0^l}^{G_1^b}(r) = R_{G_1^l}^{G_0^b}(r) = R_{G_1^l}^{G_1^b}(r) = r^{\frac{\alpha_G^l}{\alpha_G^b}}, l \neq b$$

Remark 3. If xBS and yBS are either UBSs or GBSs but not simultaneously,

$$R_{U^l}^{G_0^v}(r) = R_{U^l}^{G_1^v}(r) = \left(\frac{P_G G_G}{P_U M G_U}\right)^{\frac{1}{\alpha_G^v}} r^{\frac{\alpha_U^l}{\alpha_G^v}},$$

$$R_{G_0^l}^{U^v}(r) = R_{G_1^l}^{U^v}(r) = \left(\frac{P_U M G_U}{P_G G_G}\right)^{\frac{1}{\alpha_U^v}} r^{\frac{\alpha_G^l}{\alpha_U^v}},$$

Let X_r^l, W_0^l and W_r^l be the distance between the serving UBS, GBS$_0$ and GBS$_1$ in $l \in \{LoS, NLoS\}$, respectively. The SINR at u is defined as follows

$$SINR = \begin{cases} \dfrac{P_U g_U h_U^l X_r^{l-\alpha_U^l}}{I + N_0}, & \text{if } u \text{ is associated with UBS} \\ \dfrac{P_G g_G h_G^l W_0^{l-\alpha_G^l}}{I + N_0}, & \text{if } u \text{ is associated with GBS}_0 \\ \dfrac{P_G g_G h_G^l W_r^{l-\alpha_G^l}}{I + N_0}, & \text{if } u \text{ is associated with GBS}_1 \end{cases} \tag{4.17}$$

where N_0 is the additive white gaussian noise signal power.

In this study, all BSs are considered to be interfering BSs, with the exception of the serving BS. Consequently, the aggregate interference encompasses the aggregate interference from UBSs denoted by I_U, GBS$_0$ denoted by I_{G_0}, and GBS$_1$ denoted by I_{G_1}, which can be expressed as follows

$$I = I_U + I_{G_0} + I_{G_1}, \tag{4.18}$$

We denote by I_{U_i} the interference received from an arbitrary UBS. I_{U_i}, I_{G_0} and I_{G_1} are given as follows

$$I_{U_i} = P_U G_U \hat{h}_U^v {Z_i}^{-\alpha_U^v}, \tag{4.19}$$

$$I_{G_0} = P_G G_G h_G^v {W_0}^{-\alpha_G^v}, \tag{4.20}$$

$$I_{G_1} = \sum_v \sum_{M_j \in \Phi_G \setminus \psi_{t^l}^{G_1^v}} P_G G_G h_G^v {W_j}^{-\alpha_G^v}, \tag{4.21}$$

where $\hat{h}_U^v \sim \Gamma\left(m_U^v N_u, \frac{1}{m_U^v}\right)$ is the channel fading gain of the interfering UBSs. Z_i is the distance from u to a random interfering UBS. $\psi_{t^l}^{G_1^v}$ is a disk with radius $R_{t^l}^{G_1^v}(r)$ indicating the excluded area without any GBS$_1$ interference.

Remark 4. If u is served by the GBS$_0$, $I_{G_0} = 0$ since there is only one GBS$_0$.

4.5.6 Extension to A Model With 3D Beamforming

Since we have constrained the terrestrial network model to operate within a 2D plane, 3D beamforming will exclusively be implemented in UBSs, where we adjust the antenna radiation pattern in both the horizontal and vertical planes. The SINR received by the typical user from the UBS A_i will be formulated as follows

$$SINR = \frac{P_U g_U \Omega(\omega, \theta(X_r^l)) h_U^l {X_r^l}^{-\alpha_U^l}}{I + N_0}, \tag{4.22}$$

where $\Omega(\omega, \theta(\mathrm{X}_r^l))$ is the vertical antenna pattern gain of the serving UBS, given by

$$\Omega(\omega, \theta(X_r^l)) = 10^{-0.1 \times \min\left[12\left(\frac{\omega - \theta(X_r^l)}{\theta_d}\right)^2, SLL\right]}, \tag{4.23}$$

where $\theta(X_r^l) = \tan^{-1} \dfrac{h}{\sqrt{({X_r^l}^2 - h^2)}}$.

The singular modification in the aggregate interference $I = I_U + I_{G_0} + I_{G_1}$, lies in I_U which is formulated as

$$I_{U_i} = P_U G_U \Omega(\omega, \theta(Z_i^v)) \hat{h}_U^v {Z_i}^{-\alpha_U^v}, \tag{4.24}$$

4.6 Probability Density Function

We derive relevant distance distributions while considering the probabilities of occurrence of the LoS/NLoS links for both A2G and G2G channels.

4.6.1 Distance Distribution in the UBS Tier

Based on the Lemma 3.6.1 given in the previous chapter, for a typical user u located at the origin i.e. $y_0 = 0$, the PDF of the distance X_i from u to an arbitrary UBS A_i reduces to a simple expression, as shown in the following Corollary.

Corollary 4.6.1. *The PDF of X_i is*

$$f_{X_i}(x_i) = \frac{2x_i}{r_a^2}, \quad h \leq x_i \leq x_u, \tag{4.25}$$

where $x_u = \sqrt{r_a^2 + h^2}$.

4.6.2 Distance Distribution in the 0^{th} Tier

Given that the user distribution is based on TCP with a variance σ_u^2, the CCDF and PDF of the distance W_0 between u and GBS in the representive cluster are respectively, given by

$$\bar{F}_{W_o}(w) = \exp\left(-\frac{w^2}{2\sigma_u^2}\right) \qquad w \geq 0, \tag{4.26}$$

$$f_{W_o}(w) = \frac{w}{\sigma_u^2}\exp\left(-\frac{w^2}{2\sigma_u^2}\right) \quad w \geq 0. \tag{4.27}$$

4.6.3 Distance Distribution in the 1^{st} Tier

Recall that W_r^l is the serving distance in the 1^{st} tier i.e. the nearest distance from u to the LoS/NLoS GBS$_1$.

Lemma 4.6.1. *The CCDF and PDF of W_r^l, can be written as*

$$\bar{F}_{W_r^l}(r) = {Q_G^l}^{-1}\exp\left(-2\lambda_G\pi\int_0^r P_G^l(q)qdq\right), \tag{4.28}$$

$$f_{W_r^l}(r) = {Q_G^l}^{-1}2\lambda_G\pi r P_G^l(r)\exp\left(-2\lambda_G\pi\int_0^r P_G^l(q)qdq\right), \tag{4.29}$$

where $Q_G^l = 1 - e^{-2\lambda_G\pi\int_0^\infty p_G^l(q)qdq}$ is the probability that u is surrounded by at least one l GBS$_1$.

Proof: Given that at least one GBS$_1$ exists in $l \in \{LoS, NLoS\}$ state, $\bar{F}_{W_r^l}(r)$ can be defined as the probability that all GBSs in the 1^{st} tier are located at a distance greater than r.

$$\begin{aligned}
\bar{F}_{W_r^l}(r) &= \mathbb{P}(W_r^l > r \mid \exists \text{ at least one GBS}_1 \text{ is in } l \text{ link}) \\
&= \frac{\mathbb{P}(W_r^l > r, \text{ the link is } l)}{\mathbb{P}(\exists \text{ at least one GBS}_1 \text{ is in } l \text{ link})} \\
&= \frac{\mathbb{P}(\text{there is no GBS}_1 \text{ closer that } r\ )}{Q_G^l} \\
&\overset{(a)}{=} {Q_G^l}^{-1}\exp\left(-\int\int\lambda_G p_G^l(q)qdqd\theta\right) \\
&= {Q_G^l}^{-1}\exp\left(-2\lambda_G\pi\int_0^r p_G^l(q)qdq\right),
\end{aligned} \tag{4.30}$$

where (a) results from the null probability of the PPP [37], by integrating the area of the circle with radius r using polar coordinates. The PDF of W_r^l, can be simply computed by $f_{W_r^l}(r) = -\frac{d}{dr}\bar{F}_{W_r^l}(r)$ which completes the proof.

4.6.4 Conditional Serving Distance Distribution

Let denote by $\hat{X}_r^l$, $\hat{W}_0^l$ and $\hat{W}_r^l$ the conditional distances given that u is associated with a UBS, GBS$_0$ or GBS$_1$ in a LoS/NLoS link, respectively.

Lemma 4.6.2. *The conditional PDF of the distances $\hat{X}_r^l$, $\hat{W}_0^l$ and $\hat{W}_r^l$ are respectively expressed by*

$$f_{\hat{X}_r^l}(r) = \frac{N\frac{2r}{r_a^2}P_U^l(r)}{A_U^l}\left(\sum_v \int_{R_{U^l}^{U^v}(r)}^{x_u} \frac{2x}{r_a^2}P_U^v(x)dx\right)^{N-1} \sum_v Q_0^v \bar{F}_{W_o}\left(R_{U^l}^{G_0^v}(r)\right) \prod_v Q_G^v \bar{F}_{W_r^v}\left(R_{U^l}^{G_1^v}(r)\right), \tag{4.31}$$

$$f_{\hat{W}_0^l}(r) = \frac{f_{W_0}(r)P_G^l(r)}{A_{G_0}^l}\left(\sum_v \int_{R_{G_0^l}^{U^v}(r)}^{x_u} \frac{2x}{r_a^2}P_U^v(x)dx\right)^{N} \prod_v Q_G^v \bar{F}_{W_r^v}(r), \tag{4.32}$$

$$f_{\hat{W}_r^l}(r) = \frac{Q_G^l Q_G^b f_{W_r}^l(r)}{A_{G_1}^l}\left(\sum_v \int_{R_{G_1^l}^{U^v}(r)}^{x_u} \frac{2x}{r_a^2}P_U^v(x)dx\right)^{N} \bar{F}_{W_r^b}(r) \sum_v Q_0^v \bar{F}_{W_0}(r), \tag{4.33}$$

where $l, v, b \in \{LoS, NLoS\}$ and $l \neq b$.

Proof: The proof follows the same steps as in Lemma 3.6.2.

4.6.5 Conditional Interfering Distance Distribution

Let denote by $\mathcal{B}_{R_{tl}^{y^v}(r)}$ the event that the interfering BS $y \in \{U, G_0, G_1\}$ in $v \in \{LoS, NLoS\}$ link is located $R_{tl}^{y^v}(r)$ away from u and that the serving BS $t \in \{U, G_0, G_1\}$ in $l \in \{LoS, NLoS\}$ link is located at a distance r from u.

The conditional PDF of the interference distance Z_i and W_0 are given by

$$f_{Z_i}\left(z|\mathcal{B}_{R_{tl}^{U^v}(r)}\right) = \frac{f_{X_i}(z)P_U^v(z)}{\int_{R_{tl}^{U^v}(r)}^{x_u} f_{X_i}(z)P_U^v(z)dz}, \tag{4.34}$$

$$f_{W_0}\left(w_0|\mathcal{B}_{R_{tl}^{G_0^v}(r)}\right) = \frac{f_{W_0}(w_0)}{\bar{F}_{W_0}(R_{tl}^{G_0^v})}, \tag{4.35}$$

The proof follows the same steps as in Lemma 3.6.3.

4.7 Conclusion

In this chapter, we have proposed a new VHetNet framework model operating in mmWave bands under the assumption of a probabilistic LoS/NLoS propagation, and max-power association approach. The model consisted of multi-tier networks in which the GBSs are assisted by a finite number of UBSs in the context of hotspot scenarios and high-rise building environments. It was assumed that the UBSs are downlink MU-MIMO beamforming capable and that users are clustered around the GBSs following the TCP model. The buildings are modeled by a Boolean scheme of rectangles. We have developed formulas for LoS/NLoS probabilities, that take into

account the density, height, and area of blockages. Furthermore, we have extended our model to a MU-MIMO 3D beamforming model. Based on this, we derive the SINR expression and the relevant distance distributions for each tier. The subsequent chapter is dedicated to the analysis and evaluation of the performances of the two elaborated network models.

Chapter 5

Downlink Performance Analysis of UAV-assisted Cellular Networks

Contents

5.1 Introduction **75**
5.2 Downlink Performance Analysis of Single-Tier Aerial Networks **75**
5.2.1 Coverage Probability 75
5.2.2 UBSs Number Optimization 78
5.2.3 Network Spectral Efficiency 78
5.2.4 Simulation and Performance Evaluation 79
5.3 Downlink Performance Analysis of VHetNets under 3D Blockage Effects . . **85**
5.3.1 Coverage Probability 85
5.3.2 Coverage Probability With Shadowing 89
5.3.3 Coverage Probability With 3D Beamforming 90
5.3.4 Coverage Probability With Manageable Scenario 90
5.3.5 Area Spectral Efficiency 91
5.3.6 Simulation and Performance Evaluation 92
5.4 Conclusion **104**

5.1 Introduction

This chapter provides a detailed downlink performance analysis and evaluation for the proposed frameworks, based on the system models described in chapter 3 and chapter 4. First, we derive the analytical expressions for the association probability of a typical user at each tier based on the distance distribution and LoS/NLoS probabilities. Subsequently, we calculate Laplace transform of the aggregate interference to obtain the conditional coverage probabilities using the gamma approximation. From there, we derive the overall coverage probability and spectral efficiency analytical expressions. Finally, we evaluate and confirm the validity of these expressions through numerical and simulation results.

5.2 Downlink Performance Analysis of Single-Tier Aerial Networks

Recall that the aim of this study is to evaluate the downlink performance of mmWave aerial networks in an isolated region where traditional GBSs are unable to provide wireless connectivity. In this scenario, we analyze coverage probability and network spectral efficiency as performance metrics through the association probability to LoS and NLoS UBSs based on the greater received power.

5.2.1 Coverage Probability

We set a SINR threshold $\mathcal{T}$ above which coverage can be assumed. The overall coverage probability can be defined as

$$P_c(y_0) = \sum_l \mathbb{P}(SINR > \mathcal{T} | u \text{ is connected to } l \text{ UBS }) A_U^l(y_0),$$

$$P_c(y_0) = P_{c,U}^{LoS}(y_0) A_U^{LoS}(y_0) + P_{c,U}^{NLoS}(y_0) A_U^{NLoS}(y_0), \tag{5.1}$$

where $P_{c,U}^{LoS}(y_0)$ and $P_{c,U}^{NLoS}(y_0)$ are the conditional coverage probabilities and $A_U^{LoS}(y_0)$ and $A_U^{NLoS}(y_0)$ are the association probabilities given that the typical user is served by the UBS in LoS and NLoS states, respectively.

Association Probability

Using the PDF of the distances given in Chapter 3, section 3.6, the association probability with UBS being transmitting in a LoS link can be derived by Lemma 5.2.1.

Lemma 5.2.1. *The probability of the typical user being connected to LoS UBS is given by*

$$A_U^{LoS}(y_0) = N \int_h^{x_u} \left(\int_r^{x_u} f_{X_i}(x \mid y_0) P_U^{LoS}(x) dx + \int_{R_{LoS}^{NLoS}(r)}^{x_u} f_{X_i}(x \mid y_0) P_U^{NLoS}(x) dx \right)^{N-1} \times P_U^{LoS}(r) f_{X_i}(r \mid y_0) dr, \tag{5.2}$$

where $l, v \in \{LoS, NLoS\}$, $R_l^v(r) = \left(\frac{\varphi_l}{\varphi_v}\right)^{\frac{1}{\alpha_U^v}} r^{\frac{\alpha_U^l}{\alpha_U^v}}$ is the separation distance between u and the nearest UBS in the v state assuming that the serving UBS is in the l state. N implies the fact that there are N ways to choose the serving UBS from all UBSs.

Proof of Lemma 5.2.1:

Recall that the N transmitting UBSs in a single swarm are i.i.d. with arbitrary locations $\{A_i\}_{i=1:N}$ according to the BPP distribution, and $X_i \leq x_u$ is the distance between an arbitrary UBS A_i and the typical user. Therefore, there is only one serving UBS, which is the one that provides the strongest received power. Let $\mathcal{A}_{LoS}$ denotes the probability that the service UBS located at A_0 is in LoS connection with the user, the distance between the two being noted as r. A_U^{LoS} can be defined as [136]

$$\begin{aligned} A_U^{LoS} &= N \mathbb{E}\left[P_U^{LoS}(X_i) \mathcal{A}_{LoS} \right] \\ A_U^{LoS} &= N \int_h^{x_u} P_U^{LoS}(r) \mathcal{A}_{LoS} f_{X_i}(r) dr \end{aligned} \tag{5.3}$$

where $\mathcal{A}_{LoS}$ can be given as

$$\begin{aligned} \mathcal{A}_{LoS} &= \mathbb{P}\left(\max_{i=1:N} \left(P_U \varphi_{LoS}^{-1} X_i^{-\alpha_U^{LoS}} \cup P_U \varphi_{NLoS}^{-1} X_i^{-\alpha_U^{NLoS}} \right) \right) \\ \mathcal{A}_{LoS} &\overset{(a)}{=} \prod_{\substack{i'=1:N-1 \\ i' \neq i}} \mathbb{P}\left(P_U \varphi_{LoS}^{-1} X_i^{-\alpha_U^{LoS}} > P_U \varphi_{LoS}^{-1} X_{i'}^{-\alpha_U^{LoS}} \cup P_U \varphi_{LoS}^{-1} X_i^{-\alpha_U^{LoS}} > P_U \varphi_{NLoS}^{-1} X_{i'}^{-\alpha_U^{NLoS}} \right) \\ &= \prod_{\substack{i'=1:N-1 \\ i' \neq i}} \mathbb{P}\left(X_{i'} > X_i \right) + \mathbb{P}\left(X_{i'} > X_i^{\frac{\alpha_U^{LoS}}{\alpha_U^{NLoS}}} \right) \\ &= \prod_{\substack{i'=1:N-1 \\ i' \neq i}} \mathbb{P}\left(X_{i'} > r \right) + \mathbb{P}\left(X_{i'} > r^{\frac{\alpha_U^{LoS}}{\alpha_U^{NLoS}}} \right) \\ &\overset{(b)}{=} \left(\int_r^{x_u} P_U^{LoS}(x) f_{X_i}(x) dx + \int_{R_{LoS}^{NLoS}(r)}^{x_u} P_U^{NLoS}(y) f_{X_i}(x) dx \right)^{N-1}, \end{aligned} \tag{5.4}$$

where (a) follows from the event that the strongest UBS can be LoS or NLoS are mutually exclusive. (b) means that there is no UBS in NLoS located at a distance less than $R_{LoS}^{NLoS}(r)$. The proof is complete by substituting (5.4) into (5.3).

Corollary 5.2.1. *The probability of the typical user being connected to NLoS UBS can be written as*

$$A_U^{NLoS}(y_0) = 1 - A_U^{LoS}(y_0) \tag{5.5}$$

Lemma 5.2.1 demonstrates the need for an additional numerical integral fold to be included in the association probabilities to manage the LoS and NLoS characteristics of the channel propagation model. For a deterministic channel model, this is not necessary.

Conditional Coverage Probability

The coverage probability given that the typical user is connected to either LoS UBS or NLoS UBS is referred to as the conditional coverage probability. The calculation of the conditional coverage probability of the typical user is based on the conditional distribution of service and interference distance, which was previously calculated in Chapter 3 and the Laplace transform of the total interference. The latter is given in the following lemma.

Lemma 5.2.2. *The Laplace transform of the aggregate interference I conditioned on the serving UBS being at a distance r is given by*

$$\mathcal{L}_I(\delta, R_l^{LoS}(r), R_l^{NLoS}(r)) = \sum_v \left[\int_{R_l^v(r)}^{x_u} \left(\frac{m_U^v}{m_U^v + \delta P_U \Omega(\omega, \theta(z)) \varphi_v^{-1} z^{-\alpha_U^v}} \right)^{m_U^v} \frac{P_U^v(z) f_{X_i}(z \mid y_0) dz}{\sum_q \int_{R_l^q(r)}^{x_u} f_{X_i}(z \mid y_0) P_U^q(z) dz} \right]^{K-1}, \tag{5.6}$$

Proof: See Appendix A.

After we have obtained the Laplace transform of the interference power, we present the main theorem on the conditional coverage probability. Including the high-order derivative calculation that depends on the Nakagami-*m* parameter in the coverage probability expression may considerably increase the evaluation time. To address this issue, we use the gamma approximation instead of the exact function to simplify the expression and reduce evaluation time.

Theorem 5.2.1. *The conditional coverage probability of the typical user is defined as*

$$P_{c,U}^l(y_0) = \int_h^{x_u} \sum_{n=1}^{m_U^l} (-1)^{n+1} \binom{m_U^l}{n} e^{-\delta N_0} \mathcal{L}_I(\delta, R_l^{LoS}(r), R_l^{NLoS}(r)) f_{\hat{X}_r^l}(r \mid y_0) dr, \tag{5.7}$$

where $\delta = \frac{n\varepsilon_U^l m_U^l \mathcal{T} \varphi_l r^{\alpha_U^l}}{P_U \Omega(\omega, \theta(r))}$, $\varepsilon_U^l = \left(m_U^l!\right)^{\frac{1}{m_U^l}}$ and the binomial coefficient $\binom{a}{b} = \frac{a!}{b!(a-b)!}$.

Proof: See Appendix B.

Substituting (5.2), (5.5) and (5.7) into (5.1) gives the overall coverage probability $P_c(y_0)$.

$$P_c(y_0) = \sum_l \int_h^{x_u} \sum_{n=1}^{m_U^l} (-1)^{n+1} \binom{m_U^l}{n} e^{-\delta N_0} \mathcal{L}_I(\delta, r, R_l^v(r)) f_{\hat{X}_r^l}(r \mid y_0) dr N \int_h^{x_u} P_U^l(r) f_{X_i}(r \mid y_0)$$
$$\times \left(\int_r^{x_u} f_{X_i}(x \mid y_0) P_U^{LoS}(x) dx + \int_{R_{LoS}^{NLoS}(r)}^{X_u} f_{X_i}(x \mid y_0) P_U^{NLoS}(x) dx \right)^{N-1} dr, \tag{5.8}$$

5.2.2 UBSs Number Optimization

The overall coverage probability expression is a function of the total number of UBSs and the number of SA UBSs. An optimization problem is formulated to determine the optimal number of SA UBSs within the single swarm [136], with the coverage probability serving as the objective function, which can be formulated as

$$K_{opt} = \arg\max P_c(y_0) \tag{5.9}$$

5.2.3 Network Spectral Efficiency

Determining the number of simultaneously active links is crucial for computing the NSE. Firstly, it is important to note that we are examining a specific, isolated region with a low user density. Therefore, it is not necessary to activate all the UBSs, as in hotspot scenarios. We assume that the K UBSs are simultaneously serving K different ground users. The NSE is computed by scaling the spectral efficiency of a link by the number of active transmitters in the network, as given in the following Lemma.

Theorem 5.2.2. *The network spectral efficiency can be formulated as*

$$NSE(y_0) = K \log_2 (1 + \mathcal{T}) P_c(y_0) \quad \textit{Bits/s/Hz}, \tag{5.10}$$

Proof: We have K out of N UBSs that are transmitting simultaneously in the network. Subsequently, by applying Shannon's capacity we could determine the spectral efficiency of a fully reliable communication link, given by $\log_2(1+\mathcal{T})\mathbb{P}(SINR > \mathcal{T})$ where $\mathbb{P}(SINR > \mathcal{T})$ is the overall coverage probability. By scaling this result with the SA UBSs we obtain (5.10).

Table 5.1: 3D beamforming based UAV swarm networks simulation parameters.

Parameter	**Value**	**Parameter**	**Value**
r_a	500 m	m_U^{LoS}, m_U^{NLoS}	$2, 1$
P_U	5 W	θ_d	$6°$
y_0	200 m	SL	18 dB
c_1, c_2	11.95, 0.136	N_0	-90 dBm
α_U^{LoS}, α_U^{NLoS}	3, 3.5	$\mathcal{T}$	-5 dB
φ_{LoS}, φ_{NLoS}	1, 10	Monte Carlo runs	10^5 - 10^6 runs

5.2.4 Simulation and Performance Evaluation

In this subsection, we validate our findings and assess the accuracy of the proposed mathematical framework. We evaluate the performance as a function of the down tilt angle and the UBS altitude, and we determine the optimal number of SA UBSs in a given finite region. Specifically, we use the computational software Wolfram Mathematica 12 to evaluate the analytical expressions, while MATLAB 2015 is employed for Monte Carlo simulations. These computations are performed on PCs equipped with an Intel(R) Core(TM) i5-5200U CPU @ 2.20GHz processor and 8GB of RAM. The system parameters are listed in Table 5.1.

5.2.4.1 Model Validation

Before proceeding with the coverage probability analysis, we verified the accuracy of our analytical findings. We performed our simulations within a circular area B_r with radius $r_a = 500$m. To ensure precision, we aggregated the outcomes over 100,000 simulation iterations. All Monte Carlo simulations are represented by "black" circular markers, while curves of varying colors depict the mathematical frameworks [136]. Figure 5.1 illustrates the coverage probability plotted against the SINR threshold for varying numbers of SA UBSs K, while maintaining a fixed number of transmitting UBSs $(N = 8)$. Initially, it is evident that the simulation results exhibit complete congruence with the analytical results for various SINR thresholds, thereby affirming the accuracy of our analytical expressions. On the other hand, increasing the number of SA UBSs leads to an increase in interference received from UBSs operating within the same time-frequency band, consequently diminishing the coverage probability.

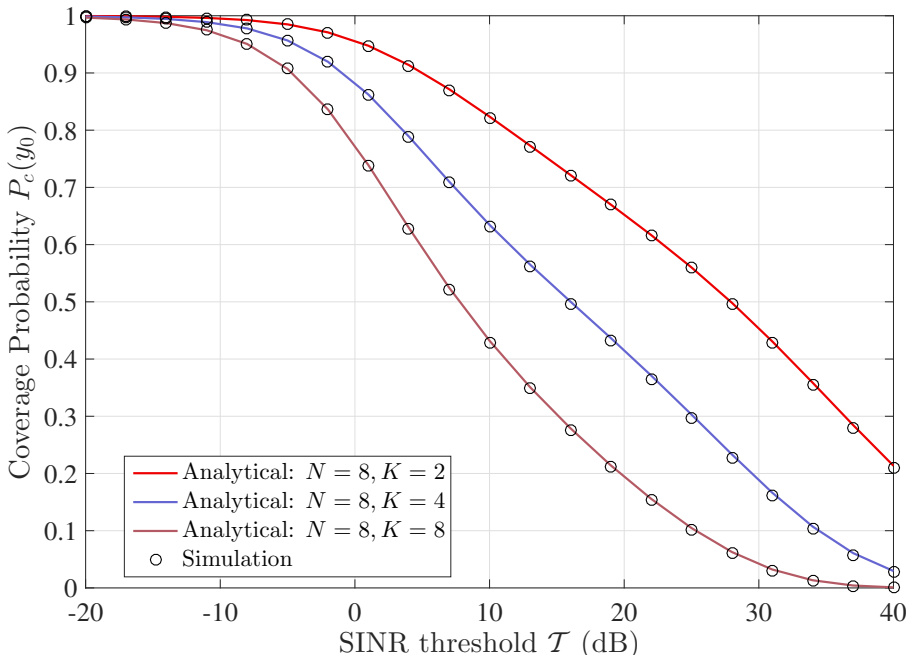

Figure 5.1: Coverage probability vs. SINR threshold with different number of SA UBSs ($h = 80$ m).

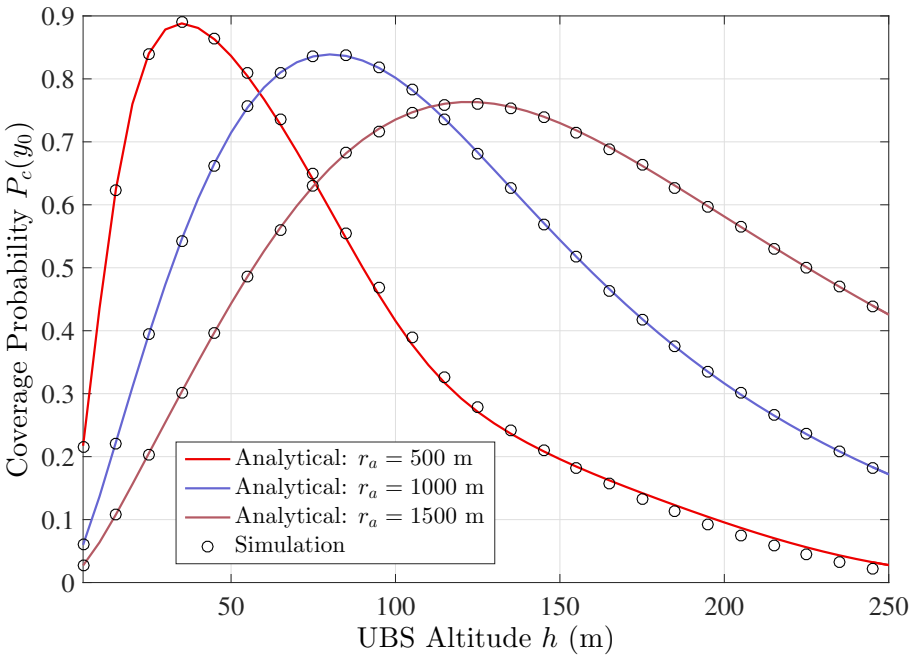

Figure 5.2: Coverage probability vs. UBS's altitude with different radius r_a.

5.2.4.2 Impact of h

In Figure 5.2, we depict the coverage probability as a function of UBS altitude across various surfaces of the finite target region, while maintaining a constant number of UBSs. It can be noticed that the altitude of the UBSs correlates with the area of the isolated region to achieve maximum coverage. In fact, enlarging the radius of the disks B_a and B_r exacerbates the coverage probability while requiring a high altitude. This is due to the expanded distribution area of

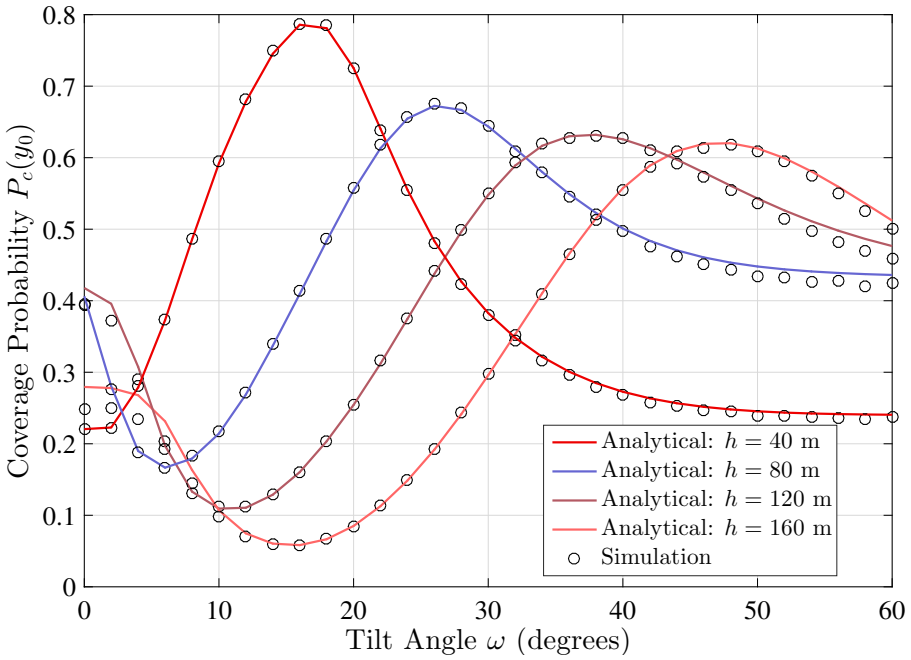

(a) Impact of tilt angle with UBS's altitude ($N = 8$, $K = 4$).

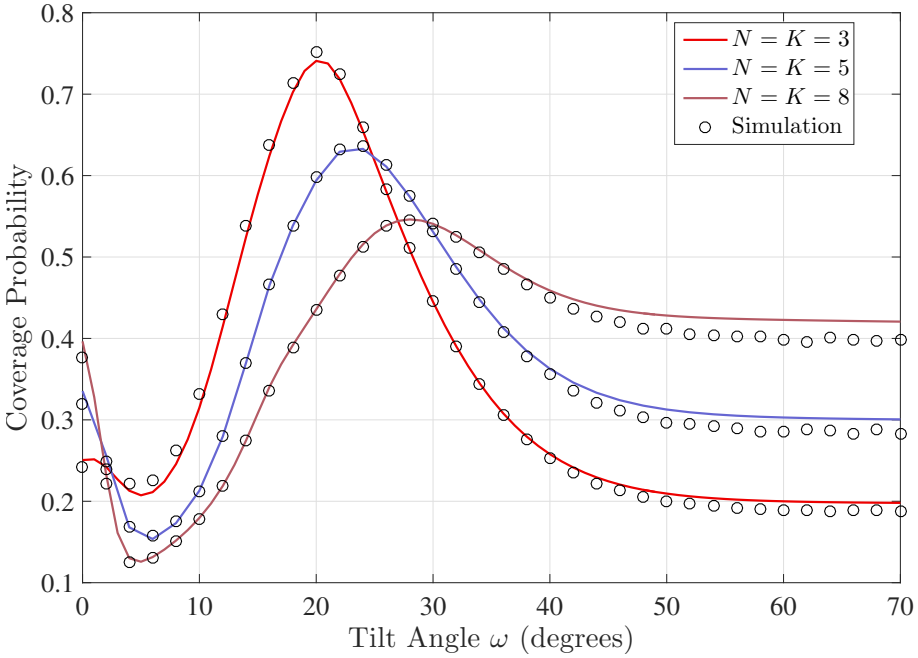

(b) Impact of tilt angle with the number of SA UBSs ($h = 80$ m).

Figure 5.3: Coverage probability vs. Tilt angle ω.

the UBS swarm, leading to a weakened signal reception at the user level. Consequently, raising the altitude of the UBSs becomes imperative to mitigate multipath phenomena and achieve improved LoS communications.

5.2.4.3 Impact of the Tilt Angle

Figure 5.3 delve into the examination of 3D beamforming's impact on the coverage probability, aiming to determine the optimal tilt angle for various parameters. In Figure 5.3(a), we analyze the coverage probability concerning tilt angle variation across different UBS altitudes. A general observation regarding this result is that the coverage probability decreases at low tilt angles, increases at moderate values, and then decreases again beyond the optimal threshold. This decrease is due to an excessively large tilt angle, where the UBS's antenna fails to extend its reach adequately. Moreover, we observe that varying UBS altitudes correspond to significantly different optimal tilt angles, exhibiting a direct relationship between them. Specifically, the optimal tilt angle increases as h increases ($\omega = 16°$ for $h = 40$ m and $\omega = 48°$ for $h = 160$ m). This highlights the importance of considering UBS altitude when adjusting the tilt angle for enhanced coverage probability.

Figure 5.3(b) illustrates the impact of using multiple SA UBSs on the optimal tilt angle. It can be observed that with a small number of SA UAVs, the coverage probability improves with a reduced tilt angle ranging from $\omega = 6°$ to $\omega = 20°$. This improvement stems from the reinforcement of the vertical antenna pattern gain and the expansion of the antenna coverage area associated with a smaller tilt angle. Additionally, owing to the restricted number of UBSs, the resultant interference experienced by the user remains minimal. However, in scenarios where the number of SA UBSs is elevated ($K = 8$), it becomes necessary to elevate the tilt angle (exceeding $\omega = 30°$) through 3D beamforming. This adjustment aims to mitigate the vertical antenna pattern gain received from interfering UBSs and enhance the SINR.

5.2.4.4 Impact of the User's Location

To discern the discrepancy in performance between the typical user located at the origin and an arbitrarily-positioned typical user, Figure 5.4 illustrates the coverage probability of the typical user within the finite circular zone B_r with radius $ra = 500$m, plotted against its distance from the origin with different UBS altitudes. As evident from Figure 5.4, the coverage probability is significantly affected by the user's location. As the user approaches the boundary of the circular zone, there is a marked decrease in coverage probability, primarily attributed to the diminished probability of the serving UBS being in LoS with the user. This phenomenon arises from the greater distance of many UBSs from the user compared to the fewer UBSs in close proximity, particularly evident when the UBS altitude is elevated. Consequently, this degrades the received signal power.

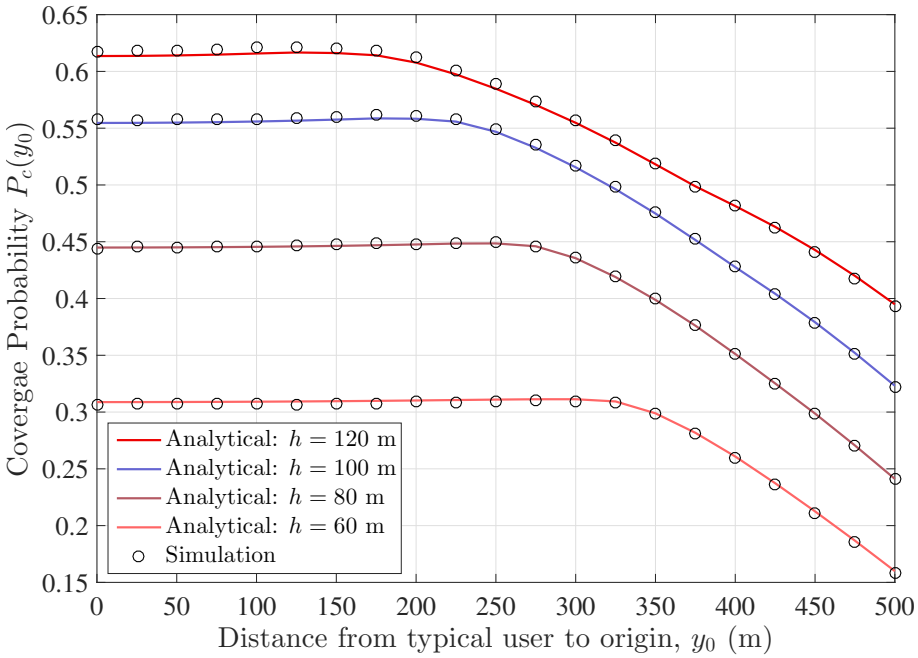

Figure 5.4: Coverage probability vs. the distance from the typical user to origin with different UBS altitudes.

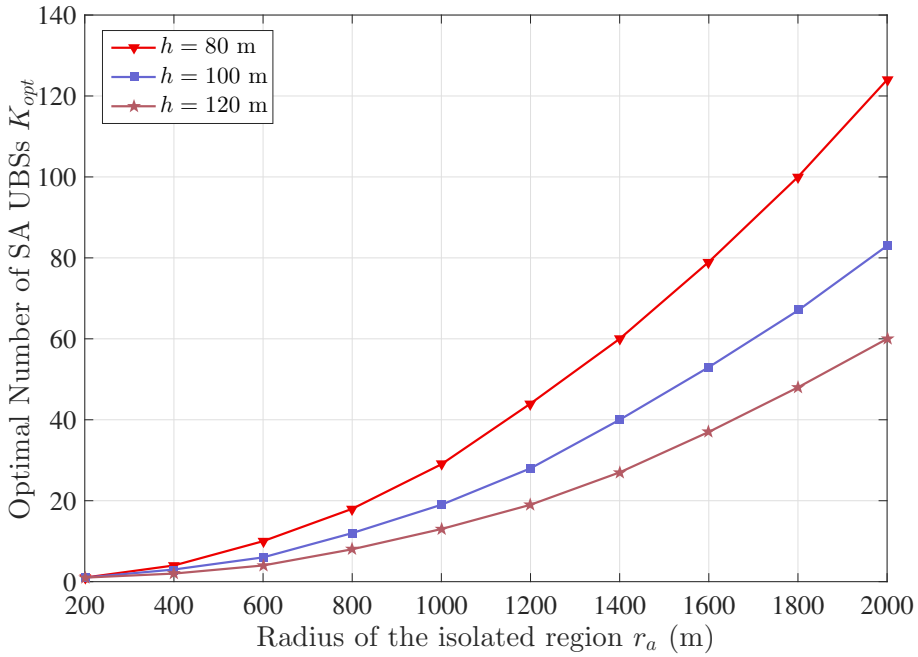

Figure 5.5: Optimal Number of SA UBSs K_{opt} vs. the isolated region radius ($\omega = 30°$).

5.2.4.5 SA UBSs Optimization

To determine the optimal number of SA UBSs that maximize the coverage probability, we conducted an analysis across various radii r_a of the disk B_r and B_a. For each radius, we extracted the optimal number of UBSs corresponding to different altitudes. The results obtained from this analysis are presented in Figure 5.5. It is evident that K_{opt} increases with r_a. In fact, the distribution of UBSs is contingent upon the surface of B_r. Consequently, the larger the

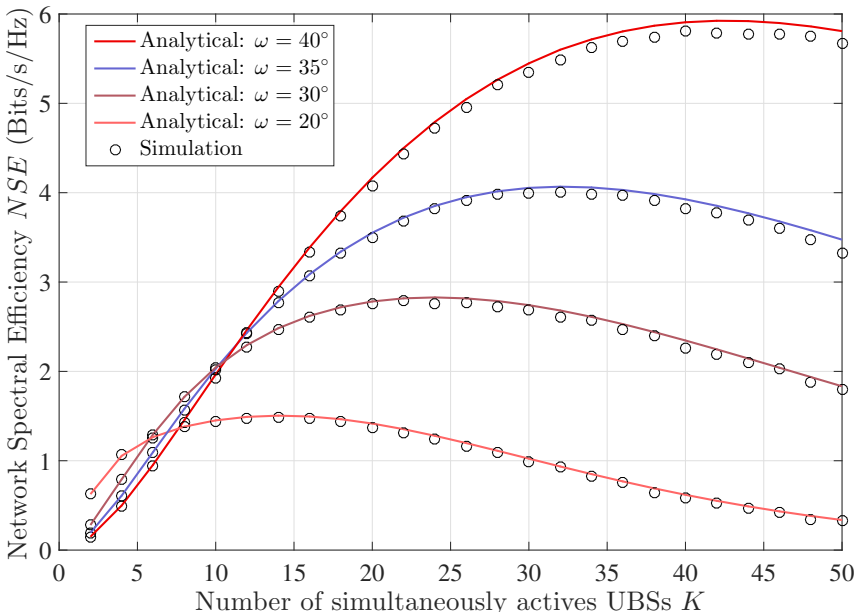

Figure 5.6: Network spectral efficiency vs. the number of SA UBSs K with different tilt angle ω ($h = 80$ m).

area to be covered, the greater the number of UBSs that must be deployed, as this increases the probability that the randomly located users will receive signal information in a LoS link and of high quality from one of the UBSs, guaranteeing comprehensive coverage. It is worth noting that deploying a large number of SA UBSs at low altitudes is recommended to mitigate interference caused by LoS SA UBSs. This approach strikes a trade-off between the optimal number of SA UBSs operating within the same frequency band and the resulting interference generated.

5.2.4.6 Impact of K and ω on the NSE

The performance of NSE was evaluated based on the number of SA UBSs with different tilt angle values, as shown in Figure 5.6. The figure indicates that NSE initially increases with an increase in the number of UBSs, but declines beyond the optimal value of K. This decline is due to the growing aggregate interference, which significantly reduces the received SINR. This highlights the trade-off between reusing spectrum resources and the resulting interference. Additionally, it was observed that the optimal number of SA UBSs increases with an increasing tilt angle value, resulting in improved NSE performance. For example, when $\omega = 40°$, $K = 42$, and when $\omega = 20°$, $K = 12$. This relationship exists because a larger tilt angle results in a smaller coverage area, which requires multiple UBSs to achieve maximum coverage and NSE. This finding supports the observations presented in Figure 5.3(b).

5.3 Downlink Performance Analysis of VHetNets under 3D Blockage Effects

In this section, we aim to evaluate the downlink performance of mmWave VHetNet with 3 tiers under 3D blockage effects caused by buildings for a typical user u assumed to be at the origin of the target area. In this study, we analyze coverage probability and area spectral efficiency as performance metrics through association probability based on the strongest long-term averaged received power in each tier.

5.3.1 Coverage Probability

We set a SINR threshold $\mathcal{T}$ above which coverage can be assumed. The overall coverage probability P_c of u is expressed as follows

$$P_c = \sum_t \sum_l \mathbb{P}\left(SINR > \mathcal{T} | u \text{ is connected to } t\text{BS in } l \text{ link }\right) A_t^l,$$

$$P_c = \sum_l P_{c,U}^l A_U^l + \sum_l P_{c,G_0}^l A_{G_0}^l + \sum_l P_{c,G_1}^l A_{G_1}^l, \tag{5.11}$$

where $l \in \{LoS, NLoS\}$, $P_{c,t}^l$ and A_t^l are the conditional coverage probability and the association probability of the typical user in each tier $t \in \{U, G_0, G_1\}$.

We will delve into the analysis of coverage probability both with and without shadowing effect. This decision stems from the anticipated high cost associated with incorporating shadowing into our coverage analysis model. This comprehensive approach will allow us to gain deeper insights into the combined effects of shadowing and blockages on the coverage probability.

In the following, we derive the mathematical expressions for the association probability and the conditional coverage probability in each tier and in the next subsection we determine the expression of the Area spectral efficiency.

Association Probability

Using the distribution functions for relevant distances in each tier derived in the previous Chapter 4, the analytical expressions for the association probability considering the probabilities of occurrence of the LoS and NLoS links, are given in the following Lemmas [155].

Lemma 5.3.1. *The probability that the typical user is associated with LoS/NLoS UBS can be expressed as*

$$A_U^l = N \int_h^{x_u} P_U^l(r) \left(\sum_v \int_{R_{U^l}^{U^v}(r)}^{x_u} \frac{2x}{r_a^2} P_U^v(x) dx \right)^{N-1} \sum_v Q_0^v \bar{F}_{W_o} \left(R_{U^l}^{G_0^v}(r) \right) \prod_v Q_G^v \bar{F}_{W_r^v} \left(R_{U^l}^{G_1^v}(r) \right) \times \frac{2r}{r_a^2} dr, \tag{5.12}$$

where $l, v \in \{LoS, NLoS\}$ $Q_0^v = \int_0^\infty P_G^v(q) f_{W_0}(q) dq$, is the probability of a v link in GBS_0.

Proof of Lemma 5.3.1:.

Let $\mathcal{A}_{UU}^l$, $\mathcal{A}_{UG_0}^l$, and $\mathcal{A}_{UG_1}^l$ be the probabilities that the l UBS A_i provides stronger received power than the power received from the other UBSs, GBS_0 and the nearest GBS in the 1^{st} tier, respectively. A_U^l can be written as [155]

$$A_U^l = N \mathbb{E} \left[P_U^l(r) \left[\mathcal{A}_{UU}^l \times \mathcal{A}_{UG_0}^l \times \mathcal{A}_{UG_1}^l \right] \right], \tag{5.13}$$

where

$$\begin{aligned} \mathcal{A}_{UU}^l &= \prod_{\substack{i'=1:N-1 \\ i' \neq i}} \mathbb{P} \left(P_U M g_U X_i^{-\alpha_U^l} > P_U M g_U X_{i'}^{-\alpha_U^l} \cup P_U M g_U X_i^{-\alpha_U^l} > P_U M g_U X_{i'}^{-\alpha_U^b} \right) \\ &= \left(\mathbb{P} \left(X_{i'} > r \right) + \mathbb{P} \left(X_{i'} > r^{\frac{\alpha_U^{LoS}}{\alpha_U^{NLoS}}} \right) \right)^{N-1} \\ &= \left(\sum_v \int_{R_{U^l}^{U^v}(r)}^{x_u} P_U^v(x) f_{X_i}(x) dx \right)^{N-1}, \end{aligned} \tag{5.14}$$

$$\begin{aligned} \mathcal{A}_{UG_0}^l &= \mathbb{P} \left(P_U M g_U X_i^{-\alpha_U^l} > P_G g_G W_0^{-\alpha_G^l} \cup P_U M g_U X_i^{-\alpha_U^l} > P_G g_G W_0^{-\alpha_G^b} \right) \\ &= \sum_v \mathbb{P} \left(W_0 > \left(\frac{P_G g_G}{P_U M g_U} \right)^{\frac{1}{\alpha_G^v}} r^{\frac{\alpha_U^l}{\alpha_G^v}} \right) \\ &= \sum_v Q_0^v \bar{F}_{W_o} \left(R_{U^l}^{G_0^v}(r) \right), \end{aligned} \tag{5.15}$$

$$\begin{aligned} \mathcal{A}_{UG_1}^l &= \prod_v \mathbb{P} \left(P_U M g_U X_i^{-\alpha_U^l} > P_G g_G W_r^{v - \alpha_G^v} \right) \\ &= \prod_v \mathbb{P} \left(W_r^v > \left(\frac{P_G g_G}{P_U M g_U} \right)^{\frac{1}{\alpha_G^v}} r^{\frac{\alpha_U^l}{\alpha_G^v}} \right) \\ &= \prod_v Q_G^v \bar{F}_{W_r^v} \left(R_{U^l}^{G_1^v}(r) \right), \end{aligned} \tag{5.16}$$

where $l, b, v \in \{LoS, NLoS\}$ and $l \neq b$.

Finally, substituting the expressions of (5.14), (5.15), and (5.16) into (5.13) and integrating over the disk region B_a yields to (5.12).

Lemma 5.3.2. *The probability that the typical user is associated with LoS/NLoS GBS in the* 0^{th} *tier is given by*

$$A^l_{G_0} = \int_0^{R^l_0} P^l_G(r) \left(\sum_v \int_{R^{U^v}_{G^l_0}(r)}^{x_u} \frac{2x}{r_a^2} P^v_U(x) dx \right)^N \prod_v Q^v_G \bar{F}_{W^v_r}(r)\, f_{W_0}(r) dr, \tag{5.17}$$

where $R^l_0 = \max\left(R^{G^l_0}_{U^v}(x_u)\right)$.

Proof: The proof follows the same steps as in Lemma 5.3.1.

Lemma 5.3.3. *The probability that the typical user is associated with LoS/NLoS GBS in the* 1^{st} *tier is given by*

$$A^l_{G_1} = Q^l_G \int_0^{R^l_1} \left(\sum_v \int_{R^{U^v}_{G^l_1}(r)}^{x_u} \frac{2x}{r_a^2} P^v_U(x) dx \right)^N Q^b_G \bar{F}_{W^b_r}(r) \sum_v Q^v_0 \bar{F}_{W_0}(r)\, f_{W^l_r}(r) dr, \tag{5.18}$$

where $R^l_1 = \max\left(R^{G^l_1}_{U^v}(x_u)\right)$.

Proof: The proof follows the same steps as in Lemma 5.3.1.

Conditional Coverage Probability

Before we start to derive the coverage probability conditioned on that u is associated with LoS/NLoS UBS, LoS/NLoS GBS in the 0^{th} tier and LoS/NLoS GBS in the 1^{st} tier, we need to derive first the Laplace transform of the aggregate interference providing from each tier, which are given in the following Lemmas.

Lemma 5.3.4. *The Laplace transform of the interference* I_{U_i} *from an arbitrary interfering UBS* A_i *is expressed as follows*

$$\mathcal{L}_{I_{U_i}}(\delta, R^{U^v}_{t^l}(r)) = \sum_v \int_{R^{U^v}_{t^l}(r)}^{x_u} \left(\frac{m^v_U}{m^v_U + \delta P_U G^U_I z^{-\alpha^v_U}} \right)^{m^v_U N_u} \frac{f_{X_i}(z) P^v_U(z) dz}{\sum_k \int_{R^{U^k}_{U^l}(r)}^{x_u} f_{X_i}(z) P^k_U(z) dz}, \tag{5.19}$$

where $l, v, k \in \{LoS, NLoS\}$, $t \in \{U, G_0, G_1\}$ and $G^U_I = \dfrac{g_U P_{g_U} + s_U P_{s_U}}{g_U}$.

Proof: The proof follows the same steps as in Lemma 5.2.2.

The Laplace transform of the aggregate interference I_U is expressed by [155]

$$\mathcal{L}_{I_U}(\delta, R^{U^v}_{t^l}(r)) = \begin{cases} \prod_{i=1}^{N-1} \mathcal{L}_{I_{U_i}}(\delta, R^{U^v}_{U^l}(r)), & \text{if } u \text{ is connected with UBS} \\ \prod_{i=1}^{N} \mathcal{L}_{I_{U_i}}(\delta, R^{U^v}_{G^l_0}(r)), & \text{if } u \text{ is connected with GBS}_0 \\ \prod_{i=1}^{N} \mathcal{L}_{I_{U_i}}(\delta, R^{U^v}_{G^l_1}(r)), & \text{if } u \text{ is connected with GBS}_1 \end{cases} \tag{5.20}$$

Lemma 5.3.5. *The Laplace transform of the interference I_{G_0} from the GBS$_0$ can be written as*

$$\mathcal{L}_{I_{G_0}}(\delta, R_{t^l}^{G_0^v}(r)) = \sum_v \int_{R_{t^l}^{G_0^v}}^{\infty} \left(\frac{m_G^v}{m_G^v + \delta P_G G_I^G w_0^{-\alpha_G^v}}\right)^{m_G^v} \frac{Q_0^v f_{W_0}(w_0) dw_0}{\sum_k Q_0^k \bar{F}_{W_0}(R_{t^l}^{G_0^k}(r))}, \tag{5.21}$$

where $G_I^G = \dfrac{g_G P_{g_G} + s_G P_{s_G}}{g_G}$.

Proof: The proof follows the same steps as in Lemma 5.2.2.

Lemma 5.3.6. *The Laplace transform of the interference I_{G_1} from the GBSs in the 1^{st} tier can be written as*

$$\mathcal{L}_{I_{G_1}}(\delta, R_{t^l}^{G_1^v}) = \prod_v \exp\left(- 2\lambda_G \pi \int_{R_{t^l}^{G_1^v}(r)}^{\infty} \left[1 \; - \left(\frac{m_G^v}{m_G^v + \delta P_G G_I^G w^{-\alpha_G^v}}\right)^{m_G^v} w P_G^v(w) dw\right]\right), \tag{5.22}$$

Proof: See Appendix E.

Using the gamma approximation and based on the conditional distance distribution and the Laplace transform of the interference, we provide in Theorem 5.3.1 the eventual expressions of the conditional coverage probability [155].

Theorem 5.3.1. *Applying the gamma approximation, the conditional coverage probabilities are given as follows*

$$P_{c,U}^l = \int_h^{x_u} \left[\sum_{n=1}^{m_U^l M} (-1)^{n+1} \binom{m_U^l M}{n} e^{-\delta N_0} \mathcal{L}_{I_U}(\delta, R_{U^l}^{U^v}(r)) \mathcal{L}_{I_{G_0}}(\delta, R_{U^l}^{G_0^v}(r))\right.$$
$$\left. \times \, \mathcal{L}_{I_{G_1}}(\delta, R_{U^l}^{G_1^v}(r))\right]_{\delta = \frac{n\varepsilon_U^l m_U^l \mathcal{T} r^{\alpha_U^l}}{P_U g_U}} f_{\hat{X}_r^l}(r) dr, \tag{5.23}$$

$$P_{c,G_0}^l = \int_0^{R_0^l} \left[\sum_{n=1}^{m_G^l} (-1)^{n+1} \binom{m_G^l}{n} e^{-\delta N_0} \mathcal{L}_{I_U}(\delta, R_{G_0^l}^{U^v}(r)) \mathcal{L}_{I_{G_1}}(\delta, r)\right]_{\delta = \frac{n\varepsilon_G^l m_G^l \mathcal{T} r^{\alpha_G^l}}{P_G g_G}} f_{\hat{W}_0^l}(r) dr, \tag{5.24}$$

$$P_{c,G_1}^l = \int_0^{R_1^l} \left[\sum_{n=1}^{m_G^l} (-1)^{n+1} \binom{m_G^l}{n} e^{-\delta N_0} \mathcal{L}_{I_U}(\delta, R_{G_1^l}^{U^v}(r)) \mathcal{L}_{I_{G_0}}(\delta, r) \mathcal{L}_{I_{G_1}}(\delta, r)\right]_{\delta = \frac{n\varepsilon_G^l m_G^l \mathcal{T} r^{\alpha_G^l}}{P_G g_G}}$$
$$\times \, f_{\hat{W}_r^l}(r) dr, \tag{5.25}$$

where $\varepsilon_U^l = \left((m_U^l M)!\right)^{\frac{1}{m_U^l M}}$, $\varepsilon_G^l = \left(m_G^l!\right)^{\frac{1}{m_G^l}}$.

Proof: The proof follows the same steps as in Theorem 5.2.1.

Now that we have obtained the expressions for both association and conditional coverage probabilities, we can obtain the overall coverage probability without shadowing, P_c, by substituting (5.12), (5.17), (5.18), (5.23), (5.24), (5.25) into (5.11).

5.3.2 Coverage Probability With Shadowing

In this subsection, we focus to derive the coverage probability including the effect of shadowing. To accomplish this, we require the PDF of the log-normal shadowing power S^l_{tdB}. Given that S^l_{tdB} follows a normal distribution with a mean of zero and a variance of $\sigma_{S^l_t}^2$, the expression for its PDF is as follows [155]

$$f_{S^l_t}(S) = \frac{1}{\sqrt{2\pi\sigma_{S^l_t}^2}} \exp\left(\frac{-S^2}{2\sigma_{S^l_t}^2}\right) \tag{5.26}$$

Theorem 5.3.2. *The conditional coverage probabilities with shadowing given that u is connected with UBS, GBS$_0$, and GBS$_1$ are given respectively by*

$$P_{c,U}^{Shad,l} = \int_h^{x_u} \left[\sum_{n=1}^{m_U^l M} (-1)^{n+1} \binom{m_U^l M}{n} \int_0^\infty e^{-\delta N_0} f_{S_U^l}(S) \mathcal{L}_{I_U}(\delta, R_{G_1^l}^{U^v}(r)) \mathcal{L}_{I_{G_0}}(\delta, r) \right.$$

$$\left. \times \mathcal{L}_{I_{G_1}}(\delta, r) dS \right]_{\delta = \frac{n\varepsilon_U^l m_U^l \mathcal{T} r^{\alpha_U^l}}{P_U g_U} 10^{\frac{S}{10}}} f_{\hat{X}_r^l}(r) dr, \tag{5.27}$$

$$P_{c,G_0}^{Shad,l} = \int_0^{R_0^l} \left[\sum_{n=1}^{m_G^l} (-1)^{n+1} \binom{m_G^l}{n} \int_0^\infty e^{-\delta N_0} f_{S_G^l}(S) \mathcal{L}_{I_U}(\delta, R_{G_0^l}^{U^v}(r)) \right.$$

$$\left. \times \mathcal{L}_{I_{G_1}}(\delta, r) dS \right]_{\delta = \frac{n\varepsilon_G^l m_G^l \mathcal{T} r^{\alpha_G^l}}{P_G g_G} 10^{\frac{S}{10}}} f_{\hat{W}_0^l}(r) dr, \tag{5.28}$$

$$P_{c,G_1}^{Shad,l} = \int_0^{R_1^l} \left[\sum_{n=1}^{m_G^l} (-1)^{n+1} \binom{m_G^l}{n} \int_0^\infty e^{-\delta N_0} f_{S_U^l}(S) \mathcal{L}_{I_U}(\delta, R_{G_1^l}^{U^v}(r)) \mathcal{L}_{I_{G_0}}(\delta, r) \right.$$

$$\left. \times \mathcal{L}_{I_{G_1}}(\delta, r) dS \right]_{\delta = \frac{n\varepsilon_G^l m_G^l \mathcal{T} r^{\alpha_G^l}}{P_G g_G} 10^{\frac{S}{10}}} f_{\hat{W}_r^l}(r) dr, \tag{5.29}$$

Proof: The proof follows the same steps as in Theorem 5.2.1.

The expression of the overall coverage probability with shadowing denoted by P_c^{Shad} can be written as

$$P_c^{Shad} = \sum_l P_{c,U}^{Shad,l} A_U^l + \sum_l P_{c,G_0}^{Shad,l} A_{G_0}^l + \sum_l P_{c,G_1}^{Shad,l} A_{G_1}^l, \tag{5.30}$$

5.3.3 Coverage Probability With 3D Beamforming

The implementation of 3D beamforming is constrained to the UBS tier. Consequently, the sole modification to the coverage probability formula derived in (5.11) is the conditional coverage probability, which accounts for the typical user being connected to the UBS tier. By employing the identical methodology as outlined in Theorem 5.3.1, the conditional coverage probability with MU-MIMO 3D beamforming, denoted by $P_{c,U}^{3DBeam,l}$ can be expressed as follows

$$P_{c,U}^{3DBeam,l} = \int_h^{x_u} \left[\sum_{n=1}^{m_U^l M} (-1)^{n+1} \binom{m_U^l M}{n} e^{-\delta N_0} \mathcal{L}_{I_U}\left(\delta, R_{U^l}^{U^v}(r)\right) \mathcal{L}_{I_{G_0}}\left(\delta, R_{U^l}^{G_0^v}(r)\right) \right.$$
$$\left. \times \mathcal{L}_{I_{G_1}}\left(\delta, R_{U^l}^{G_1^v}(r)\right) \right]_{\delta = \frac{n\varepsilon_U^l m_U^l \mathcal{T} r^{\alpha_U^l}}{P_U g_U \Omega\left(\omega,\theta\left(r^{\alpha_U^l}\right)\right)}} f_{\hat{X}_r^l}(r) dr, \tag{5.31}$$

The expression of the overall coverage probability with 3D beamforming model and without shadowing denoted by P_c^{3DBeam} can be written as

$$P_c^{3DBeam} = \sum_l P_{c,U}^{3DBeam,l} A_U^l + \sum_l P_{c,G_0}^l A_{G_0}^l + \sum_l P_{c,G_1}^l A_{G_1}^l, \tag{5.32}$$

5.3.4 Coverage Probability With Manageable Scenario

Closed-form expressions provide computational efficiency and precise mathematical representation of the system under study. They enable researchers to accurately analyze the system's behavior without relying on numerical simulations. They serve as a foundation for theoretical investigations, allowing researchers to examine more intricate scenarios or expand the analysis to various network configurations.

To identify a mathematically manageable scenario we derive closed-form expressions for coverage probability, we streamline our model by making the assumption that the typical user u is connected to GBS_0 the GBS in the cluster center of the representative cluster and experiences aggregate interference solely from GBS_1, while excluding consideration of the UBS tier.

Special case: We assume a Rayleigh fading $(m_G = 1)$, $(\alpha_G = 4)$.

Using a change of variables $\mu = \frac{w_0}{r\mathcal{T}^{1/\alpha_G}}$. The Laplace transform of the interference can be written as

$$\mathcal{L}_{I_{G_1}}(r) = \exp\left(-\pi r^2 \lambda_G \mathcal{T}^{\frac{2}{\alpha_G}} \int_{T^{-\frac{2}{\alpha_G}}}^{\infty} \frac{1}{1+\mu^{\frac{\alpha_G}{2}}} d\mu\right), \tag{5.33}$$

when $\alpha_G = 4$, the Laplace transform become a closed-form expression given by

$$\mathcal{L}_{I_{G_1}}^{CF}(r) = \exp\left(-\pi r^2 \lambda_G \sqrt{\mathcal{T}}\left(\frac{\pi}{2} - \tan^{-1}\left(\frac{1}{\sqrt{\mathcal{T}}}\right)\right)\right), \tag{5.34}$$

Based on the definition of the coverage probability and the exponential distribution of the Rayleigh fading, the coverage probability of a typical user can be written as

$$P_c^* = \int_0^\infty \mathcal{L}_{I_{G_1}}^{CF}(r) \exp\left(\frac{-\mathcal{T} N_0 r^4}{P_G g_G}\right) f_{W_0}(r) dr, \tag{5.35}$$

Using a change of variables $r^2 \to d$ the coverage probability expression allows a form that can be evaluated according to

$$\int_0^\infty \exp\left(-bd\right) \exp\left(-cd^2\right) dd = \sqrt{\frac{\pi}{c}} \exp\left(\frac{b^2}{4c}\right) Q\left(\frac{b}{\sqrt{2c}}\right), \tag{5.36}$$

Therefore the closed-form expression of the coverage probability, denoted by, P_c^{CF} is expressed as

$$P_c^{CF} = \frac{\sqrt{\pi T}}{2\sigma_u^2} \exp\left(\frac{\left(\pi\lambda_G L + \frac{1}{2\sigma_u^2}\right)^2 T}{4}\right) Q\left(\frac{\left(\pi\lambda_G L + \frac{1}{2\sigma_u^2}\right)\sqrt{T}}{\sqrt{2}}\right), \tag{5.37}$$

where $Q(.)$ is the standard Gaussian tail probability. $L = \sqrt{\mathcal{T}}\left(\frac{\pi}{2} - \tan^{-1}\left(\frac{1}{\sqrt{\mathcal{T}}}\right)\right)$ and $T = \frac{P_G g_G}{\mathcal{T} N_0}$. This expression is quite simple, where only a simple $Q(.)$ value needs to be calculated.

In the next subsection, we compute the area spectral efficiency based on the overall coverage probability in the absence of shadowing.

5.3.5 Area Spectral Efficiency

In this scenario, it's pertinent to reiterate that we're examining a densely populated hotspot area. Consequently, we make the assumption that all GBSs and a total of N UBSs are concurrently operational within the surveyed region.

Theorem 5.3.3. *The expression of ASE can be formulated as follows*

$$ASE = \left(\frac{N N_u}{\pi r_a^2} \sum_l P_{c,l}^U A_U^l + \lambda_G \left(\sum_l P_{c,l}^{G_0} A_{G_0}^l + \sum_l P_{c,l}^{G_1} A_{G_1}^l\right)\right) \log_2(1+\mathcal{T}), \tag{5.38}$$

Proof: The average density of active UBSs is calculated by dividing the number of UBSs, N, by the disk area, B_a. Since UBSs have MIMO antennas that serve N_u users concurrently, the result is multiplied by N_u. The ASE may be expressed as $\log_2(1+\mathcal{T})P_c$, as derived by Shannon's theorem. Finally, (5.38) is obtained by scaling the formula $\log_2(1+\mathcal{T})P_c$ with the densities of the GBSs and UBSs.

Table 5.2: VHetNets with a 3D blockage model simulation parameters.

Parameter	**Value**
λ_G	$\frac{2}{\pi 500^2}$
N	15
r_a	1 Km
P_G	20 W
P_U	5 W
N_a	4
N_u	2
α_G^{LoS}, α_G^{NLoS}, α_U^{LoS}, α_U^{NLoS}	$2.5, 4, 2.5, 4$
m_G^{LoS}, m_G^{NLoS}, m_U^{LoS}, m_U^{NLoS}	$2, 1, 2, 1$
b_1, b_2, b_1', b_2' (urban environment)	10.39, 0.05, 29.06, 0.03
$\mathbb{E}[W_B]$, $\mathbb{E}[L_B]$	15 m, 20 m
g_t, s_t, θ_t,	40 dBm, 20 dBm, $\pi/6$
θ_d, SSL	6°, 18 dB
N_0	-90 dBm
$\mathcal{T}$	15 dB
Monte Carlo Runs	10^5

5.3.6 Simulation and Performance Evaluation

In this subsection, we assess the analytical expressions developed in this study and confirm the analytical findings using Monte Carlo simulations. The aim is to analyze the influence of 3D blockage effects on VHetNet performance under the assumption of a hotspot scenario. Furtheremore, we investigate the advantage of adopting MU-MIMO beamforming system in the UBS tier. The parameters used in this analysis are listed in Table 5.2.

5.3.6.1 Impact of σ_u on the Association Probability

The total association probability to each tier is given by $A_t = A_t^{LoS} + A_t^{NLoS}$. Figure 5.7(a) illustrates the effect of the standard deviation of user distribution σ_u on the association probability. It is evident that with a small σ_u, the serving BS remains GBS_0. This occurs because the typical user is near to the cluster center in the representive cluster, thereby reducing the probability of encountering a blocked link or NLoS link. However, with an increase in σ_u, denoting a broader dispersion of users around the cluster center, the association probability with GBS_0

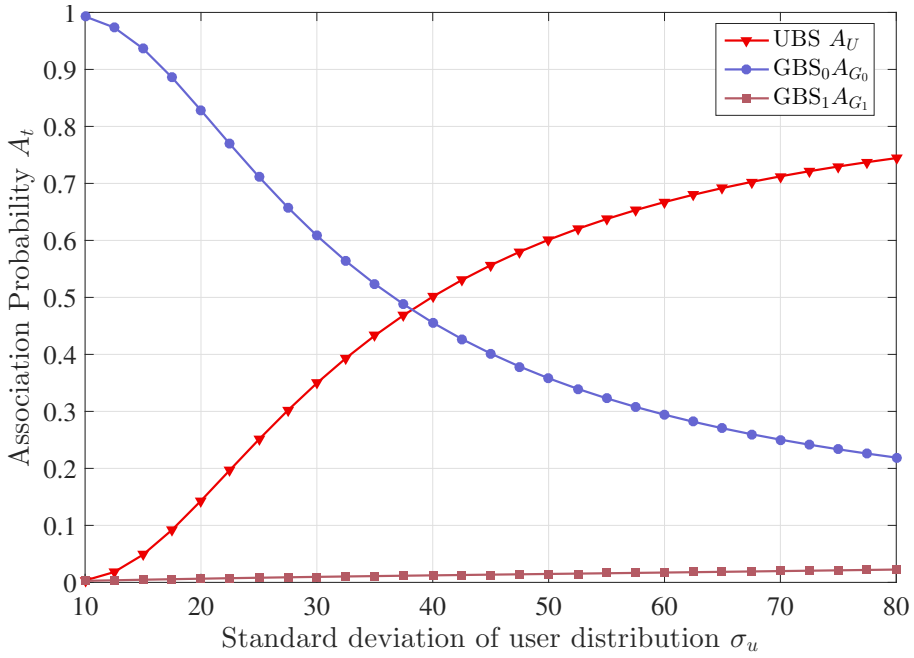

(a) Impact of standard deviation σ_u ($h = 250$ m, $p = 0.4$).

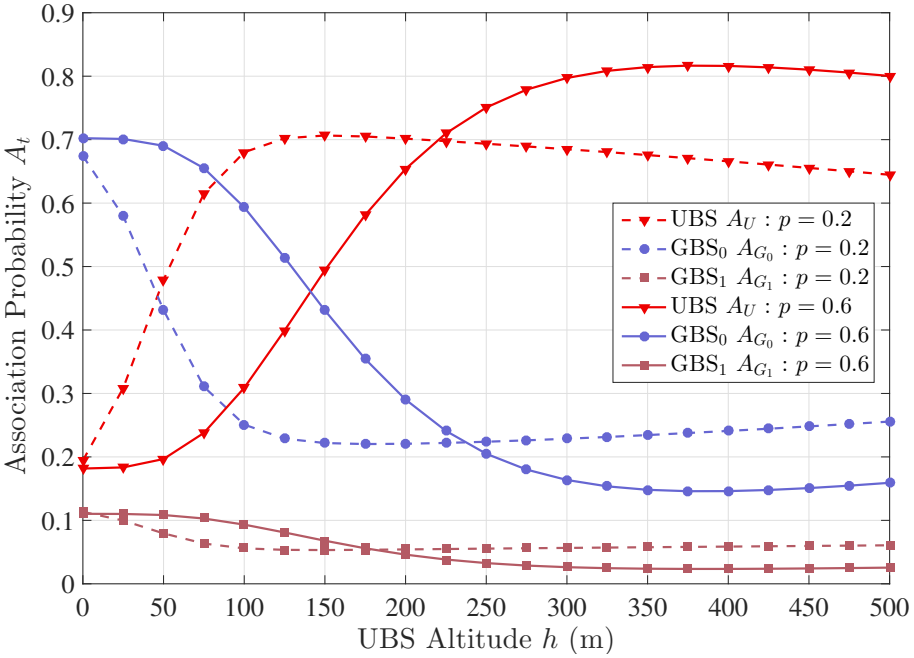

(b) Impact of UBS altitude for different p.

Figure 5.7: Association probability vs. user distribution's standard deviation and UBS altitude h ($\overline{H}_B = 20$ m).

deteriorates while the association probability with UBSs increases. This is due to the increased distance between u and GBS$_0$, resulting in increased path loss and subsequently, a degradation of the received signal power from GBS$_0$. Consequently, the received power provided by UBSs is amplified. Moreover, the association probability to GBS$_1$, exhibits a slight increase, indicating that the typical user is more inclined to be associated with UBSs rather than GBS$_1$.

5.3.6.2 Impact of h and p on the Association Probability

We examine the impact of UBS altitude h on user association, for varying city blockage densities p in Figure 5.7(b). First, for the association probability with the UBS tier, in suburban areas ($p = 0.2$), the association probability increases rapidly as altitude increases. This arises from the ability to establish LoS connections with the typical user at low altitudes. However, the probability of maintaining LoS begins to decrease beyond an altitude of 150 m. In dense urban areas with multiple buildings ($p = 0.6$), the association probability increases gradually and starts to decrease at altitudes over 400 m. It can be inferred that the optimal UBS altitude can be affected by the environmental conditions. The association probability with the 0^{th} tier and the 1^{st} tier decreases as long as the UBS does not exceed its optimal altitude. Beyond this altitude, the A2G channel weakens due to the significant distance between the UBS and the user. As a result, the association probability with GBS_0 and GBS_1 begins to increase. Nevertheless, connecting to GBS_0 remains more favorable then GBS_1 as it is closer to the typical user. This finding concludes that in a dense city, the probability of association with the UBS level remains the highest, which may make UBSs an asset in tackling the problem of 3D blockages.

5.3.6.3 Model Validation

We validate our analytical expressions for the coverage probability as a function of the SINR threshold under different main lobe gain g_t, main lobe beamwidth θ_t and a fixed side lobe gain $s_t = 20$ dBm in Figure 5.8(a). We performed our Monte Carlo simulations in a circular target area B_g with radius $r_a = 1$ Km, concentric to a large circular simulation area with radius 10 Km [155]. To guarantee result accuracy, the simulation results are averaged over $100,000$ independent drops. Monte Carlo simulations are represented by "black" circular markers, while curves depict the mathematical frameworks. It is observed in Figure 5.8(a) that the simulation results exactly match the analytical curves, confirming the validity of our proposed framework and derivation. The use of beamforming significantly enhances the coverage probability. By choosing a larger main lobe gain and a narrower main lobe beamwidth, the coverage probability can be further enhanced.

5.3.6.4 Model Validation under Fixed/Random h

The coverage probability versus the SINR threshold for various number of UBSs with $\sigma_u = 30$ is illustrated in Figure 5.8(b). The simulation findings using the 2D BPP at a fixed altitude of $h = 100$ m represented by "black" circular markers precisely match the analytical curves for various numbers of UBSs and under different SINR threshold. The research may be extended

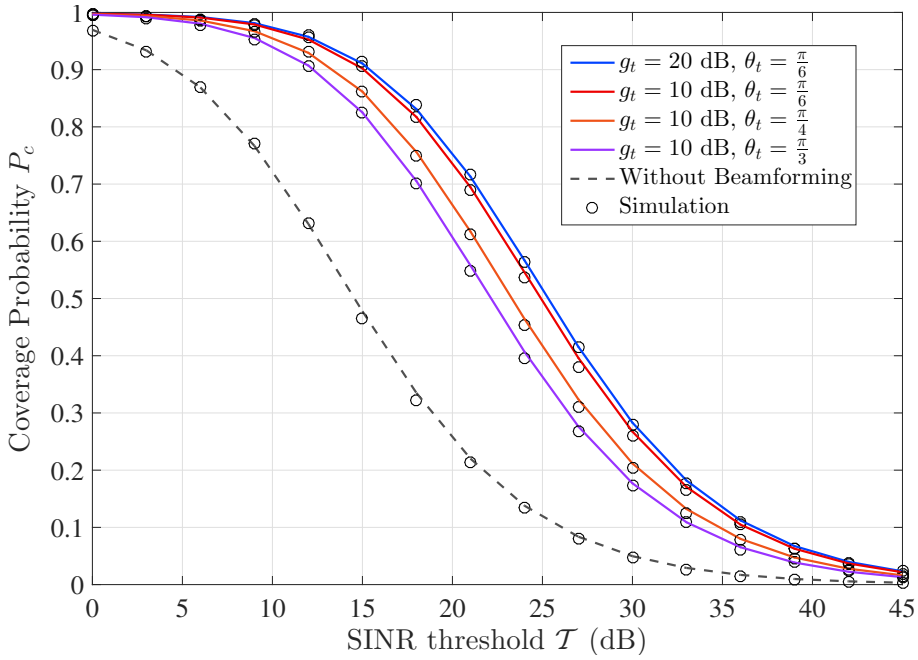

(a) Accuracy under directional beamforming ($\sigma_u = 30$, $h = 100$ m).

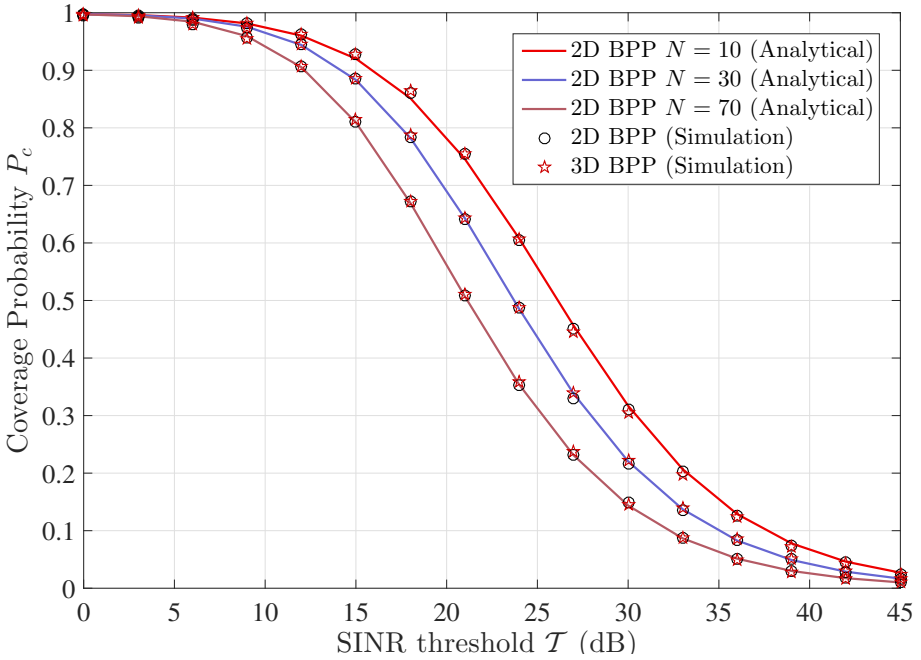

(b) Accuracy under varying UBS altitude ($\sigma_u = 30$).

Figure 5.8: Coverage probability without shadowing vs. SINR threshold $\mathcal{T}$ (dB) ($\overline{H}_B = 30$ m).

to include UBS networks at varying altitudes using 3D BPP, but this would result in more complex analytical expression derivations. To illustrate the accuracy of our approximation, the Monte Carlo simulations were used to compare 2D BPP with 3D BPP as it is not possible to acquire analytical findings for 3D BPP. We assume that h ranges between $h_{max} = 200$ m and $h_{min} = 100$ m for 3D BPP and mantain $h = \dfrac{h_{min} + h_{max}}{2}$ i.e., $h = 150$ m for 2D BPP. The

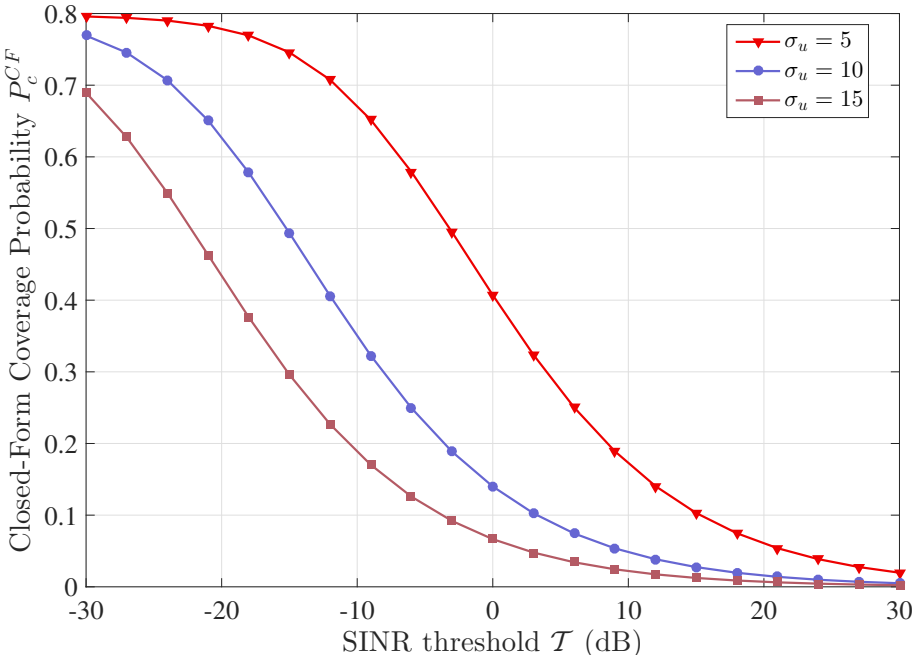

Figure 5.9: Coverage probability vs. SINR threshold with manageable scenario ($\alpha = 4$, Rayleigh fading).

simulations results with 3D BPP are represented by "red" pentagram markers. It is clear from Figure 5.8(b) that the results with fixed altitude closely match the results with varying atitude. As a result, for tractable analysis a fixed altitude can be assumed for all the UBSs. Figure 5.8(b) makes it evident that as the number of UBSs rises, the coverage probability declines because the user experiences more interference, which lowers the received SINR.

Figure 5.9 illustrates the closed-form expression for coverage probability with exponential interference (Rayleigh fading) where GBS_0 is the serving BS under different user distribution's standard deviation σ_u. It is evident that a higher σ_u, which indicates that the user is moving away from GBS_0, results in a lower coverage probability. This is due to the large path loss as the user gets farther away from GBS_0, which lowers the SINR.

5.3.6.5 Impact of h on the Coverage Probability

In this part, we investigate the effect of UBS altitude on coverage probability under high and small city blockage densities. In Figure 5.10(a), we plotted the coverage probability vs. h at various SINR thresholds. As can be shown, increasing the UBS altitude initially improves the coverage probability. However, at a specific altitude, the coverage probability starts to decrease, indicating the existence of an optimal h that maximizes the coverage probability. Increasing the altitude above the optimal level increases the propagation loss of the received signal. This occurs because, at peak coverage probability, most UBSs are already transmitting in a LoS connection with users. On the other hand, the optimal h is greater in the ultra-dense

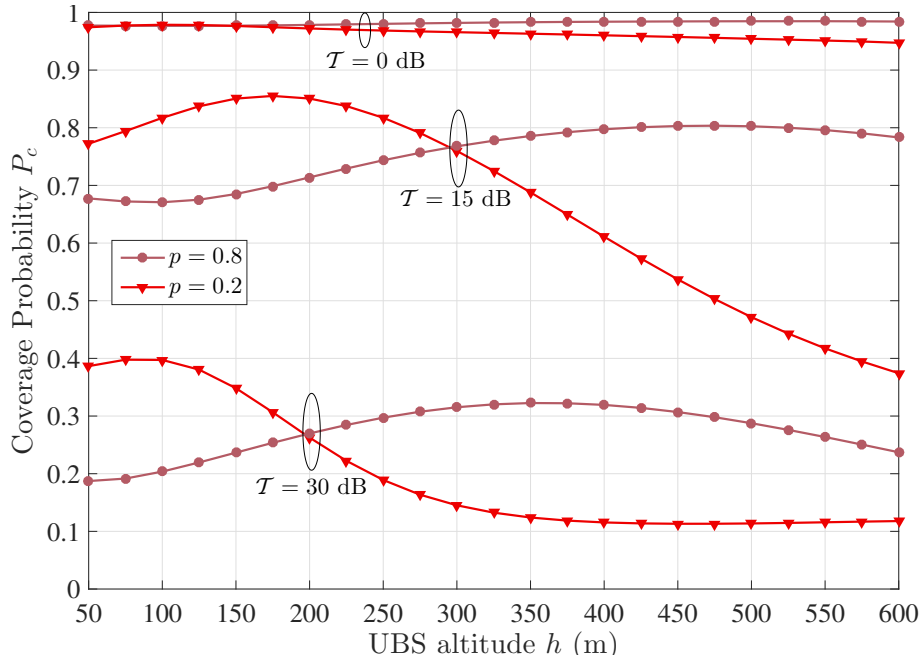

(a) Impact of UBS altitude for different p ($\overline{H}_B = 30$ m).

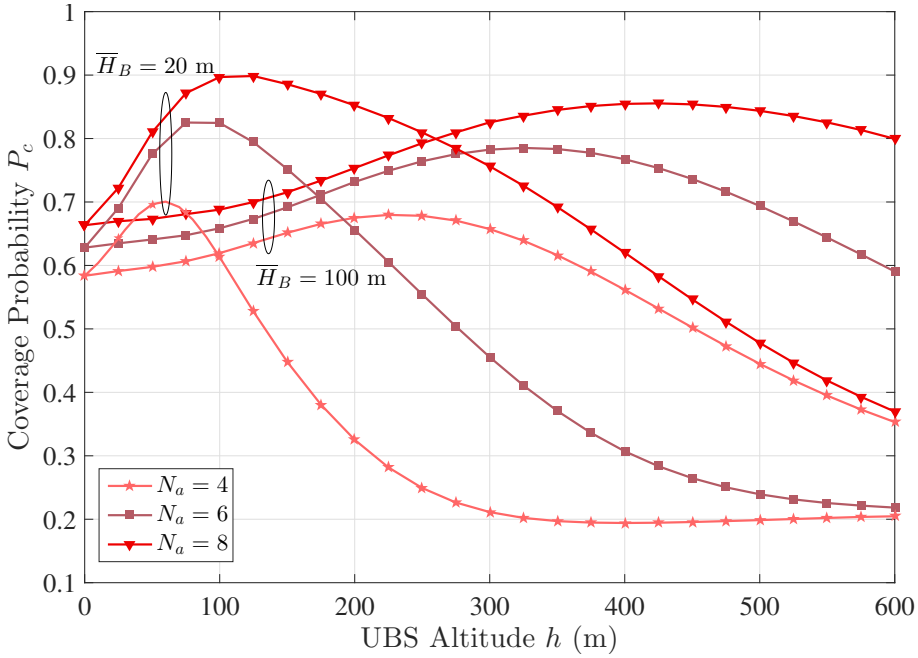

(b) Impact of UBS altitude for different number of antennas ($p = 0.2$).

Figure 5.10: Coverage probability vs UBS altitude.

city ($p = 0.8$) than it is in the suburban city ($p = 0.2$) to ensure LoS connectivity and prevent blocked connections. Furthermore, it is asserted that the optimal h varies based on the SINR threshold.

The coverage probability as a function of h, under different building height and transmit antenna number N_a, is displayed in Figure 5.10(b). The optimal h is also influenced by the height

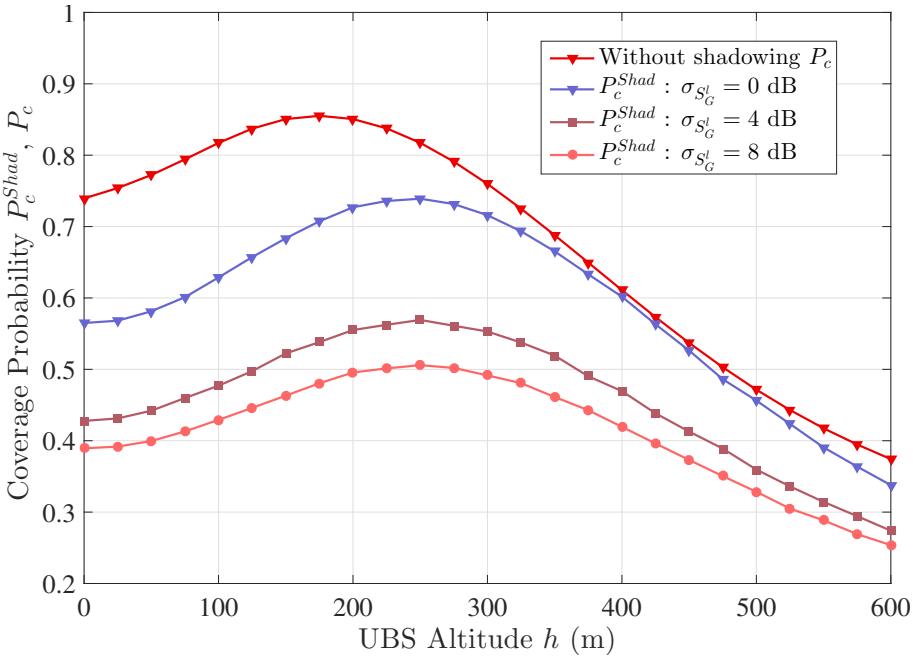

Figure 5.11: Coverage probability with/without shadowing vs UBS altitude h for different variance of the shadow power σ_G^l ($\bar{H}_B = 30$ m).

of the buildings. UBS must be sufficiently higher than the buildings to maximize coverage. For example, the optimal h for $N_a = 4$ with low building height ($\overline{H}_B = 20$ m) stays low at around 52 m, but rises to 225 m with tall buildings ($\overline{H}_B = 100$ m). Furthermore, taller buildings increase the probability of blocked connections, which slightly reduces coverage. It is important to note that increasing N_a increases the optimal h and significantly improves the coverage probability. This is because MU-MIMO system boosts the received signal power and increases the LoS probability.

5.3.6.6 Correlation between Shadowing, h and N

Our model shows that the variance of shadow power in the UBS tier is dependent on the elevation angle between the typical user and the UBS. To examine the shadowing effect, we plotted the coverage probability with and without shadowing as a function of h in Figure 5.11, while varying the variance of the shadow power in the GBS tier σ_G^l. Note that when $\sigma_G^l = 0$ dB, the GBS shadow is neglected. We can see that increasing σ_G^l leads to a decrease in the coverage probability P_c^{Shad}, as the user's received power decreases, resulting in a lower received SINR. At high UBS altitudes and when $\sigma_G^l = 0$, the coverage probability is nearly the same with or without shadowing. This is because the path loss has a much greater effect than shadowing.

Figure 5.12, illustrates the correlation between shadowing, h, and the number of assisting UBSs N, where $p = 0.4$ and $H_B = 30$ m. Clearly, the coverage probability P_c^{Shad} and P_c increases

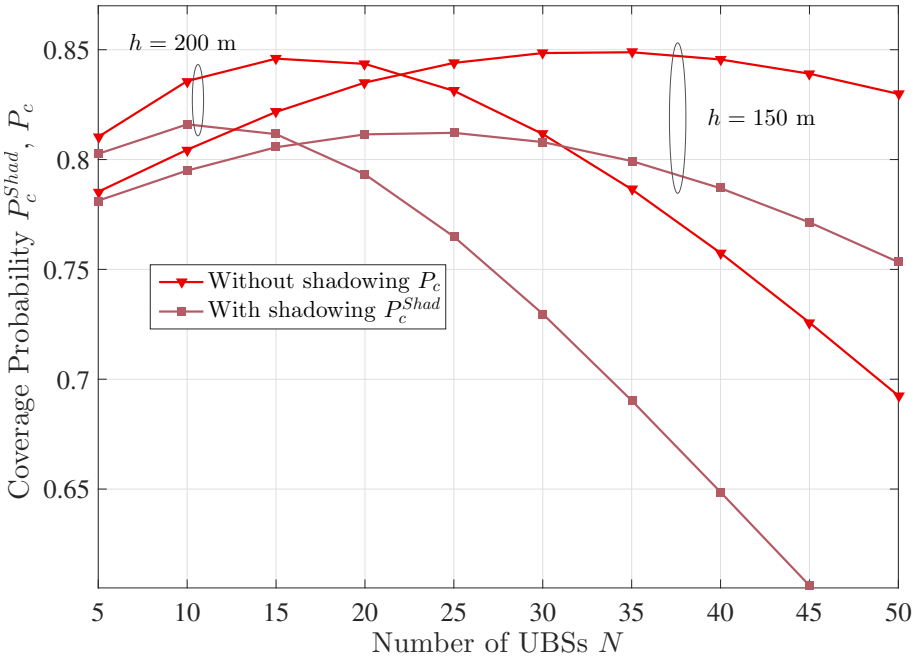

Figure 5.12: Coverage probability with/without shadowing vs assisting UBS number N with different h.

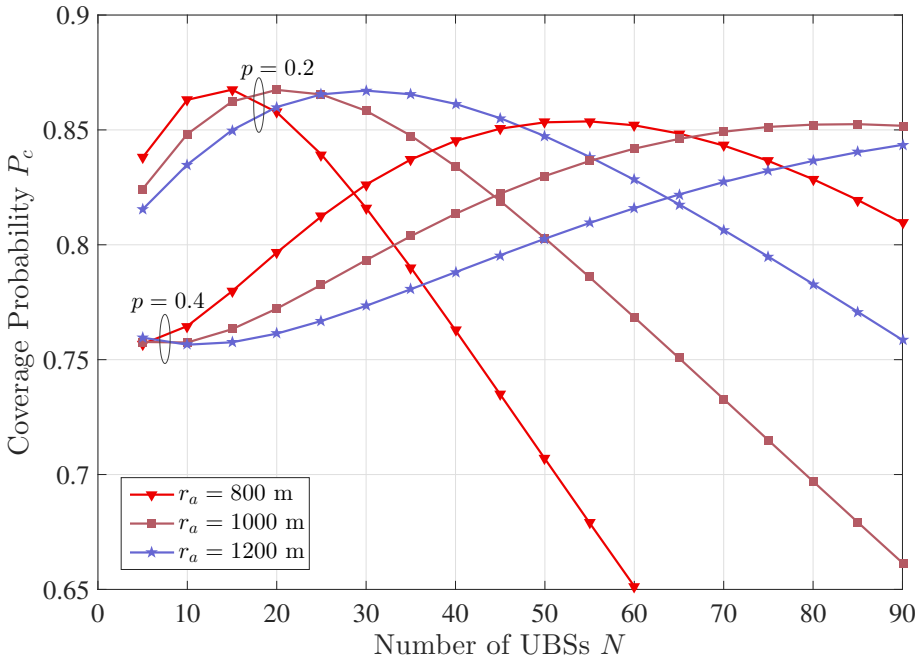

Figure 5.13: Coverage probability vs assisting UBS number N for different r_a and p ($\bar{H}_B = 30$ m).

as the N increases until it reaches its maximum at a certain optimal N. Beyong this number the interference from multiple UBSs lowers the received SINR, thus greatly decreasing coverage probability, especially when shadowing is present. Aditionnaly, Figure 5.12 demonstrates that the optimal N decreases with increasing h and also with the presence of shadowing. For an altitude around 200 m $N = 15$ without shadowing and $N = 10$ with shadowing, while at $h = 150$ m $N = 35$ without shadowing and $N = 25$ with shadowing, which shows that we

need to assist a large number of UBSs at low altitudes and a small number at high altitudes.

Figure 5.13 shows the coverage probability as a function of N with various city blocage density indexes p. For low-density urban areas ($p = 0.2$), it is optimal to have only 15 UBSs (r_a=800m). This is because most UBSs are already in LoS connection with the user. Increasing N will just cause substantial interference. When $p = 0.4$, the optimal N is 55, as more blockages increase the probability of NLoS propagation, and assisting more UBSs increases the LoS probability. It is important to note that the optimal N increases as r_a increases. This is because the UBSs are more widely distributed throughout a larger, finite area, which increases the distance between them and the typical user. Consequently, the probability of buildings obstructing the communication path becomes greater. Adding more UBSs can boost the LoS probability and ultimately improve the coverage probability.

5.3.6.7 Blockage Effects on the Coverage Probability

The impact of 3D blockage density on the coverage probability is examined in Figure 5.14. Figure 5.14(a) illustrates the coverage probability as a function of blockage density at different UBSs's altitude. The coverage probability increases at first, even with higher blockage density λ_B, and then decreases at a certain value of λ_B and this value increases with altitude. The coverage probability's early improvement is due to blockages generating dominating interference in the NLoS connection, which produces an enhanced received SINR. However, a significant increase in λ_B reduces interference in LoS connections, but also result in NLoS transmission of the dominating serving signals, which deteriorates the coverage probability. A relevant finding from Figure 5.14(a) is that in areas with few blockages the coverage probability is maximized by deploying UBSs at low altitude, and in areas with numerous blockages the coverage probability is maximized by deploying UBSs at high altitude. We can point out that blockages can enhance coverage by minimizing interference, although this advantage is restricted.

Figure 5.14(b) illustrates the coverage probability vs. blockage density with various path loss exponents on LoS/NLoS links. We first examine the impact of the LoS link path loss exponent under a fixed value of $\alpha_t^{NLoS} = 4$. When α_t^{LoS} decreases, coverage performance deteriorates at very low λ_B, while it increases at high λ_B. This is because a low α_t^{LoS} will increase both the received signal power and the interference power from LoS BSs (GBSs and UBSs). With the presence of several blockages, the interferences from NLoS BSs will predominate and improve the received SINR and with the presence of few blockages, the interferences from LoS BSs will predominate. On the other hand, increasing the value of α_t^{NLoS} with a fixed value of $\alpha_t^{LoS} = 2.5$ significantly improves coverage performance, because this reduces the interference power in

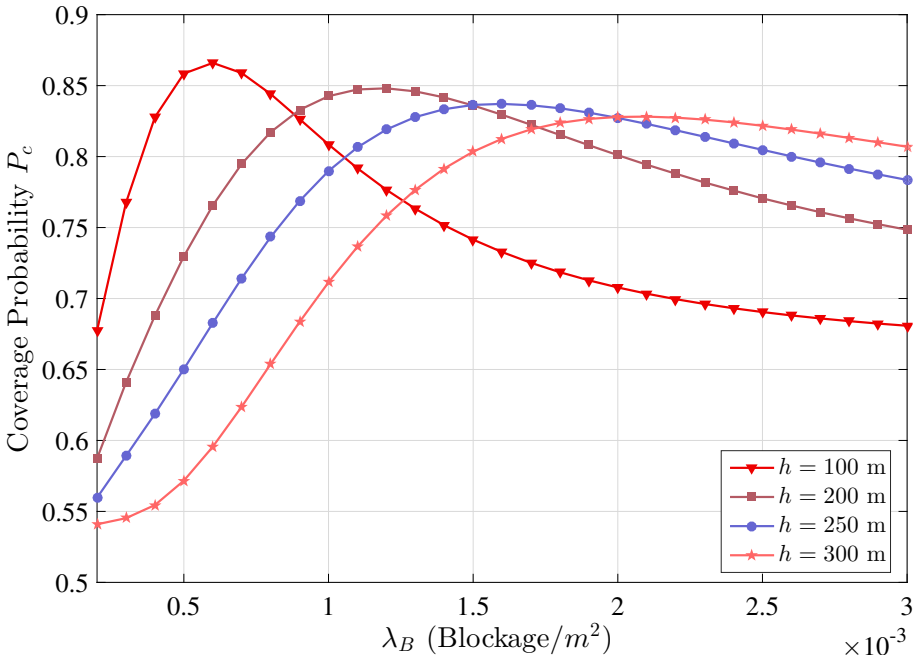

(a) Impact of blocage density for different h

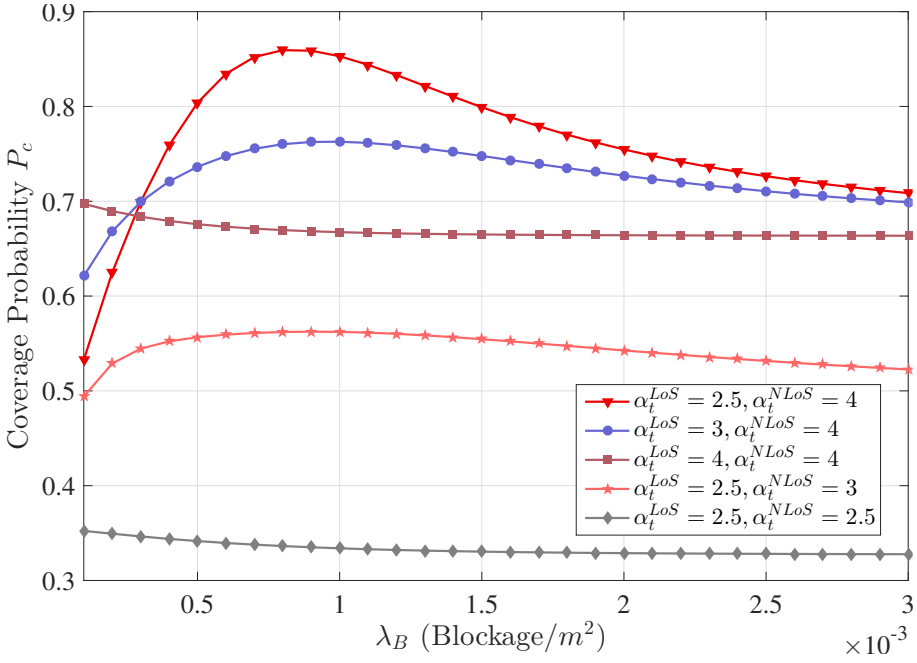

(b) Impact of blockage density for different path loss exponent.

Figure 5.14: Coverage probability. vs blocage density.

LoS link. An important finding to note from Figure 5.14(b) is that for a dense or ultra-dense city ($\lambda_B > 0.002$), a higher coverage probability is achieved when $\alpha_{LoS} = 2.5$ and $\alpha_{NLoS} = 4$.

5.3.6.8 Impact of N and N_a on the ASE

The performance of ASE is investigated in Figure 5.15. Figure 5.15(a) shows the ASE as a function of the number of assisting UBSs at different altitudes and with different numbers of

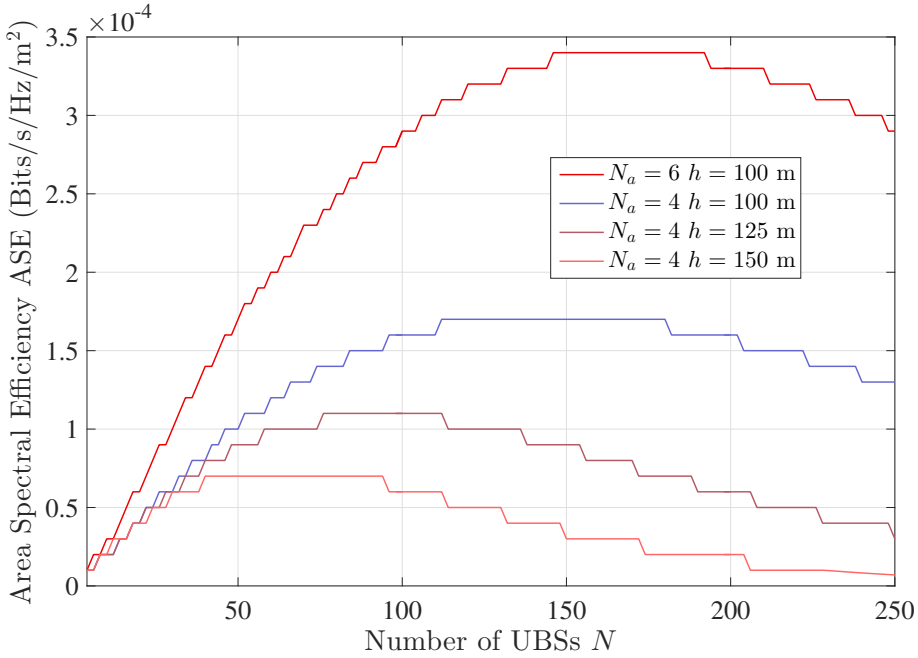

(a) Impact of UBS number on the ASE.

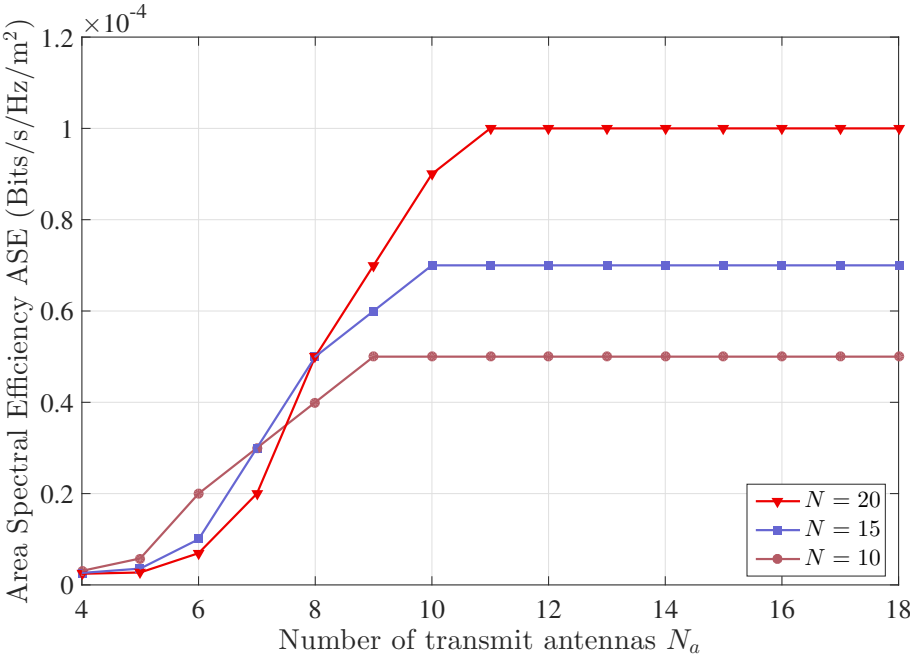

(b) Impact of number of antennas on the ASE.

Figure 5.15: Area spectral efficiency vs. the number of assisting UBS N and the number of antennas N_a.

transmit antennas N_a. The ASE exhibits a staircase shape. The optimal N that maximizig the ASE decreases as UBS altitude increases. This analysis can be used to determine the optimal altitude for ASE enhancement when the number of assisting UBSs is limited. Moreover, increasing N_a significantly improves ASE compared to the results obtained in [46]. This is due to the increased coverage probability, as shown in Figure 5.10(b).

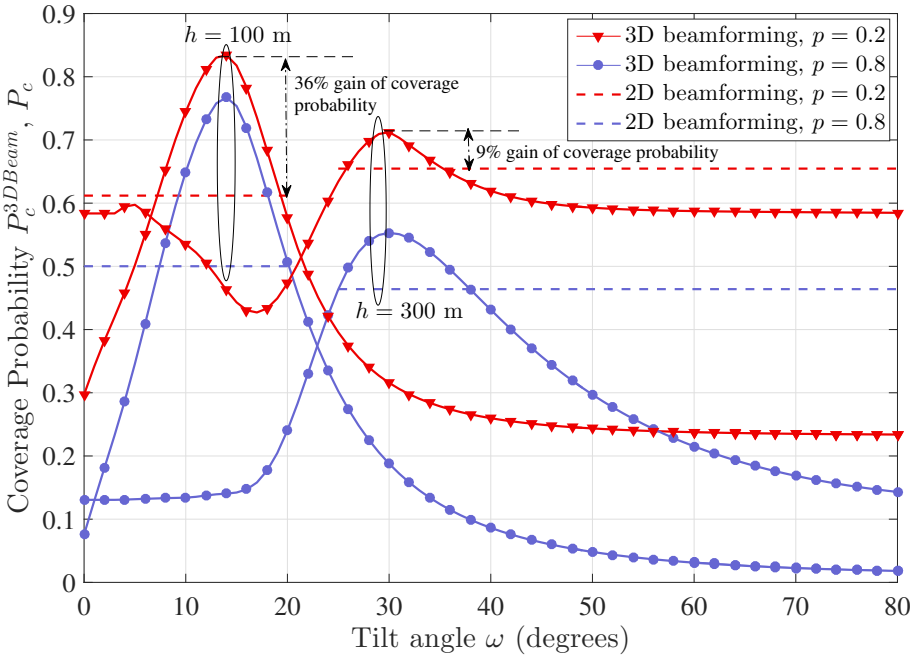

Figure 5.16: Coverage probability vs. tilt angle, compraraison between 2D and 3D beamforming technologies for different p and altitude h ($\theta_d = 6°$, $SLL = 18$ dB°).

Figure 5.15(b) shows the impact of increasing the number of antennas N_a on ASE performance. The study demonstrates that the ASE increases with N_a up to a certain point, after which it remains constant, because greater N_a improves the SINR. It is important to note that ASE can be greatly improved by deploying a small number of UBSs equipped with a few MIMO antennas (less than 8) while deploying a large number of UBSs equipped with large MIMO antennas due to the better spatial multiplexing created.

5.3.6.9 Comparaison between 2D and 3D Beamforming

Figure 5.16 illustrates the impact of using a 3D beamforming model versus a 2D beamforming model on coverage probability. The graph displays the coverage probability as a function of the downtilt angle in suburban and ultra-dense cities, with diffrent UBS altitude. The dotted plots correspond to 2D beamforming and the solid plots correspond to 3D beamforming. It is evident that there exists an optimal tilt angle that maximizes coverage and is dependent on the altitude of the UBS. This angle, is not affected by the environment type and remains fixed for suburban and dense urban environments. To enhance the coverage probability, it is recommended to adjust the antenna radiation pattern in both the horizontal and vertical planes by carefully selecting the downtilt angle especially at low altitude. As seen in Figure 5.16 the 3D beamforming brings 36% coverage gain when UBS altitude $h = 100$m and city blockage density $p = 0.2$ and brings 9% coverage gain when UBS altitude $h = 300$m and city blockage

density $p = 0.2$. The results additionally indicate that, when operating at low UBS altitudes, it is recommended to use a low downtilt angle for optimal performance.

5.4 Conclusion

In this chapter, the downlink performance analysis of mmWave UAV-assisted cellular networks in isolated regions and in hotspot areas with 3D blockages of buildings are introduced. First we have derived the association probabilities and the conditional coverage probabilities relying on the serving and interfering distance distribution and integrating the randomness in LoS/NLoS link. After that, we have obtained the overall coverage probability and the spectral efficicency expressions. Monte Carlo simulations results have confirmed the analytical derivations. The findings of the single-tier model indicated the importance of meticulously adjusting the downtilt angle in relation to the altitude and the number of SA UBSs. The findings of the VHetNets model in hotspot areas indicated that the combination of mmWave UBSs networks with MU-MIMO beamforming significantly enhanced performance, even in the presence of 3D blockages, by selecting the optimal number and altitude of UBSs, and the optimal tilt angle.

Conclusion and Future Works

Providing universal coverage by the currently installed terrestrial cellular networks seems inconsequential mostly because of significant ICI, severe shadowing and path loss attenuation, high user demand in hotspots, and static infrastructure. UAV networks and VHetNets are implemented as new network architectures which are currently the focus of a great deal of interest to address the coverage issues in 5G networks. However, a number of significant issues remain open and in need of further investigation, citing the importance of accurately modeling communication behavior in these new networks.

In this thesis, new analytical frameworks for system modeling, mathematical analysis, performance assessment and optimization were developed. The work is based on the use of the stochastic geometry approach, which is the optimal tool for coverage analysis in 5G networks. The adoption of an appropriate topological model is of vital relevance to performance analysis. The analysis focused on the assistance of a finite 3D UAV network in two scenarios where the most modern and up-to-date technologies were incorporated.

The introduction of this thesis outlines the problem statement, motivations, related works, objectives, and contributions. Two contributions are investigated, in which different network topologies are considered.

In Chapter 1, we presented the coverage analytical and evaluative techniques for 5G cellular networks that have been developed in the literature. We delineated the disparate network architectures and the new UAV networks that are being developed to enhance performance. Furthermore, we provided an overview of the mathematical tools of stochastic geometry.

In Chapter 2, the propagation channel modeling of aerial and terrestrial networks and their characteristics were meticulously delineated. The various user association strategies were presented and discussed. The stochastic geometry theory was employed to present an analytical measurement of performance metrics such as coverage probability and spectral efficiency, with a focus on the crucial factor, the SINR. The fundamental principles of Monte Carlo optimization algorithm simulation were elucidated.

In chapter 3, the first topology was presented, comprising a single swarm of UBSs, designed to provide communications assistance in isolated regions that were not covered by traditional

networks. These regions were considered to be finite circular disks. In this specific scenario, the PPP cannot accurately characterize UBSs' deployment as they are deployed in a finite region with a predefined number. To capture this feature, the BPP is used for the UBS spatial distribution. The number of SA UBSs reusing the same resource block is determined and the 3D beamforming technique is implemented, searching for the optimum down tilt angle to mitigate interference and overcome the high propagation loss of mmWave communications. The relevant distance distributions between a randomly selected user located at a certain distance from the origin to a UBS were obtained.

In Chapter 4, the second topology is defined as a congested network of GBSs, assisted by a finite number of UBSs in dense cities. This VHetNet topology depicts hotspot scenarios by distributing users around GBSs in a TCP model. The dense urban areas are distinguished by the prevalence of high-rise buildings, which can impede the transmission of communication links. This phenomenon has not been extensively studied by researchers. Consequently, we investigated the constraints imposed by 3D blockages, represented by buildings, using a Boolean scheme. In this context, we developed new A2G and G2G channel models different from the widely used models, by computing new formulas for the probability of LoS and NLoS paths, taking into account the characteristics of 3D blockages. To cope with the high user density, we employed the new MU-MIMO beamforming technology. This technology enables a UBS to serve multiple users simultaneously using the same frequency resources while mitigating intensified shadow effects.

The downlink performance assessment of the two proposed mathematical frameworks, validated by the Monte Carlo simulation results, is detailed in Chapter 5. Initially, we derived the overall coverage probability as a function of the association probabilities and the conditional coverage probabilities. Subsequently, we obtained the spectral efficiency expression. The findings of the single-tier model emphasized the importance of meticulously adjusting the downtilt angle in relation to the altitude and the number of SA UBSs to improve the performance. The findings of the VHetNets model in hotspot areas indicated that the addition of UBSs combined with MU-MIMO beamforming can establish a dynamic flying cellular network to provide high-coverage wireless services even in the presence of 3D blockages.

Future Works

It is of the utmost importance to propose new avenues for future research endeavors to investigate the challenges and potentialities that have not yet been addressed by previous studies. The work described in this thesis can be pursued along several lines of research.

- The consideration of various types of users for a more comprehensive understanding of the model. These include, for example, D2D communicating users, the users served by UBSs are distinct from those served by GBSs, or the coexistence of aerial and ground users in VHetNets.
- Modeling the UBS distribution in correlation with hotspot locations.
- The use of a more realistic directional pattern model in 3D mmWave networks, which incorporates a shaped main beam and secondary lobes. A Gaussian beam steering error may be included.
- The integration of heterogeneous UAV networks, comprising UAVs with varying power transmission, altitudes, and flying capabilities, as well as analyzing how the combined capabilities of different UAV types can improve coverage.

Appendices

Appendix A

Proof of Lemma 5.2.2

Recall that $\mathcal{B}_{R_l^v(r)}$ is the event that the interfering UBS being in $v \in \{LoS, NLoS\}$ is located $R_l^v(r)$ away from the typical user. Since the number of UBSs is fixed we can write $\mathcal{B}_{R^v_{LoS}(r)} \cup \mathcal{B}_{R^v_{NLoS}(r)}$. Hereafter we denote by $\mathcal{Q}_l^{LoS}$, $\mathcal{Q}_l^{NLoS}$ the probability that the interfering UBS is in LoS, NLoS link respectively conditioned on the two events $\mathcal{B}_{R^v_{LoS}(r)}$ and $\mathcal{B}_{R^v_{NLoS}(r)}$ are mutually exclusive and given that the service UBS is in l connection with user. $\mathcal{Q}_l^v$ can be defined as

$$\begin{aligned}\mathcal{Q}_l^v =& \mathbb{P}(\mathcal{B}_{R_l^v(r)} | \mathcal{B}_{R_l^v(r)} \cup \mathcal{B}_{R_l^b(r)}) \\ =& \frac{\mathbb{P}(\mathcal{B}_{R_l^v(r)} | \text{the serving UBS is in } l \text{ link})}{\mathbb{P}(\mathcal{B}_{R_l^v(r)} | \text{the serving UBS is in } l \text{ link} + \mathcal{B}_{R_l^v(r)} | \text{the serving UBS is in } l \text{ link})} \\ =& \frac{\int_{R_l^v(r)}^{x_u} f_{X_i}(z) P_v(z)}{\sum\limits_q \int_{R_l^v(r)}^{x_u} f_{X_i}(z) P_q(z) dz},\end{aligned} \tag{5.39}$$

where $l, v, b \in \{LoS, NLoS\}$ and $b \neq v$.

Using the aggregate interference equation in (3.8) and applying the Laplace transform definition, $\mathcal{L}(\delta, R_l^{LoS}(r), R_l^{NLoS}(r))$ can be written as follows

$$\mathcal{L}_I(\delta, R_l^{LoS}(r), R_l^{NLoS}(r)) = \mathbb{E}_{I|\mathcal{I}_{LoS}\cup\mathcal{I}_{NLoS}}\Big[\exp\left(-\delta I\right)\Big]$$

$$= \mathbb{E}_{Z_i,h_U^v|\mathcal{I}_{LoS}\cup\mathcal{I}_{NLoS}}\left[\exp\left(-\delta\sum_{i=1}^{K}\sum_{v}P_U\Omega(\omega,\theta(Z_i))h_U^v\varphi_v^{-1}Z_i^{-\alpha_U^v}\right)\right]$$

$$= \prod_{i=1}^{K}\sum_{v}\mathbb{E}_{Z_i,h_U^v|\mathcal{I}_v}\left[\exp\left(-\delta P_U\Omega(\omega,\theta(Z_i))h_U^v\varphi_v^{-1}Z_i^{-\alpha_U^v}\mathcal{Q}_{sL}\right)\right]$$

$$\overset{(a)}{=} \prod_{i=1}^{K}\sum_{v}\mathbb{E}_{Z_i|\mathcal{I}_v}\left[\left(\frac{m_U^v}{m_U^v+\delta P_U\Omega(\omega,\theta(Z_i))\varphi_v^{-1}Z_i^{-\alpha_U^v}}\right)^{m_U^v}\frac{\int_{R_l^v(r)}^{x_u}f_{X_i}(z)P_U^v(z)}{\sum_q\int_{R_l^v(r)}^{x_u}f_{X_i}(z)P_q(z)dz}\right]$$

$$= \sum_{v}\left[\int_{R_l^v(r)}^{x_u}\left(\frac{m_U^v}{m_U^v+\delta P_U\Omega(\omega,\theta(z))\varphi_v^{-1}z^{-\alpha_L}}\right)^{m_U^v}\frac{\int_{R_l^v(r)}^{x_u}f_{X_i}(z)P_U^v(z)}{\sum_q\int_{R_l^v(r)}^{x_u}f_{X_i}(z)P_q(z)dz}\right.$$

$$\left.f_{Z_i}\left(z|\mathcal{B}_{R_l^v(r)},y_0\right)dz\right]^{K-1}, \tag{5.40}$$

where (a) follows from the gamma distribution of the channel gain h_U^v using the moment generating function. The $K-1$ comes from the number of SA UBSs that are interfering with the serving UBS. Substitution of the equation (3.16) in (5.40) results in (5.6).

Appendix B

Proof of Theorem 5.7

The serving distance conditioned on the event that UBS A_i is l link is denoted by $\hat{X}_r^l = r$, $P_{c,l}^U$ can be defined as follows

$$\begin{aligned}
P_{c,U}^l(y_0) =& \mathbb{P}\left(SINR > \mathcal{T} | \text{the serving UBS is in } l \text{ link} \right) \\
=& \mathbb{E}_{X_r^l}\left[\mathbb{P}\left(\frac{P_U \Omega(\omega, \theta(X_r^l)) h_U^l \varphi_l^{-1} X_r^{l-\alpha_U^l}}{I + N_0} > \mathcal{T} | \text{the serving UBS is in } l \text{ link} \right) \right] \\
=& \mathbb{E}_{\hat{X}_r^l}\left[\mathbb{P}\left(h_U^l > \frac{\mathcal{T}\varphi_l \hat{X}_r^{l\alpha_U^l}}{P_U \Omega(\omega, \theta(\hat{X}_r^l))} (I + N_0) \right) \right] \\
=& \mathbb{E}_{\hat{X}_r^l}\left[\bar{F}_{h_U^l}\left(\frac{\mathcal{T}\varphi_l \hat{X}_r^{l\alpha_U^l}}{P_U \Omega(\omega, \theta(\hat{X}_r^l))} (I + N_0) \right) \right], \qquad (5.41)
\end{aligned}$$

where $\bar{F}_{h_U^l}(\eth)$ is the CCDF of h_U^l Since h_U^l is a normalized gamma random variable, we can write $\bar{F}_{h_U}(\eth) = \dfrac{\Gamma_u(m, m\eth)}{\Gamma(m)}$, where $\eth > 0$ and $\Gamma_u(m, m\eth)$ is the upper incomplete gamma function. Following [157] $\bar{F}_{h_U^l}(\eth)$ can be approximated using the gamma approximation to simplify the evaluation process, which can be formulated as

$$\begin{aligned}
P_{c,U}^l =& \mathbb{E}_{\hat{X}_r^l, I}\left[1 - \left(1 - \exp\left(\frac{\mathcal{T}\varphi_l \hat{X}_r^{l\alpha_U^l}}{P_U \Omega\big(\omega, \theta(\hat{X}_r)\big)} \Big(I + N_0 \Big) \right) \right)^{m_U^l} \right] \\
\overset{(a)}{=}& \sum_{n=1}^{m_U^l} (-1)^{n+1} \binom{m_U^l}{n} \mathbb{E}_{\hat{X}_r^l, I}\left[\exp\left(\frac{-n\varepsilon_U^l \mathcal{T}\varphi_l \hat{X}_r^{l\alpha_U^l}}{P_U \Omega\big(\omega, \theta(\hat{X}_r^l)\big)} \Big(I + N_0 \Big) \right) \right] \\
=& \sum_{n=1}^{m_U^l} (-1)^{n+1} \binom{m_U^l}{n} \mathbb{E}_{\hat{X}_r^l}\left[\exp\left(\frac{-n\varepsilon_U^l \mathcal{T}\varphi_l \hat{X}_r^{l\alpha_U^l}}{P_U \Omega\big(\omega, \theta(\hat{X}_r^l)\big)} N_0 \right) \mathbb{E}_I\left[\exp\left(\frac{-n\varepsilon_U^l \mathcal{T}\varphi_l \hat{X}_r^{l\alpha_U^l}}{P_U \Omega\big(\omega, \theta(\hat{X}_r^l)\big)} I \right) \right] \right] \\
=& \sum_{n=1}^{m_U^l} (-1)^{n+1} \binom{m_u^l}{n} \exp\Big(-\delta N_0 \Big) \mathbb{E}_{\hat{X}_r^l}\left[\mathcal{L}_I\left(\delta, R_l^{LoS}\left(\hat{X}_r^l \right), R_l^{NLoS}\left(\hat{X}_r^l \right) \right) \right] \\
=& \int_h^{x_u} \sum_{n=1}^{m_U^l} (-1)^{n+1} \binom{m_U^l}{n} \exp\Big(-\delta N_0 \Big) \mathcal{L}_I\left(\delta, R_l^{LoS}(r), R_l^{NLoS}(r) \right) f_{\hat{X}_r^l}(r) dr, \qquad (5.42)
\end{aligned}$$

where (a) comes from the binomial theorem and $\delta = \dfrac{n\varepsilon_U^l m_U^l \mathcal{T}\varphi_l r^{\alpha_U^l}}{P_U \Omega\big(\omega, \theta(r)\big)}$. This completes the proof of (5.7).

Appendix C

Proof of Lemma 5.3.6

The Laplace transform $\mathcal{L}_{I_{G_1}}(\delta, R_{t^l}^{G_1^v})$ can be written as follows

$$\begin{aligned}
\mathcal{L}_{I_{G_1}}(\delta, R_{t^l}^{G_1^v}) =& \mathbb{E}_{I_{G_1}}\left[\exp\Big(-\delta I_{G_1}\Big)\right] \\
=& \mathbb{E}_{\Phi_G, h_G^v}\left[\exp\left(-\delta \sum_v \sum_{M_j \in \Phi_G \setminus \psi_{t^l}^{G_1^v}} P_G G_G h_G^v W_j^{-\alpha_G^v}\right)\right] \\
=& \mathbb{E}_{\Phi_G, h_G^v} \prod_v \prod_{M_j \in \Phi_G \setminus \psi_{t^l}^{G_1^v}} \left[\exp\Big(-\delta P_G G_G h_G^v W_j{}^{-\alpha_G^v}\Big)\right] \\
\overset{(a)}{=}& \mathbb{E}_{\Phi_G} \prod_v \prod_{M_j \in \Phi_G \setminus \psi_{t^l}^{G_1^v}} \left[\left(\frac{m_G^v}{m_G^v + \delta P_G G_I^G W^{-\alpha_G^v}}\right)^{m_G^v}\right] \\
\overset{(b)}{=}& \prod_v \exp\left(-2\lambda_G \pi \int_{R_{t^l}^{G_1^v}(r)}^{\infty} \left[1 - \left(\frac{m_G^v}{m_G^v + \delta P_G G_I^G w^{-\alpha_G^v}}\right)^{m_G^v} w P_G^v(w) dw\right],
\end{aligned} \tag{5.43}$$

where $\psi_{t^l}^{G_1^v}$ is a disk with radius $R_{t^l}^{G_1^v}(r)$ denoting the excluded region where no interfering GBS_1 exists, (a) follows from $h_G^v \sim \Gamma\left(m_G^v, \frac{1}{m_G^v}\right)$ and (b) is achieved by applying the PGFL of PPP [34].

Bibliography

[1] N. Bhandari, S. Devra, and K. Singh, "Evolution of cellular network: from 1G to 5G," *International journal of engineering and techniques*, vol. 3, no. 5, pp. 98–105, 2017.

[2] O. T. Ajayi, S. O. Onidare, A. A. Ayeni, Q. R. Adebowale, S. O. Yusuf, and A. Ogundele, "Performance evaluation of GSM and WCDMA networks: A case study of the University of Ilorin," *International Journal on Electrical Engineering and Informatics*, vol. 13, no. 1, pp. 87–106, 2021.

[3] M. Rumney *et al.*, *LTE and the evolution to 4G wireless: Design and measurement challenges*. John Wiley & Sons, 2013.

[4] M. Agiwal, A. Roy, and N. Saxena, "Next generation 5G wireless networks: A comprehensive survey," *IEEE communications surveys & tutorials*, vol. 18, no. 3, pp. 1617–1655, 2016.

[5] Y. Daldoul, D.-E. Meddour, and A. Ksentini, "Performance evaluation of OFDMA and MU-MIMO in 802.11 ax networks," *Computer Networks*, vol. 182, p. 107477, 2020.

[6] M. G. Kachhavay and A. P. Thakare, "5G technology-evolution and revolution," *International Journal of Computer Science and Mobile Computing*, vol. 3, no. 3, pp. 1080–1087, 2014.

[7] D. Taneja, "The internet of things: overview & analysis," *International Journal of Electronics Engineering*, vol. 11, pp. 407–413, 2019.

[8] A. K. Hassan, M. Moinuddin, U. M. Al-Saggaf, O. Aldayel, T. N. Davidson, and T. Y. Al-Naffouri, "Performance analysis and joint statistical beamformer design for multiuser MIMO systems," *IEEE Communications Letters*, vol. 24, no. 10, pp. 2152–2156, 2020.

[9] C. Qi, K. Chen, O. A. Dobre, and G. Y. Li, "Hierarchical codebook-based multiuser beam training for millimeter wave massive MIMO," *IEEE Transactions on Wireless Communications*, vol. 19, no. 12, pp. 8142–8152, 2020.

[10] Z. Xiao, L. Zhu, Y. Liu, P. Yi, R. Zhang, X.-G. Xia, and R. Schober, "A survey on millimeter-wave beamforming enabled UAV communications and networking," *IEEE Communications Surveys & Tutorials*, vol. 24, no. 1, pp. 557–610, 2021.

[11] L. Zhang, H. Zhao, S. Hou, Z. Zhao, H. Xu, X. Wu, Q. Wu, and R. Zhang, "A survey on 5G millimeter wave communications for UAV-assisted wireless networks," *IEEE Access*, vol. 7, pp. 117460–117504, 2019.

[12] A. A. Salih, S. Zeebaree, A. S. Abdulraheem, R. R. Zebari, M. Sadeeq, and O. M. Ahmed, "Evolution of mobile wireless communication to 5G revolution," *Technology Reports of Kansai University*, vol. 62, no. 5, pp. 2139–2151, 2020.

[13] L. Rao, M. Pant, L. Malviya, A. Parmar, and S. V. Charhate, "5G beamforming techniques for the coverage of intended directions in modern wireless communication: in-depth review," *International Journal of Microwave and Wireless Technologies*, vol. 13, no. 10, pp. 1039–1062, 2021.

[14] X. Wang and M. C. Gursoy, "Coverage analysis for energy-harvesting UAV-assisted mmWave cellular networks," *IEEE Journal on Selected Areas in Communications*, vol. 37, no. 12, pp. 2832–2850, 2019.

[15] S. Samarakoon, M. Bennis, W. Saad, M. Debbah, and M. Latva-Aho, "Ultra dense small cell networks: Turning density into energy efficiency," *IEEE Journal on Selected Areas in Communications*, vol. 34, no. 5, pp. 1267–1280, 2016.

[16] A. Chatterjee and S. S. Das, "Downlink Coverage Analysis of 3-D Ultra Dense Networks with Realistic Propagation Conditions," in *2019 IEEE International Conference on Advanced Networks and Telecommunications Systems (ANTS)*, pp. 1–6, IEEE, 2019.

[17] M. Ding, D. Lopez-Perez, H. Claussen, and M. A. Kaafar, "On the fundamental characteristics of ultra-dense small cell networks," *IEEE Network*, vol. 32, no. 3, pp. 92–100, 2018.

[18] S. Joshi and R. K. Mallik, "Coverage probability analysis in a device-to-device network: Interference functional and Laplace transform based approach," *IEEE Communications Letters*, vol. 23, no. 3, pp. 466–469, 2019.

[19] I. Trigui and S. Affes, "Unified analysis and optimization of D2D communications in cellular networks over fading channels," *IEEE Transactions on Communications*, vol. 67, no. 1, pp. 724–736, 2018.

[20] B. Li, Z. Fei, and Y. Zhang, "UAV communications for 5G and beyond: Recent advances and future trends," *IEEE Internet of Things Journal*, vol. 6, no. 2, pp. 2241–2263, 2018.

[21] S. Hayat, E. Yanmaz, and R. Muzaffar, "Survey on unmanned aerial vehicle networks for civil applications: A communications viewpoint," *IEEE Communications Surveys & Tutorials*, vol. 18, no. 4, pp. 2624–2661, 2016.

[22] K. P. Valavanis and G. J. Vachtsevanos, *Handbook of unmanned aerial vehicles*, vol. 1. Springer, 2015.

[23] M. Asadpour, B. Van den Bergh, D. Giustiniano, K. A. Hummel, S. Pollin, and B. Plattner, "Micro aerial vehicle networks: An experimental analysis of challenges and opportunities," *IEEE Communications Magazine*, vol. 52, no. 7, pp. 141–149, 2014.

[24] M. Mozaffari, W. Saad, M. Bennis, and M. Debbah, "Mobile unmanned aerial vehicles (UAVs) for energy-efficient Internet of Things communications," *IEEE Transactions on Wireless Communications*, vol. 16, no. 11, pp. 7574–7589, 2017.

[25] M. Mozaffari, W. Saad, M. Bennis, and M. Debbah, "Efficient deployment of multiple unmanned aerial vehicles for optimal wireless coverage," *IEEE Communications Letters*, vol. 20, no. 8, pp. 1647–1650, 2016.

[26] Q. Wu, J. Xu, Y. Zeng, D. W. K. Ng, N. Al-Dhahir, R. Schober, and A. L. Swindlehurst, "A comprehensive overview on 5G-and-beyond networks with UAVs: From communications to sensing and intelligence," *IEEE Journal on Selected Areas in Communications*, vol. 39, no. 10, pp. 2912–2945, 2021.

[27] S. Sekander, H. Tabassum, and E. Hossain, "Multi-tier drone architecture for 5G/B5G cellular networks: Challenges, trends, and prospects," *IEEE Communications Magazine*, vol. 56, no. 3, pp. 96–103, 2018.

[28] Q. Liu, R. Liu, Z. Wang, and J. S. Thompson, "UAV swarm-enabled localization in isolated region: a rigidity-constrained deployment perspective," *IEEE Wireless Communications Letters*, vol. 10, no. 9, pp. 2032–2036, 2021.

[29] A. Colpaert, E. Vinogradov, and S. Pollin, "3D beamforming and handover analysis for UAV networks," in *2020 IEEE Globecom Workshops (GC Wkshps*, pp. 1–6, IEEE, 2020.

[30] S. Shamai and A. D. Wyner, "Information-theoretic considerations for symmetric, cellular, multiple-access fading channels. I," *IEEE Transactions on Information Theory*, vol. 43, no. 6, pp. 1877–1894, 1997.

[31] S. Shamai and A. D. Wyner, "Information-theoretic considerations for symmetric, cellular, multiple-access fading channels. II," *IEEE Transactions on Information Theory*, vol. 43, no. 6, pp. 1895–1911, 1997.

[32] F. Baccelli and B. Błaszczyszyn, "Stochastic Geometry and Wireless Networks, Volume I—Theory," *foundations and trends® in networking*, vol. 3, no. 3–4, 2009.

[33] F. Baccelli, B. Błaszczyszyn, *et al.*, "Stochastic geometry and wireless networks: Volume II applications," *foundations and trends® in networking*, vol. 4, no. 1–2, pp. 1–312, 2010.

[34] M. Haenggi, *Stochastic geometry for wireless networks*. Cambridge University Press, 2012.

[35] F. Baccelli and S. Zuyev, "Stochastic geometry models of mobile communication networks," in *Frontiers in queueing: models and applications in science and engineering*, pp. 227–243, 1998.

[36] S. N. Chiu, D. Stoyan, W. S. Kendall, and J. Mecke, *Stochastic geometry and its applications*. John Wiley & Sons, 2013.

[37] J. G. Andrews, F. Baccelli, and R. K. Ganti, "A tractable approach to coverage and rate in cellular networks," *IEEE Transactions on communications*, vol. 59, no. 11, pp. 3122–3134, 2011.

[38] H. S. Dhillon, R. K. Ganti, F. Baccelli, and J. G. Andrews, "Modeling and analysis of K-tier downlink heterogeneous cellular networks," *IEEE Journal on Selected Areas in Communications*, vol. 30, no. 3, pp. 550–560, 2012.

[39] H. ElSawy, A. Sultan-Salem, M.-S. Alouini, and M. Z. Win, "Modeling and analysis of cellular networks using stochastic geometry: A tutorial," *IEEE Communications Surveys & Tutorials*, vol. 19, no. 1, pp. 167–203, 2016.

[40] T. Bai and R. W. Heath, "Coverage and rate analysis for millimeter-wave cellular networks," *IEEE Transactions on Wireless Communications*, vol. 14, no. 2, pp. 1100–1114, 2014.

[41] P. Koivumäki, A. F. Molisch, and K. Haneda, "Line-of-sight probability in cluttered urban microcells: Analyses using poisson point process and point cloud," *IEEE Transactions on Antennas and Propagation*, vol. 70, no. 3, pp. 2161–2173, 2021.

[42] M. Afshang and H. S. Dhillon, "Fundamentals of modeling finite wireless networks using binomial point process," *IEEE Transactions on Wireless Communications*, vol. 16, no. 5, pp. 3355–3370, 2017.

[43] Q. Ying, Z. Zhao, Y. Zhou, R. Li, X. Zhou, and H. Zhang, "Characterizing spatial patterns of base stations in cellular networks," in *2014 IEEE/CIC International Conference on Communications in China (ICCC)*, pp. 490–495, IEEE, 2014.

[44] M. Alzenad and H. Yanikomeroglu, "Coverage and rate analysis for vertical heterogeneous networks (VHetNets)," *IEEE Transactions on Wireless Communications*, vol. 18, no. 12, pp. 5643–5657, 2019.

[45] E. Turgut and M. C. Gursoy, "Downlink analysis in unmanned aerial vehicle (UAV) assisted cellular networks with clustered users," *IEEE Access*, vol. 6, pp. 36313–36324, 2018.

[46] X. Wang, H. Zhang, Y. Tian, and V. C. Leung, "Modeling and analysis of aerial base station-assisted cellular networks in finite areas under LoS and NLoS propagation," *IEEE Transactions on Wireless Communications*, vol. 17, no. 10, pp. 6985–7000, 2018.

[47] N. Cherif, M. Alzenad, H. Yanikomeroglu, and A. Yongacoglu, "Downlink coverage and rate analysis of an aerial user in vertical heterogeneous networks (VHetNets)," *IEEE Transactions on Wireless Communications*, vol. 20, no. 3, pp. 1501–1516, 2020.

[48] W. Tang, H. Zhang, and Y. He, "Tractable modelling and performance analysis of UAV networks with 3D blockage effects," *IEEE Wireless Communications Letters*, vol. 9, no. 12, pp. 2064–2067, 2020.

[49] W. Tang, H. Zhang, and Y. He, "Performance analysis of power control in urban UAV networks with 3D blockage effects," *IEEE Transactions on Vehicular Technology*, vol. 71, no. 1, pp. 626–638, 2021.

[50] A. Sufyan, K. B. Khan, O. A. Khashan, T. Mir, and U. Mir, "From 5G to beyond 5G: A Comprehensive Survey of Wireless Network Evolution, Challenges, and Promising Technologies," *Electronics*, vol. 12, no. 10, p. 2200, 2023.

[51] R. Borralho, A. Mohamed, A. U. Quddus, P. Vieira, and R. Tafazolli, "A survey on coverage enhancement in cellular networks: Challenges and solutions for future deployments," *IEEE Communications Surveys & Tutorials*, vol. 23, no. 2, pp. 1302–1341, 2021.

[52] D. Alkama, S. Zenadji, M. A. Ouamri, A. Khireddine, and M. Azni, "Performance of Resource Allocation for Downlink Non-Orthogonal Multiple Access Systems in Tri-Sectorial Cell," in *2022 IEEE International Conference on Electrical Sciences and Technologies in Maghreb (CISTEM)*, vol. 4, pp. 1–6, IEEE, 2022.

[53] D. Kumar, "Investigating Resource Allocation Techniques and Key Performance Indicators (KPIs) for 5G New Radio Networks: A Review," *International Journal of Computer Networks and Applications*, vol. 10, no. 3, pp. 422–442, 2023.

[54] F. Gul, W. Rahiman, S. Alhady, A. Ali, I. Mir, and A. Jalil, "Meta-heuristic approach for solving multi-objective path planning for autonomous guided robot using PSO–GWO optimization algorithm with evolutionary programming," *Journal of Ambient Intelligence and Humanized Computing*, vol. 12, pp. 7873–7890, 2021.

[55] D. J. Daley, D. Vere-Jones, *et al.*, *An introduction to the theory of point processes: volume I: elementary theory and methods*. Springer, 2003.

[56] D. J. Daley and D. Vere-Jones, *An introduction to the theory of point processes: volume II: general theory and structure*. Springer Science & Business Media, 2007.

[57] A. Karr, *Point processes and their statistical inference*. Routledge, 2017.

[58] T. Bai, R. Vaze, and R. W. Heath, "Using random shape theory to model blockage in random cellular networks," in *2012 International Conference on Signal Processing and Communications (SPCOM)*, pp. 1–5, IEEE, 2012.

[59] Y. Xu, G. Gui, H. Gacanin, and F. Adachi, "A survey on resource allocation for 5G heterogeneous networks: Current research, future trends, and challenges," *IEEE Communications Surveys & Tutorials*, vol. 23, no. 2, pp. 668–695, 2021.

[60] D. J. Birabwa, D. Ramotsoela, and N. Ventura, "Service-aware user association and resource allocation in integrated terrestrial and non-terrestrial networks: A genetic algorithm approach," *IEEE Access*, vol. 10, pp. 104337–104357, 2022.

[61] R. Bajracharya, R. Shrestha, S. Kim, and H. Jung, "6G NR-U based wireless infrastructure UAV: Standardization, opportunities, challenges and future scopes," *IEEE Access*, vol. 10, pp. 30536–30555, 2022.

[62] A. Fotouhi, H. Qiang, M. Ding, M. Hassan, L. G. Giordano, A. Garcia-Rodriguez, and J. Yuan, "Survey on UAV cellular communications: Practical aspects, standardization advancements, regulation, and security challenges," *IEEE Communications surveys & tutorials*, vol. 21, no. 4, pp. 3417–3442, 2019.

[63] E. Vinogradov, H. Sallouha, S. De Bast, M. M. Azari, and S. Pollin, "Tutorial on UAV: A blue sky view on wireless communication," *arXiv preprint arXiv:1901.02306*, 2019.

[64] M. Mozaffari, W. Saad, M. Bennis, Y.-H. Nam, and M. Debbah, "A tutorial on UAVs for wireless networks: Applications, challenges, and open problems," *IEEE communications surveys & tutorials*, vol. 21, no. 3, pp. 2334–2360, 2019.

[65] Y. Lyu, W. Wang, Y. Sun, H. Yue, and J. Chai, "Low Altitude UAV Air-to-Ground Multi-Link Channel Modeling and Analysis At 2.4 and 5.9 GHz," *IEEE Antennas and Wireless Propagation Letters*, 2023.

[66] V. Chamola, P. Kotesh, A. Agarwal, N. Gupta, M. Guizani, *et al.*, "A comprehensive review of unmanned aerial vehicle attacks and neutralization techniques," *Ad hoc networks*, vol. 111, p. 102324, 2021.

[67] K. Nonami, F. Kendoul, S. Suzuki, W. Wang, and D. Nakazawa, *Autonomous flying robots: unmanned aerial vehicles and micro aerial vehicles*. Springer Science & Business Media, 2010.

[68] Y. Zeng, R. Zhang, and T. J. Lim, "Wireless communications with unmanned aerial vehicles: Opportunities and challenges," *IEEE Communications magazine*, vol. 54, no. 5, pp. 36–42, 2016.

[69] M. Ding and D. Lopez-Perez, "Performance impact of base station antenna heights in dense cellular networks," *IEEE Transactions on Wireless Communications*, vol. 16, no. 12, pp. 8147–8161, 2017.

[70] A. Al-Hourani, S. Kandeepan, and S. Lardner, "Optimal LAP altitude for maximum coverage," *IEEE Wireless Communications Letters*, vol. 3, no. 6, pp. 569–572, 2014.

[71] A. Al-Hourani, S. Kandeepan, and A. Jamalipour, "Modeling air-to-ground path loss for low altitude platforms in urban environments," in *2014 IEEE global communications conference*, pp. 2898–2904, IEEE, 2014.

[72] B. Galkin, J. Kibilda, and L. A. DaSilva, "Coverage analysis for low-altitude UAV networks in urban environments," in *GLOBECOM 2017-2017 IEEE Global Communications Conference*, pp. 1–6, IEEE, 2017.

[73] B. P. Sahoo, D. Puthal, and P. K. Sharma, "Toward advanced UAV communications: Properties, research challenges, and future potential," *IEEE Internet of Things Magazine*, vol. 5, no. 1, pp. 154–159, 2022.

[74] M. M. Azari, F. Rosas, A. Chiumento, and S. Pollin, "Coexistence of terrestrial and aerial users in cellular networks," in *2017 IEEE Globecom Workshops (GC Wkshps)*, pp. 1–6, IEEE, 2017.

[75] M. M. Azari, F. Rosas, and S. Pollin, "Cellular connectivity for UAVs: Network modeling, performance analysis, and design guidelines," *IEEE Transactions on Wireless Communications*, vol. 18, no. 7, pp. 3366–3381, 2019.

[76] S. Kang, M. Mezzavilla, A. Lozano, G. Geraci, S. Rangan, V. Semkin, W. Xia, and G. Loianno, "Coexistence of UAVs and terrestrial users in millimeter-wave urban networks," in *2022 IEEE Globecom Workshops (GC Wkshps)*, pp. 1158–1163, IEEE, 2022.

[77] Y. Du, H. Zhang, and J. Peng, "Modeling and coverage analysis for cellular-connected UAVs with up-tilted antenna," *IEEE Communications Letters*, vol. 26, no. 11, pp. 2572–2575, 2022.

[78] D. Alkama, M. A. Ouamri, L. Alkama, and M. Azni, "Cellular-Connected UAVs : Coverage Analysis using SWIPT and Up-Tilted Antenna," in *2023 Electrical Engineering International Conference EEIC'23*, pp. 641–645, 2023. ISBN: 978-9969-9732-0-4.

[79] J. Qiu, J. Lyu, and L. Fu, "Placement optimization of aerial base stations with deep reinforcement learning," in *ICC 2020-2020 IEEE International Conference on Communications (ICC)*, pp. 1–6, IEEE, 2020.

[80] T. Kimura and M. Ogura, "Distributed 3D deployment of aerial base stations for on-demand communication," *IEEE Transactions on Wireless Communications*, vol. 20, no. 12, pp. 7728–7742, 2021.

[81] S. Enayati, H. Saeedi, H. Pishro-Nik, and H. Yanikomeroglu, "Optimal altitude selection of aerial base stations to maximize coverage and energy harvesting probabilities: A stochastic geometry analysis," *IEEE Transactions on Vehicular Technology*, vol. 69, no. 1, pp. 1096–1100, 2019.

[82] S. K. Khan, M. Farasat, U. Naseem, and F. Ali, "Performance evaluation of next-generation wireless (5G) UAV relay," *Wireless Personal Communications*, vol. 113, no. 2, pp. 945–960, 2020.

[83] X. Chen, X. Hu, Q. Zhu, W. Zhong, and B. Chen, "Channel modeling and performance analysis for UAV relay systems," *China Communications*, vol. 15, no. 12, pp. 89–97, 2018.

[84] Q. Wu, J. Xu, Y. Zeng, D. W. K. Ng, N. Al-Dhahir, R. Schober, and A. L. Swindlehurst, "A comprehensive overview on 5G-and-beyond networks with UAVs: From communications to sensing and intelligence," *IEEE Journal on Selected Areas in Communications*, vol. 39, no. 10, pp. 2912–2945, 2021.

[85] T. X. Brown, "Cellular performance bounds via shotgun cellular systems," *IEEE Journal on Selected Areas in Communications*, vol. 18, no. 11, pp. 2443–2455, 2000.

[86] J.-F. Coeurjolly, J. Møller, and R. Waagepetersen, "A tutorial on Palm distributions for spatial point processes," *International Statistical Review*, vol. 85, no. 3, pp. 404–420, 2017.

[87] M. Haenggi, J. G. Andrews, F. Baccelli, O. Dousse, and M. Franceschetti, "Stochastic geometry and random graphs for the analysis and design of wireless networks," *IEEE journal on selected areas in communications*, vol. 27, no. 7, pp. 1029–1046, 2009.

[88] V. H. Mac Donald, "Advanced mobile phone service: The cellular concept," *The bell system technical Journal*, vol. 58, no. 1, pp. 15–41, 1979.

[89] M. Di Renzo, A. Guidotti, and G. E. Corazza, "Average rate of downlink heterogeneous cellular networks over generalized fading channels: A stochastic geometry approach," *IEEE Transactions on Communications*, vol. 61, no. 7, pp. 3050–3071, 2013.

[90] X. Lu, M. Salehi, M. Haenggi, E. Hossain, and H. Jiang, "Stochastic geometry analysis of spatial-temporal performance in wireless networks: A tutorial," *IEEE Communications Surveys & Tutorials*, vol. 23, no. 4, pp. 2753–2801, 2021.

[91] C.-H. Lee, C.-Y. Shih, and Y.-S. Chen, "Stochastic geometry based models for modeling cellular networks in urban areas," *Wireless networks*, vol. 19, pp. 1063–1072, 2013.

[92] W. Lu and M. Di Renzo, "Stochastic geometry modeling of cellular networks: Analysis, simulation and experimental validation," in *Proceedings of the 18th ACM International Conference on Modeling, Analysis and Simulation of Wireless and Mobile Systems*, pp. 179–188, 2015.

[93] A. Guo and M. Haenggi, "Spatial stochastic models and metrics for the structure of base stations in cellular networks," *IEEE Transactions on Wireless Communications*, vol. 12, no. 11, pp. 5800–5812, 2013.

[94] F. Baccelli, M. Klein, M. Lebourges, and S. Zuyev, "Stochastic geometry and architecture of communication networks," *Telecommunication Systems*, vol. 7, pp. 209–227, 1997.

[95] M. Matracia, M. A. Kishk, and M.-S. Alouini, "Coverage analysis for UAV-assisted cellular networks in rural areas," *IEEE Open Journal of Vehicular Technology*, vol. 2, pp. 194–206, 2021.

[96] M. A. Ouamri, D. Singh, M. A. Muthanna, A. Bounceur, and X. Li, "Performance analysis of UAV multiple antenna-assisted small cell network with clustered users ," *Wireless Networks*, pp. 1–14, 2023.

[97] N. Deng, L. Chen, and H. Wei, "A 3D UAV-assisted cellular network model with inter-tier dependence," in *2021 IEEE Wireless Communications and Networking Conference (WCNC)*, pp. 1–6, IEEE, 2021.

[98] C. Saha, H. S. Dhillon, N. Miyoshi, and J. G. Andrews, "Unified analysis of HetNets using Poisson cluster processes under max-power association," *IEEE Transactions on Wireless Communications*, vol. 18, no. 8, pp. 3797–3812, 2019.

[99] Y. Yao, Y. Wu, Z. Zhu, X. Qin, and X. Yue, "Modeling and performance analysis in UAV-assisted cellular networks with clustered edge users," *Electronics*, vol. 11, no. 5, p. 828, 2022.

[100] M. Afshang, C. Saha, and H. S. Dhillon, "Nearest-neighbor and contact distance distributions for Thomas cluster process," *IEEE Wireless Communications Letters*, vol. 6, no. 1, pp. 130–133, 2016.

[101] M. Afshang, C. Saha, and H. S. Dhillon, "Nearest-neighbor and contact distance distributions for Matérn cluster process," *IEEE Communications Letters*, vol. 21, no. 12, pp. 2686–2689, 2017.

[102] R. K. Ganti and M. Haenggi, "Interference and outage in clustered wireless ad hoc networks," *IEEE transactions on information theory*, vol. 55, no. 9, pp. 4067–4086, 2009.

[103] W. Yi, Y. Liu, and A. Nallanathan, "Modeling and analysis of D2D millimeter-wave networks with poisson cluster processes," *IEEE Transactions on Communications*, vol. 65, no. 12, pp. 5574–5588, 2017.

[104] Y. J. Chun, M. O. Hasna, and A. Ghrayeb, "Modeling heterogeneous cellular networks interference using Poisson cluster processes," *IEEE Journal on Selected Areas in Communications*, vol. 33, no. 10, pp. 2182–2195, 2015.

[105] L. Yang, T. J. Lim, J. Zhao, and M. Motani, "Modeling and analysis of HetNets with interference management using Poisson cluster process," *IEEE Transactions on Vehicular Technology*, vol. 70, no. 11, pp. 12039–12054, 2021.

[106] C.-h. Lee and M. Haenggi, "Interference and outage in Poisson cognitive networks," *IEEE Transactions on Wireless Communications*, vol. 11, no. 4, pp. 1392–1401, 2012.

[107] W. Yi, Y. Liu, E. Bodanese, A. Nallanathan, and G. K. Karagiannidis, "A unified spatial framework for UAV-aided mmWave networks," *IEEE Transactions on Communications*, vol. 67, no. 12, pp. 8801–8817, 2019.

[108] P. D. Mankar, G. Das, and S. S. Pathak, "Modeling and coverage analysis of BS-centric clustered users in a random wireless network," *IEEE Wireless Communications Letters*, vol. 5, no. 2, pp. 208–211, 2016.

[109] V. V. Chetlur and H. S. Dhillon, "Downlink coverage analysis for a finite 3-D wireless network of unmanned aerial vehicles," *IEEE Transactions on Communications*, vol. 65, no. 10, pp. 4543–4558, 2017.

[110] X. Shi and N. Deng, "Coverage probability of UAV-enabled millimeter wave communications in finite areas," in *2021 IEEE Wireless Communications and Networking Conference (WCNC)*, pp. 1–6, IEEE, 2021.

[111] C. K. Armeniakos, P. S. Bithas, and A. G. Kanatas, "Finite point processes in a truncated octahedron-based 3D UAV network," *IEEE Transactions on Vehicular Technology*, vol. 71, no. 7, pp. 7230–7243, 2022.

[112] R. Cowan, "Objects arranged randomly in space: an accessible theory," *Advances in Applied Probability*, vol. 21, no. 3, pp. 543–569, 1989.

[113] T. Bai, R. Vaze, and R. W. Heath, "Analysis of blockage effects on urban cellular networks," *IEEE Transactions on Wireless Communications*, vol. 13, no. 9, pp. 5070–5083, 2014.

[114] Y. Xiao, "A tutorial on analysis and simulation of boolean gene regulatory network models," *Current genomics*, vol. 10, no. 7, pp. 511–525, 2009.

[115] J.-H. Lee, J.-S. Choi, and S.-C. Kim, "Cell coverage analysis of 28 GHz millimeter wave in urban microcell environment using 3-D ray tracing," *IEEE Transactions on Antennas and Propagation*, vol. 66, no. 3, pp. 1479–1487, 2018.

[116] W. Khawaja, I. Guvenc, D. W. Matolak, U.-C. Fiebig, and N. Schneckenburger, "A survey of air-to-ground propagation channel modeling for unmanned aerial vehicles," *IEEE Communications Surveys & Tutorials*, vol. 21, no. 3, pp. 2361–2391, 2019.

[117] M. Simunek, P. Pechac, and F. P. Fontán, "Excess loss model for low elevation links in urban areas for UAVs," *Radioengineering*, vol. 20, no. 3, pp. 561–568, 2011.

[118] H. Zhang, L. Song, and Z. Han, *Unmanned aerial vehicle applications over cellular networks for 5G and beyond*. Springer, 2020.

[119] C. Yan, L. Fu, J. Zhang, and J. Wang, "A comprehensive survey on UAV communication channel modeling," *IEEE Access*, vol. 7, pp. 107769–107792, 2019.

[120] N. Goddemeier and C. Wietfeld, "Investigation of air-to-air channel characteristics and a UAV specific extension to the rice model," in *2015 IEEE Globecom Workshops (GC Wkshps)*, pp. 1–5, IEEE, 2015.

[121] L. Yang and M.-S. Alouini, "On the average outage rate and average outage duration of wireless communication systems with multiple cochannel interferers," *IEEE transactions on wireless communications*, vol. 3, no. 4, pp. 1142–1153, 2004.

[122] P. Liu, M. Di Renzo, and A. Springer, "Line-of-sight spatial modulation for indoor mmWave communication at 60 GHz," *IEEE Transactions on Wireless Communications*, vol. 15, no. 11, pp. 7373–7389, 2016.

[123] D. Maamari, N. Devroye, and D. Tuninetti, "Coverage in mmWave cellular networks with base station co-operation," *IEEE transactions on Wireless Communications*, vol. 15, no. 4, pp. 2981–2994, 2016.

[124] D. Wang, R. R. Sattiraju, and H. D. Schotten, "Performances of C-V2X communication on highway under varying channel propagation models," in *2018 10th International Conference on Communications, Circuits and Systems (ICCCAS)*, pp. 305–309, IEEE, 2018.

[125] R. Amer, W. Saad, and N. Marchetti, "Mobility in the sky: Performance and mobility analysis for cellular-connected UAVs," *IEEE Transactions on Communications*, vol. 68, no. 5, pp. 3229–3246, 2020.

[126] X. Shi and N. Deng, "Modeling and Analysis of mmWave UAV Swarm Networks: A Stochastic Geometry Approach," *IEEE Transactions on Wireless Communications*, vol. 21, no. 11, pp. 9447–9459, 2022.

[127] N. Kouzayha, H. ElSawy, H. Dahrouj, K. Alshaikh, T. Y. Al-Naffouri, and M.-S. Alouini, "Stochastic geometry analysis of hybrid aerial terrestrial networks with mmWave backhauling," in *ICC 2020-2020 IEEE International Conference on Communications (ICC)*, pp. 1–7, IEEE, 2020.

[128] M.-S. Alouini and A. J. Goldsmith, "Area spectral efficiency of cellular mobile radio systems," *IEEE Transactions on vehicular technology*, vol. 48, no. 4, pp. 1047–1066, 1999.

[129] A. AlAmmouri, J. G. Andrews, and F. Baccelli, "A unified asymptotic analysis of area spectral efficiency in ultradense cellular networks," *IEEE Transactions on Information Theory*, vol. 65, no. 2, pp. 1236–1248, 2018.

[130] N. Al-Falahy and O. Y. Alani, "Technologies for 5G networks: Challenges and opportunities," *It Professional*, vol. 19, no. 1, pp. 12–20, 2017.

[131] S. K. Khan, U. Naseem, H. Siraj, I. Razzak, and M. Imran, "The role of unmanned aerial vehicles and mmWave in 5G: Recent advances and challenges," *Transactions on Emerging Telecommunications Technologies*, vol. 32, no. 7, p. e4241, 2021.

[132] X. Wang, H. Zhang, and V. C. Leung, "Modeling and performance analysis of UAV-assisted cellular networks in isolated regions," in *2018 IEEE International Conference on Communications Workshops (ICC Workshops)*, pp. 1–6, IEEE, 2018.

[133] P. Ji, X. Jia, Y. Lu, H. Hu, and Y. Ouyang, "Multi-UAV assisted multi-tier millimeter-wave cellular networks for hotspots with 2-tier and 4-tier network association," *IEEE Access*, vol. 8, pp. 158972–158995, 2020.

[134] M. Baianifar, S. M. Razavizadeh, S. Khavari-Moghaddam, and T. Svensson, "Effect of users height distribution on the coverage of mmWave cellular networks with 3D beamforming," *IEEE Access*, vol. 7, pp. 68091–68105, 2019.

[135] L. Zhu, J. Zhang, Z. Xiao, X. Cao, D. O. Wu, and X.-G. Xia, "3-D beamforming for flexible coverage in millimeter-wave UAV communications," *IEEE Wireless Communications Letters*, vol. 8, no. 3, pp. 837–840, 2019.

[136] D. Alkama, M. A. Ouamri, M. Azni, and X. Li, "Coverage and network spectral efficiency analysis for UAV swarm under 3D beamforming in isolated regions," *Telecommunication Systems*, pp. 1–13, 2024.

[137] A. Valcarce, T. Rasheed, K. Gomez, S. Kandeepan, L. Reynaud, R. Hermenier, A. Munari, M. Mohorcic, M. Smolnikar, and I. Bucaille, "Airborne base stations for emergency and temporary events," pp. 13–25, 2013.

[138] B. Galkin, J. Kibiłda, and L. A. DaSilva, "A stochastic model for UAV networks positioned above demand hotspots in urban environments," *IEEE Transactions on Vehicular Technology*, vol. 68, no. 7, pp. 6985–6996, 2019.

[139] S. Srinivasa and M. Haenggi, "Distance distributions in finite uniformly random networks: Theory and applications," *IEEE Transactions on Vehicular Technology*, vol. 59, no. 2, pp. 940–949, 2009.

[140] N. Zhao, W. Lu, M. Sheng, Y. Chen, J. Tang, F. R. Yu, and K.-K. Wong, "UAV-assisted emergency networks in disasters," *IEEE Wireless Communications*, vol. 26, no. 1, pp. 45–51, 2019.

[141] A. M. Hayajneh, S. A. R. Zaidi, D. C. McLernon, M. Di Renzo, and M. Ghogho, "Performance analysis of UAV enabled disaster recovery networks: A stochastic geometric framework based on cluster processes," *IEEE Access*, vol. 6, pp. 26215–26230, 2018.

[142] O. S. Oubbati, H. Badis, A. Rachedi, A. Lakas, and P. Lorenz, "Multi-UAV Assisted Network Coverage Optimization for Rescue Operations using Reinforcement Learning," in *2023 IEEE 20th Consumer Communications & Networking Conference (CCNC)*, pp. 1003–1008, IEEE, 2023.

[143] M. A. Ouamri, R. Alkanhel, C. Gueguen, M. A. Alohali, and S. S. Ghoneim, "Modeling and analysis of uav-assisted mobile network with imperfect beam alignment," *CMC-Computers, Materials & Continua*, vol. 74, no. 1, pp. 453–467, 2023.

[144] M. Gapeyenko, V. Petrov, D. Moltchanov, S. Andreev, N. Himayat, and Y. Koucheryavy, "Flexible and reliable UAV-assisted backhaul operation in 5G mmWave cellular networks," *IEEE Journal on Selected Areas in Communications*, vol. 36, no. 11, pp. 2486–2496, 2018.

[145] A. Okaf, A. Saied, and D. Qiu, "Analysis of Self-Blockage Impact on Handover Probability for User with Mobility in 5G Mm-Wave Cellular Network," in *2021 International Symposium on Networks, Computers and Communications (ISNCC)*, pp. 1–5, IEEE, 2021.

[146] S. Geng, J. Kivinen, X. Zhao, and P. Vainikainen, "Millimeter-wave propagation channel characterization for short-range wireless communications," *IEEE transactions on vehicular technology*, vol. 58, no. 1, pp. 3–13, 2008.

[147] L. Qualcomm, "Unmanned aircraft systems—Trial report," 2017.

[148] X. Jia, P. Ji, and Y. Chen, "Modeling and analysis of multi-tier clustered millimeter-wave cellular networks with user classification for large-scale hotspot area," *IEEE Access*, vol. 7, pp. 140278–140299, 2019.

[149] M. Shi, K. Yang, Z. Han, and D. Niyato, "Coverage analysis of integrated sub-6GHz-mmWave cellular networks with hotspots," *IEEE Transactions on Communications*, vol. 67, no. 11, pp. 8151–8164, 2019.

[150] S. Elhoushy, M. Ibrahim, and W. Hamouda, "Cell-free massive MIMO: A survey," *IEEE Communications Surveys & Tutorials*, vol. 24, no. 1, pp. 492–523, 2021.

[151] H. Fu, S. Roy, and L. Peng, "Asymptotic performance analysis of MMSE receivers in multicell MU-MIMO systems," *IEEE Transactions on Vehicular Technology*, vol. 70, no. 9, pp. 9174–9189, 2021.

[152] N. Baskar and P. Selvaprabhu, "Selective interference alignment and neutralization in coordinated multipoint using multiuser MIMO," *International Journal of Communication Systems*, vol. 36, no. 13, p. e5547, 2023.

[153] X. Cheng and Y. Li, "A 3-D geometry-based stochastic model for UAV-MIMO wideband nonstationary channels," *IEEE Internet of Things Journal*, vol. 6, no. 2, pp. 1654–1662, 2018.

[154] T. Hou, Y. Liu, Z. Song, X. Sun, and Y. Chen, "Multiple antenna aided NOMA in UAV networks: A stochastic geometry approach," *IEEE Transactions on Communications*, vol. 67, no. 2, pp. 1031–1044, 2018.

[155] D. Alkama, M. Azni, M. A. Ouamri, and X. Li, "Modeling and Performance Analysis of Vertical Heterogeneous Networks under 3D Blockage Effects and Multiuser MIMO Systems," *IEEE Transactions on Vehicular Technology*, 2024.

[156] D. Alkama, M. A. Ouamri, M. S. Alzaidi, R. N. Shaw, M. Azni, and S. S. Ghoneim, "Downlink performance analysis in MIMO UAV-cellular communication with LOS/NLOS propagation under 3D beamforming," *IEEE Access*, vol. 10, pp. 6650–6659, 2022.

[157] H. Alzer, "On some inequalities for the incomplete gamma function," *Mathematics of Computation*, vol. 66, no. 218, pp. 771–778, 1997.

Résumé

Le principal défi auquel sont actuellement confrontés les opérateurs de réseaux 5G est de fournir une couverture transparente et omniprésente dans les villes denses remplies de bâtiments de grande hauteur, et de combler les vides de couverture dans les zones éloignées tout en veillant à ce que tous les utilisateurs aient accès à des services fiables et de haute qualité. L'utilisation de stations de base montées sur drones (UBSs) est considérée comme une avancée significative dans les réseaux 5G et au-delà. Cette technologie permet une couverture globale des réseaux de communication 3D surmontant ainsi les limites de couverture des réseaux terrestres traditionnels. L'objectif de cette thèse est de mener une étude complète en utilisant la géométrie stochastique pour modéliser avec précision les systèmes, développer de nouvelles technologies, analyser et évaluer la performance des réseaux 3D à ondes millimétriques dans divers scénarios de déploiement. Dans ce contexte, deux modèles ont été proposés : le premier consiste à un essaim d'UBSs à un seul niveau dans des régions isolées où les UBSs utilisent le 3D beamforming et le deuxième consiste à un réseau hétérogène vertical (VHetNet) dans des zones de points chauds avec des blocages 3D de bâtiments et des systèmes de beamforming MIMO multi-utilisateurs (MU-MIMO). Les résultats ont indiqué que l'assistance des UBSs dans les régions isolées avec un angle de tilt optimal permet de fournir une couverture maximale. En outre, les VHetNets avec le beamforming MU-MIMO peuvent faciliter l'établissement d'un réseau cellulaire volant dynamique, permettant la fourniture de services sans fil à couverture élevée, même en présence de blocages 3D.

Mots clés : Analyse des performances, Géométrie stochastique, Onde millimétrique, Réseaux hétérogènes verticaux, Véhicules Aériens sans Pilote.

Abstract

The main challenge currently facing 5G network operators is to provide seamless, ubiquitous coverage in dense cities filled with high-rise buildings, and to fill coverage gaps in remote areas while ensuring that all users have access to reliable, high-quality services. The use of UAV-mounted base stations (UBSs) is considered a significant advancement in the 5G and beyond networks. This technology enables global 3D communication network coverage overcoming the coverage limitations of traditional terrestrial networks. This thesis aims to conduct a comprehensive study using stochastic geometry to accurately model systems, develop new technologies, analyze and evaluate the performance of 3D millimeter-wave (mmWave) networks in various deployment scenarios. In this context, two models have been proposed: the first consists of a swarm of single-tier UBSs in isolated regions where the UBSs use 3D beamforming, and the second consists of a vertical heterogeneous network (VHetNet) in hotspot areas with 3D blockages of buildings and multiuser multiple-input-multiple-output (MU-MIMO) beamforming systems. The results indicated that the assistance of UBSs in isolated regions with optimum tilt angle can provide maximum coverage. In addition, VHetNets with MU-MIMO beamforming can facilitate the establishment of a dynamic flying cellular network, enabling the provision of high-coverage wireless services, even in the presence of 3D blockages.

Keywords : Millimeter-wave, Performance analysis, Stochastic geometry, Unmanned aerial vehicles, Vertical heterogeneous networks (VHetNets).

ملخص

يتمثل التحدي الرئيسي الذي يواجه مشغلي شبكات الجيل الخامس حاليًا في توفير تغطية سلسة وشاملة في المدن المزدحمة المليئة بالمباني الشاهقة، وسد فجوات التغطية في المناطق النائية مع ضمان حصول جميع المستخدمين على خدمات موثوقة وعالية الجودة. يعتبر استخدام المحطات الأساسية المثبتة على المركبات الجوية بدون طيار (UBS) بمثابة تقدم كبير في شبكات الجيل الخامس وما وراءها .تتيح هذه التقنية تغطية شبكة اتصالات عالمية ثلاثية الأبعاد للتغلب على قيود التغطية للشبكات الأرضية التقليدية. تهدف هذه الأطروحة إلى إجراء دراسة شاملة باستخدام الهندسة العشوائية لنمذجة الأنظمة بدقة، وتطوير تقنيات جديدة، وتحليل وتقييم أداء شبكات الموجات المليمترية ثلاثية الأبعاد (mmWave) في سيناريوهات النشر المختلفة. في هذا السياق، تم اقتراح نموذجين: الأول يتكون من سرب من UBSs أحادية الطبقة في مناطق معزولة حيث تستخدم UBSs تشكيل الحزم ثلاثي الأبعاد، والثاني يتكون من شبكة رأسية غير متجانسة (VHetNet) في مناطق النقاط الساخنة مع عوائق ثلاثية الأبعاد من المباني و أنظمة تشكيل الشعاع متعددة المدخلات والمخرجات المتعددة (MU-MIMO). أشارت النتائج إلى أن مساعدة UBSs في المناطق المعزولة بزاوية الميل المثلى يمكن أن توفر أقصى قدر من التغطية. بالإضافة إلى ذلك، يمكن لشبكات VHetNets المزودة بتقنية MU-MIMO أن تسهل إنشاء شبكة خلوية طائرة ديناميكية، مما يتيح توفير خدمات لاسلكية عالية التغطية، حتى في ظل وجود عوائق ثلاثية الأبعاد.

الكلمات المفتاحية : تحليل الأداء ,الشبكات العمودية غير المتجانسة ,مركبة جوية بدون طيار ,موجة ملليمتر ,الهندسة العشوائية .